Growth and investigation of AlN/GaN and (Al,In)N/GaN based Bragg reflectors

DISSERTATION

zur Erlangung des akademischen Grades
doctor rerum naturalium
(Dr. rer. nat.)
im Fach Physik

eingereicht an der
Mathematisch-Naturwissenschaftlichen Fakultät I
Humboldt-Universität zu Berlin

von
Herr M.Sc. Tommy Ive
geboren am 11.03.1968 in Växjö, Schweden

Präsident der Humboldt-Universität zu Berlin:
Prof. Dr. Hans Jürgen Prömel (in Vertretung)

Dekan der Mathematisch-Naturwissenschaftlichen Fakultät I:
Prof. Thomas Buckhout, PhD

Gutachter:

1. Prof. Dr. Klaus H. Ploog
2. Prof. Dr. Enrique Calleja
3. Prof. Dr. W. Ted Masselink

eingereicht am:	8. September 2005
Tag der mündlichen Prüfung:	16. Dezember 2005

Abstract

In this work we investigate the synthesis of Bragg reflectors consisting either of AlN/GaN or of (Al,In)N/GaN by plasma-assisted molecular beam epitaxy (MBE). In addition, we study the impact of Si-doping on the surface morphology and the structural and electrical properties of AlN/GaN Bragg reflectors in order investigate the feasibility of obtaining vertically conducting Bragg mirrors. The structures are grown on conducting SiC(0001) substrates.

A brief introduction to the fundamental concepts used for the growth of AlN and GaN is given. Metal-stable growth at high temperature yield excellent results in terms of surface morphology and crystal quality and have therefore been widely adopted.

We investigate the growth of AlN in detail in order to obtain AlN layers with smooth surfaces and with a high crystal quality thus making these layers suitable for AlN/GaN Bragg reflectors. Si-doping of AlN is performed in order to study the impact of Si-doping on the surface morphology, the structural quality and the electrical properties of AlN. The obtained surface morphology and structural quality for both un-doped and Si-doped AlN layers is comparable to those of GaN layers grown in the same system. In addition, semi-conducting AlN layers are demonstrated. A Si concentration of 6×10^{20} cm^{-3} yields an electron concentration of 7.4×10^{17} cm^{-3} with a mobility of 11 cm^2/Vs and a resistivity of 1.5 Ωcm.

InN growth experiments are performed as part of the optimization of the ternary compound (Al,In)N. The concept of metal-stable growth which is used for AlN and GaN, is not directly applicable for InN since InN decomposes at a temperature at which In does not yet desorb.

The ternary (Al,In)N is subject to spinodal decomposition like in the case of (In,Ga)N but to an even higher degree. A growth temperature of 450°C and above gives rise to phase separation. Growth at 300°C induces crack-formation caused by tensile stresses due to crystallite coalescence and grain boundary formation. Homogeneous and crack-free films are obtained at a growth temperature lying around 400°C under N-rich conditions. All films exhibit a low tilt comparable to GaN layers from the same system, but a large twist ($\approx$1–2°).

The Bragg reflectors based on AlN/GaN exhibit smooth surfaces and interfaces of a very high integrity which is evidenced by reflectance measurements that yield reflectances of 99% and more for these structures. Furthermore, the AlN/GaN Bragg reflectors are crack-free as revealed by differential interference contrast optical microscopy. Reciprocal space maps unambiguously show that the AlN/GaN Bragg reflectors are crack-free due to a relaxation process that results in strain-compensated structures. Key to this relaxation process is that the first layer, which always is GaN, is thin enough (45.5 nm) to relax only partially.

We find that Si-doped AlN/GaN Bragg reflectors are vertically conducting. A doping level of 1.4×10^{20} cm^{-3} gives a specific series resistance of 2×10^{-3} Ωcm^2. In contrast, the undoped structures are insulating. The surprisingly high vertical conductance is an effect of auto-ionization of the Si-donors caused by the internal electrostatic fields.

Finally, we investigate the growth of lattice matched (Al,In)N/GaN Bragg reflectors. Under the appropriate growth conditions these structures are found to be homogeneous and crack-free and have abrupt interfaces and smooth surfaces. The reflectance is lower than expected despite the promising morphological properties. This might possibly be attributed to residual absorption or scattering of the incident light in the (Al,In)N layers.

Keywords:
GaN surface emitting structures, (Al,Ga)N heterostructures, distributed Bragg reflectors, (Al,In)N heterostructures

Zusammenfassung

Thema dieser Arbeit ist die Synthese von AlN/GaN- und (Al,In)N/GaN-Braggreflektoren mittels plasmaunterstützter Molekularstrahlepitaxie. Um die Machbarkeit von vertikal leitfähigen Braggspiegeln zu überprüfen, wird ferner der Einfluß einer Si-Dotierung auf die Oberflächenmorphologie und die strukturellen und elektrischen Eigenschaften von AlN/GaN-Braggreflektoren untersucht. Alle Strukturen werden auf leitfähigen SiC(0001)-Substraten hergestellt.

Die Arbeit beginnt mit einer kurzen Einführung in die grundlegenden Konzepte, die für das Wachstum von GaN und AlN ausgearbeitet wurden. Metallstabile Wachstumsbedingungen und hohe Temperaturen resultieren in Schichten mit ausgezeichneter Oberflächenmorphologie und Kristallqualität und werden daher weithin eingesetzt.

Um AlN-Schichten mit einer für Braggreflektoren geeigneten Oberflächenmorphologie und Kristallqualität zu erhalten, wird das Wachstum von AlN im Detail bearbeitet. Ferner werden die Schichten Si-dotiert und der Einfluß der Si-Dotierung auf die Oberflächenmorphologie sowie die strukturellen und elektrischen Eigenschaften der AlN-Schichten untersucht. Die erhaltene Oberflächenmorphologie und strukturelle Qualität sowohl undotierter als auch Si-dotierter AlN-Schichten ist vergleichbar mit der von im gleichen System hergestellten GaN-Schichten. Ferner werden halbleitende AlN-Schichten erhalten. Eine Si-Konzentration von 6×10^{20} cm^{-3} resultiert in einer Elektronenkonzentration von 7.4×10^{17} cm^{-3} mit einer Beweglichkeit von 11 cm^2/Vs und einem spezifischen Widerstand von 1.5 Ωcm.

Als Teil der Wachstumsoptimierung von (Al,In)N werden InN-Wachstumsexperimente durchgeführt. Das für GaN und AlN benutzte Konzept des metallstabilen Wachstums kann nicht direkt auf InN angewandt werden, da sich InN bereits bei Temperaturen zersetzt, die noch nicht zu einer Desorption von In führt.

Der ternäre Mischkristall (Al,In)N neigt wie (In,Ga)N zur spinodalen Entmischung, jedoch in einem noch höheren Grad. Wachstumstemperaturen über 450°C führen zu einer Phasenseparation. Ein Wachstum bei 300°C induziert die Bildung von Rissen, die durch Zugverspannungen verursacht werden, die wiederum durch Kristallitkoaleszenz und Korngrenzenbildung entstehen. Homogene und rißfreie Schichten werden bei einer Wachstumstemperatur um 400°C und N-reichen Bedingungen erhalten. Alle Schichten weisen eine niedrige polare Mosaizität (Verkippung) auf, die vergleichbar mit GaN-Schichten ist, aber eine hohe azimuthale Mosaizität (Verdrehung) von 1-2°.

AlN/GaN-basierende Braggreflektoren besitzen glatte Oberflächen und Grenzflächen hoher Qualität, wie durch eine Reflektanz von 99% und mehr in Reflektivitätsmessungen an diesen Strukturen gezeigt wird. Wie durch Interferenzkontrastmikroskopie bewiesen wird, sind die AlN/GaN-Braggreflektoren rißfrei. Abbildungen des reziproken Raums belegen, daß die AlN/GaN-Braggreflektoren spannungskompensiert sind und daher rißfrei bleiben. Die Erklärung dieses Befunds liegt in der Tatsache, daß die erste GaN-Schicht dünn genug (45.5 nm) ist, um nur partiell zu relaxieren.

Si-dotierte AlN/GaN-Braggreflektoren sind vertikal leitfähig. Eine Si-Konzentration von 1.4×10^{20} cm^{-3} führt zu einem spezifischen Serienwiderstand von 2×10^{-3} Ωcm^2. Im Gegensatz dazu sind undotierte Strukturen isolierend. Die überraschend hohe vertikale Leitfähigkeit ist ein Ergebnis der Autoionisation der Donatoren durch die internen elektrostatische Felder.

Schließlich wird das Wachstum von gitterangepaßten (Al,In)N/GaN-Braggreflektoren untersucht. Unter den geeigneten Bedingungen sind diese Strukturen homogen, frei von Rissen und weisen abrupte Grenzflächen und glatte Oberflächen auf. Trotz dieser vielversprechenden Eigenschaften ist die Reflektanz niedriger als erwartet. Dieses Ergebnis ist möglicherweise einer residuellen Absorption oder Streuung des einfallenden Lichts in den (Al,In)N-Schichten zuzuschreiben.

Schlagwörter:
GaN-Oberflächenemitter, (Al,Ga)N-Heterostrukturen, Braggreflektoren, (Al,In)N-Heterostrukturen

Parts of this work have already been published:

T. Ive, O. Brandt, M. Ramsteiner, M. Giehler, H. Kostial and K. H. Ploog, *Properties of InN layers grown on 6H-SiC(0001) by plasma-assisted molecular beam epitaxy,* Appl. Phys. Lett. **8**4, 1671 (2004)

T. Ive, O. Brandt, H. Kostial, T. Hesjedal, M. Ramsteiner, and K. H. Ploog, *Crack-free and conductive Si-doped AlN/GaN distributed Bragg reflectors grown on 6H-SiC(0001),* Appl. Phys. Lett. **8**5, 1970 (2004)

T. Ive, O. Brandt, H. Kostial, K. J. Friedland, L. Däweritz, and K. H. Ploog, *Controlled n-type doping of AlN:Si films grown on 6H-SiC(0001) by plasma-assisted molecular beam epitaxy,* Appl. Phys. Lett. **8**6, 024106 (2005)

T. Ive, O. Brandt and K. H. Ploog, *Conductive and crack-free AlN/GaN:Si distributed Bragg reflectors grown on 6H-SiC(0001),* J. Cryst. Growth **2**78, 355 (2005)

T. Ive, O. Brandt and K. H. Ploog, *Highly Reflective and Crack-free Si-doped AlN/GaN Distributed Bragg Reflectors Grown on 6H-SiC(0001) by Molecular Beam Epitaxy,* Proceedings of 31st International Symposium on Compound Semiconductors, Seoul, Korea, 12-16 September 2004, Institute of Physics Conference Series **1**84, 291 (2005)

Abbreviations

AFM	Atomic Force Microscopy
BEP	Beam Equivalent Pressure
BW	Bandwidth
CW	Continuous Wave
DF	Dielectric Function
DIC	Differential Interference Contrast
EELS	Electron Energy Loss Spectroscopy
EM	Electromagnetic
FWHM	Full Width at Half Maximum
IR	Infrared
KKR	Kramer-Kronig Relations
LCL	Lateral Correlation Length
MBE	Molecular Beam Epitaxy
μPL	micro Photoluminescence
MOCVD	Metal-Organic Chemical Vapor Deposition
MOVPE	Metal-Organic Vapor-Phase Epitaxy
MQW	Multiple Quantum Well
P-V	Peak-to-Valley
PL	Photoluminescence
QW	Quantum Well
RCLED	Resonant Cavity Light Emitting Diode
RF	Radio Frequency
RHEED	Reflection High-Energy Electron Diffraction
RIE	Reactive Ion Etching
RMS	Root Mean Square
RSM	Reciprocal Space Mapping
RT	Room Temperature
RTA	Rapid Thermal Annealing
SE	Spectroscopic Ellipsometry
SEM	Scanning Electron Microscopy
SIMS	Secondary Ion Mass Spectrometry
SQW	Single Quantum Well
TE	Transverse Electric
TEM	Transmission Electron Microscopy
TM	Transverse Magnetic
TR-PL	Time-Resolved Photoluminescence
UHV	Ultra High Vacuum
VASE	Variable Angle Spectroscopic Ellipsometry
VCSEL	Vertical Cavity Surface Emitting Laser

Abbreviations (cont.)

XRD	X-Ray Diffraction
XRC	X-Ray Rocking Curve

Contents

Chapter 1

Introduction

Few solid state devices permeates our daily life as pronounced as light emitting diodes (LEDs) and laser diodes (LDs). In fact, they are overshadowed only by the transistor. The power-efficiency, ruggedness and compactness of these light emitting devices are unbeatable and have greatly contributed to their dissemination.

We see LEDs on electronic billboards at airports and subway and train stations indicating departures, arrivals and additional important information. In large cities LED-based huge electronic billboards displaying commercials, have changed the city picture. They are extensively used as back-lighting and indicators in basically all electronic applications that requires a human interface. Since the 1980's, LDs led to the creation of a whole new branch of consumer electronics in the form of CD and DVD players/burners and laser printers. Without LDs and LEDs we would not have Internet which is based on fiber-optics.

The first infrared semiconductor GaAs laser dawned in September 1962 at General Electric from the work of Hall *et al.* [32]. In October the same year Holonyak and Bevacqua, also at General Electric, demonstrated the first red semiconductor laser and red LED based on $GaAs_{1-x}P_x$ [73]. These visible lasers and LEDs were rushed to market by General Electric and were commercially available already in December 1962 ($2600 for a LD and $260 for a LED). Because of the low electrical-to-optical power efficiency (12 lm/W), these devices were initially used only for indoor indicator applications replacing electromechanical meters and nixie tubes.

However, because of the use of $GaAs_{1-x}P_x$ the emission spectrum was limited to colors from infrared to yellow. Blue, violet and UV were still unreachable. This spurred an intense research effort in order to obtain blue and and violet and possibly also UV emission from semiconductors. For years the research was mainly focused on II-VI semiconductors such as ZnSe but did not lead to any usable devices. The only commercially available blue-emitting LED was based on SiC. This device had a very low efficiency and a very low brightness. It was commercialized despite its severe shortcomings, for the simple reason that no alternatives existed.

Another material considered for blue light emission was GaN. Blue, green, yellow and red electroluminescence from a GaN metal-insulator-semiconductor diode was demonstrated by Pankove *et al.* (RCA Princeton Laboratory) already in 1972 [86]. However, the device efficiency was very low and it was not possible to achieve p-type doping. The layers also exhibited a very large unintentional background doping. For these reasons and because of the very poor quality of the GaN epitaxial layers, GaN received very little attention during the 1970's and 1980's. It was not until the groundbreaking work of the group of Akasaki that propelled GaN to a level where it could be considered as a potential candidate for blue light emission. In 1986 Amano *et al.* showed that high quality GaN epitaxial films could be obtained using buffer layers [5]. During 1988, Akasaki *et al.* achieved p-type doped GaN layers for the first time using Mg [4, 6]. Despite these key discoveries GaN was still not considered as a serious candidate for blue LEDs and LDs. This situation was changed by the hard and persistent work of Shuji Nakamura. Then, as an employee of Nichia Chemicals (Japan) which was a small company specialized in phosphors, he was given the task to investigate GaN. In 1993 Nakamura developed the first efficient blue-emitting high-brightness GaN-based LED and in 1996 the first GaN edge-emitting blue-violet/UV continuous-wave LD [75]. Since these devices were introduced commercially the range of applications for LEDs and LDs have been greatly extended. Most notably is that UV-emitting LEDs can be combined with phosphors to create white-light solid-state emitters with an efficiency that is potentially much higher than that of incandescent lamps. The power saving capabilities of solid-state white-light emitters will become increasingly important since our society is consuming more and more energy. Blue LDs are now entering DVD players and are thus expanding the data storage capacity.

Even though the use of LDs is widespread, the device still has several drawbacks. For instance, it is not possible to integrate LDs with other electronic components on a single wafer. Further, it is extremely difficult to perform tests on conventional LDs on the wafer before dicing and packaging. This drives up the costs. For these and other reasons several suggestions have been put forward for other type of laser structures without these drawbacks. The most prevalent of the suggested laser structures is the vertical cavity surface emitting laser (VCSEL). Here, the laser light is extracted perpendicular to the surface of the structure in contrast to conventional edge-emitting semiconductor lasers which emit light parallel to the surface. Large scale integration and device testing on the wafer level are both allowed by the VCSEL scheme. In addition, VCSELs allow unique applications such as, for instance, single mode lasers desirable for coupling into optical fibers and optical neural networks. The first modern continuous-wave VCSEL operating at room temperature was demonstrated in 1989 by the group of Iga at Tokyo Institute of Technology [54]. This device was based on (Ga,Al)As and was emitting in the infrared range. Today VCSELs are used in short and long range fiber-optical interconnections. A cheaper alternative to the VCSEL is offered in the form of a resonant-cavity light emitting diode (RCLED). The RCLED improves the light extraction, which is a problem with normal LEDs and they function at higher operating temperatures than those of VCSELs. So far electrically driven nitride-based RCLEDs or VCSELs have not been realized.

A very exciting and extraordinary phenomenon in the form of cavity polaritons is offered by high-quality nitride-based microcavities. The notion of cavity polariton refers to the quasi-particle that is created by the strong coupling between an exciton and a photon-mode of the cavity [118]. This strong coupling effect has been observed in GaAs microcavities at cryogenic temperatures. However, the large GaN exciton binding energy of 26 meV opens up the study of cavity polaritons at room temperature [49]. This has the interesting implication that, since polaritons are bosons, a Bose-Einstein condensate (BEC) may be formed at room temperature. According to Ref. [108] "These polaritons will condense to their final state with a gain as a result of certain scattering processes, and then coherent light will be emitted from the polaritons in that state." The strong coupling was recently experimentally observed in a GaN microcavity at room temperature by Tawara *et al.* [108]. This might create a whole new type of devices such as lasers without threshold.

Aim of this work This work is concerned with the growth of nitride-based Bragg reflectors by plasma assisted molecular beam epitaxy. The main objective is to grow Bragg reflectors which exhibit a peak reflectance of >99% at a wavelength of 450 nm (blue color). Such structures would be used in a future nitride-based RCLED or VCSEL that is monolithically grown and that emits at 450 nm. In addition, a second objective is to investigate the feasibility of achieving electricically conducting Bragg reflectors.

The growth of AlN/GaN and (Al,In)N/GaN Bragg reflectors are investigated and represent the two different paths chosen for achieving the main objective. AlN/GaN maximizes the difference in refractive index meaning that less periods are needed to obtain a high reflectance. The drawback with this choice is that due to the large lattice mismatch between GaN and AlN the risk of forming cracks is high. On the other hand (Al,In)N with an In-content of 17–18% is lattice matched to GaN thus preventing crack-formation. However, very little is known about (Al,In)N. This material is very prone to phase separation which makes growth very difficult.

In Ch. 2 a brief introduction is given to the conceptual growth conditions that are commonly used for growth of most nitrides by plasma-assisted molecular beam epitaxy. These growth conditions generally yield good results in terms of surface morphology and crystal-, optical- and electrical quality.

Chapter 3 starts by a brief presentation of the quality of our GaN layers grown under the growth conditions outlined in the previous Chapter. This is followed by describing the optimization of the growth of AlN. The aim is to obtain layers that have a morphological and structural quality comparable to GaN. The AlN layers must at least be of a quality that is suitable for AlN/GaN Bragg reflectors. Further, the impact of Si-doping on the morphological and especially the electrical properties of the AlN layers is studied to see if conducting AlN/GaN Bragg mirrors are possible. Both goals are achieved. We obtain AlN layers both un-doped and Si-doped, that are comparable in quality to GaN layers grown in the same system. Further, semi-conducting AlN:Si layers were produced. The highest carrier concentration is 7.4×10^{17} cm^{-3} for a Si-concentration of 6×10^{20} cm^{-3} with a room temperature mobility of 11 cm^2/Vs and a resistivity of 1.5 Ωcm. The growth of InN is then studied as a step towards (Al,In)N. We will see that the growth of InN does not follow the well-established growth recipe used for AlN and GaN. The most important finding is that InN decomposes at a temperature that is lower than the desorption temperature of In. Comparatively low growth temperatures and N-rich growth conditions must therefore be used. Finally, the Chapter is concluded by presenting the results of the growth optimization of (Al,In)N. This ternary is subject to spinodal decomposition and therefore requires special attention. Homogeneous and crack-free (Al,In)N layers are obtained at a growth temperature of 400°C. Lower growth temperatures give rise to crack formation due to tensile stresses caused by crystallite coalescence and grain boundary formation. Higher growth temperatures induce phase separation.

The theoretical framework behind Bragg reflectors is given in Ch. 4 in general and how this theory is applied to (Al,Ga,In)N based Bragg reflectors in particular. The transfer matrix method is introduced as a tool for simulating the reflectance spectrum of Bragg reflectors. This is followed by a treatment of the complex refractive index since accurate knowledge of the refractive index is required for a good simulation of the reflectance spectra. The Chapter ends with the special considerations for nitride-based Bragg reflectors. The theoretical bandwidth and reflectance will be calculated. A discussion on crack-formation and current aperture follows.

Chapter 5 shows the results from the AlN/GaN Bragg reflector growth experiments. We obtain crack-free Bragg reflectors having a smooth surface morphology and abrupt interfaces. These results are evidenced by the high reflectances of these structures ($\geq$99%). Reciprocal space maps show unequivocally that the Bragg reflectors are crack-free because they relax to a strain-compensated state. The cause for this is that the first layer (always 45.5 nm GaN) is thin enough to only partially relax. In conclusion, vertical conductance measurements show that the structures are conducting. A Si-concentration of 1.4×10^{20} cm^{-3} gives a specific series resistance of 2×10^{-3} Ωcm^2. Undoped structures are, on the other hand, insulating. Auto-ionization due to the large internal electric fields in these structures, is the ultimate mechanism behind the (vertical) conductance properties.

In Ch. 6 the results of (Al,In)N growth runs are presented. Our growth optimization yields (Al,In)N/GaN Bragg reflectors that have smooth surfaces and homogeneous and abrupt interfaces like in the case of AlN/GaN. No phase separation or crack-formation is detected. However, the reflectances are lower than expected in spite of the good morphological results. Possibly, residual absorption or scattering could be the cause of the low reflectances.

The varying characterization techniques that are used will be introduced in the respective chapter in which they are employed for the first time.

Chapter 2

Growth of III-nitrides by plasma assisted molecular beam epitaxy

In this Chapter we describe briefly and on a very general level, the fundamental concepts used for the growth of AlN and GaN by plasma-assisted molecular beam epitaxy (PAMBE). Metal-stable growth at high temperature yield excellent results in terms of surface morphology and crystal-, optical- and electrical quality. Therefore, this growth concept has been commonly adopted by numerous groups for the growth of AlN and GaN by PAMBE.

We start by discussing the choice of substrate and how the substrates are treated prior to growth. This is followed by a short description of the employed PAMBE and the growth itself.

2.1 Choice of substrate and substrate preparation

Following the thorough growth optimization described in Ref. [114] which yielded high quality GaN(0001) epitaxial layers, n-doped ($<0.2\Omega$cm) 6H-SiC(0001) and semi-insulating ($>10^5$ Ωcm) 4H-SiC(0001) were chosen as the preferred substrates for the growth of our Bragg reflectors.

As indicated above both electrically conducting and insulating SiC substrates can be obtained. It is also an excellent thermal conductor (better than Cu) that could act as a heat sink in an electrically driven device. Further, the cleavage planes of SiC coincides with those of c-plane GaN [GaN(0001)]. These properties make SiC very attractive as a substrate for nitride growth. However, the surface morphology being very important for the growth of Bragg reflectors, is poor for as-received SiC substrates. A common procedure to improve the surface morphology of SiC is to use H_2-etching. Here, the substrates are heated to 1600°C while passing through H_2. This results in a very smooth surface exhibiting unit cell high steps separated by ≈ 1 μm. The drawback with the H_2-etching method is that it produces micrometer-sized etch-pits inhomogeneously dispersed on the surface. The cause for these etch-pits is that the etching preferentially attacks the micropipes which are common defects in SiC. Micrometer-sized defects are directly detrimental to the reflectance properties of a Bragg reflector. Recently, a proprietary chemo-mechanical polishing offered by NovaSiC yields very

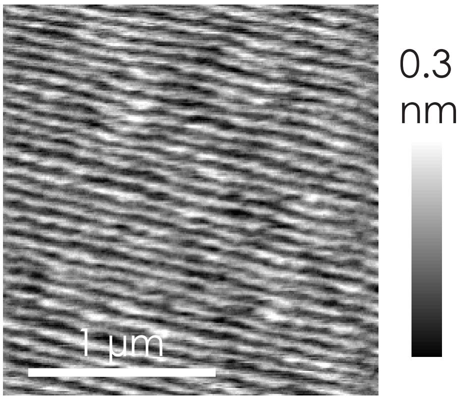

Figure 2.1: AFM scan of a 6H-SiC surface after being polished by NovaSic. Ordered monolayer steps are visible.

smooth SiC surfaces [Fig. 2.1] that are free of etch-pits and which exhibit monolayer steps.

Sapphire or $Al_2O_3(0001)$ is the traditional choice of substrate for nitride growth ever since the synthesis of high quality GaN epitaxial layers by Akasaki [5] and the growth of the first light-emitting pn-junction by Nakamura [75]. Growth on sapphire is initiated by growing an AlN nucleation layer followed by a thick GaN buffer layer in order to reduce the defect density. However, as will be shown in Ch. 5, this buffer layer is unsuitable for the growth of AlN/GaN Bragg reflectors. For the same reason it excludes the use of high quality and low defect density GaN templates.

***Ex-situ* substrate treatment and mounting** All substrates were de-greased for 10 minutes in trichloroethylene and for 5 minutes in acetone and methanol, respectively. After the de-greasing procedure the substrates were rinsed thoroughly in deionized water before they were hydrogen passivated by a 1 minute dip in hydrofluoric (HF) acid. This passivation dip is done to reduce the oxidation of the substrate surface before introducing it into the MBE system. Following the HF dip the substrate is again thoroughly rinsed in de-ionized water before it is put in a water bath and transported to the mounting station. It should be noted though that HF only partially passivates Si-face SiC(0001) surfaces in contrast to Si surfaces [51]. The mounting procedure is not performed in vacuum and therefore the SiC surface is exposed to air and thus suboxides are formed. Additional *in-situ* cleaning steps are therefore desirable in order to rid the substrate surface of oxides. Two techniques are commonly used to achieve this. The first one is thermal cleaning. Here the substrate is heated to a very high temperature (>1000°C) to crack the surface oxides into its constituents which are then pumped away. The second technique used by us, is Ga deposition and flash-off or Ga-polishing for short, and will be discussed in the next paragraph.

At the mounting station, the substrate is blown dry with N_2. A 2 inch Molybdenum substrate/sample holder with a Si template in the center, is put on a heater and heated above the melting point of In (156.6°C). On the Si template, a small piece of In is deposited and melted. The liquid In is used to cover the back side of the substrate with a very thin film of In. Once the SiC substrate is placed on the Si template it almost immediately sticks due to surface adhesion. After cooling down the holder with the newly mounted substrate on it, the holder is loaded into the MBE system. Again, once inside the system, the holder is heated to 900°C for 30 minutes in order to desorb water.

***In-situ* Ga-polishing** The Ga-polishing or Ga flash-off procedure described in the following was always performed before initiating the growth of not only GaN, but of any (Al,Ga,In)N layer which was grown on SiC. This procedure effectively removes residual sub-oxides from the SiC surface [11]. The plasma is off during the procedure and no nitrogen is flowing. The Ga effusion cell temperature is set to the temperature nominally used during growth. At 600°C Ga is deposited for 1 minute onto the substrate and dissolves sub-oxides there. The reaction products and the excess Ga are concurrently desorbed by heating the substrate up to 810°C. The Ga shutter is opened again for 1 minute at 760°C during the warmup to 810°C thereby initiating a second Ga-polishing cycle. After after reaching 810°C the substrate is cooled to the desired growth temperature, which is 760°C in the case of GaN. This marks the end of the Ga desorption procedure.

The bare unpolished SiC surface produces a 1×1 reflection high-energy electron diffraction (RHEED) pattern. An abrupt transition from the 1×1 RHEED pattern to a sharp 3×1 RHEED pattern is observed once the surface is free of sub-oxides. This 3×1 RHEED pattern occurs at 720°C and corresponds to a Si-induced surface reconstruction [50]. The 3×1 RHEED pattern can thus be used as an *in-situ* temperature calibration of the substrate temperature for each individual growth run.

2.2 MBE system

The growth experiments were conducted in a custom built three-chamber (load-lock chamber and middle- and growth chamber) system equipped with solid source effusion cells for Al, Ga, In and Si for n-doping and Mg for p-doping and a water-cooled RF nitrogen plasma source (SVTA) for producing active N. An operating power of nominally 300 W and a N_2-flux of 1 sccm yield a growth rate of 400–450 nm/h. The system has a base pressure of 5×10^{-11} Torr. We use 6N N_2 gas as a precursor which is further purified to 5 ppb by a getter filter.

The load-lock chamber is used to introduce newly mounted substrates into the MBE system and remove grown samples. The chamber is vented to atmospheric pressure before inserting the substrates and is then evacuated again by first a roughing- and a turbo-pump and, once the pressure reaches $1\text{–}3\times10^{-6}$ Torr, by a cryo pump. When the pressure is low enough ($8\times10^{-8}\text{–}1\times10^{-7}$ Torr), the sample is turned towards a heating block and is then heated to 900°C for 30 minutes in order to desorb water. After this water-desorption procedure the sample is transferred into the middle chamber where it is stored until the next growth experiment. The middle chamber is pumped by an ion pump and offers a much lower pressure (10^{-10} Torr range) than the load-lock chamber and is therefore suited for sample storage. It is also equipped with a heating block, which is used for out-gassing brand new sample holders.

A cryo- and an ion pump is continuously pumping the growth chamber, which is fitted with a quadrupole mass spectrometer and a 20 keV RHEED gun. Top and side viewports allow for visual inspection of the sample. A CCD camera can be mounted on the RHEED screen for recording RHEED patterns. The pumping action is improved by a liquid nitrogen cooled cryo-shroud inside the growth chamber. The pneumatically actuated effusion cell shutters, the N-flux and the effusion cell- and sample heater temperatures are all computer controlled.

The temperature was calibrated by visual observation of the melting point of Al (660°C). The metal is deposited using the Al-source at a temperature which is below its melting point. The Al layer grows in a crystalline manner and thus it gives rise to a RHEED pattern. The temperature is increased and once it reaches the melting point of Al the film melts and the RHEED pattern disappears reflecting the amorphous state of the Al melt. The same procedure has been performed with In, which melts at 157°C. In addition, we also used pyrometry as an independent temperature calibration tool, and of course, the previously described Ga-polishing procedure.

2.3 Growth conditions

This Section gives a qualitative introduction to the fundamental concepts used for the growth of AlN and GaN is given. Metal-stable growth at high temperature yield excellent results in terms of surface morphology and crystal quality and have therefore been widely adopted by the PAMBE nitride community [1, 2, 36, 52]. For simplicity, we discuss the growth of GaN only. However, the conclusions of this discussion are also applicable on for instance, the growth of AlN. It should be noted that, on grounds discussed in Ch. 3, this Section does not treat the growth of (Al,In)N.

It is well known that in order to obtain smooth GaN films of high structural, optical and electrical quality, one has to grow in the so called Ga- or metal-stable regime [Fig. 2.2] [11, 36]. In this growth regime, the desorption and the absorption of Ga on the growing surface, balance each other thereby forming a, under steady-state conditions, stable Ga bilayer (1–2 monolayers for AlN growth above 820°C [56]) on the surface. The bilayer promotes the mobility of the Ga adatoms yielding very smooth films.

In the following discussion the Ga-flux (ϕ_{Ga}) is normalized to a constant active N-flux (ϕ_{N}). Figure 2.2 shows the Ga/N-flux ratio ($\frac{\phi_{\mathrm{Ga}}}{\phi_{\mathrm{N}}}$) as a function of the growth temperature. We see that at the nominal growth temperature of 760°C, a wide range of Ga-fluxes (N-flux is constant) may be used to achieve Ga-stable growth conditions. We say that the growth window is wide. If the steady state Ga-stable growth conditions are discontinued by performing a growth interruption through the closing of the Ga shutter, the Ga bilayer will disappear due to incorporation and desorption. Once the surface is completely free of Ga the RHEED intensity increases abruptly. The time between the closing of the Ga shutter until the low-to-high RHEED intensity transition defines the so called recovery time. A recovery time of 10–20 s represents the desired metal-stable growth conditions. If the recovery time is longer than 20 s then the growth is progressing more on the Ga-rich side which could lead to droplet formation. On the other hand, a recovery time below 10 s indicates N-rich growth conditions [53]. RHEED, through the recovery time, thus provides an excellent real-time examination of the growth conditions.

Increasing the flux too high results in a transition into the droplet regime [Fig. 2.2].

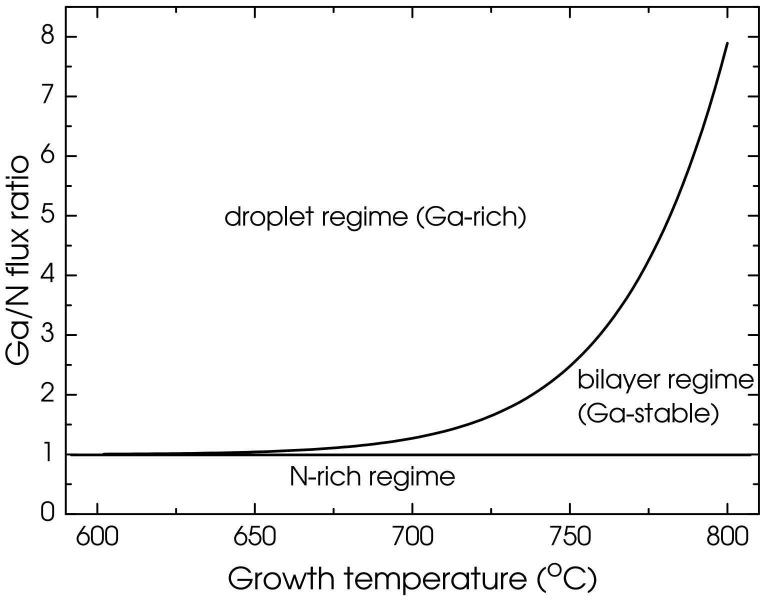

Figure 2.2: Ga-flux (active N-flux is kept constant) vs. GaN growth temperature (rescaled from Ref. [36]).

Here the incoming Ga flux is so high that Ga starts to accumulate which eventually leads to droplet formation [Fig. 2.3 (a)] because the flux of desorbing Ga cannot match the amount of Ga arriving at the surface. The RHEED pattern becomes very diffuse and of a very low intensity and thus RHEED provides a means to detect Ga rich growth conditions. On the other hand, if the Ga-flux is lowered to a level where the desorption rate is larger than the arriving flux of Ga then a continuous Ga bilayer will never form. A transition to the N-rich regime has taken place. These N-rich growth conditions result in samples having the so called plateau-valley morphology which is characterized by extremely smooth plateaus separated by very steep and deep valleys [Fig. 2.3 (b)]. Consequently, the samples grown under these conditions are very rough. The peak-to-valley (P-V) and the root-mean-square (RMS) roughness of the sample shown in Fig. 2.3 are 41 and 6.2 nm, respectively. Since the sidewalls of the valleys are essentially parallel to each other and the plateaus are so smooth, the RHEED pattern remains streaky. However, N-rich growth drastically increases the intensity of the RHEED pattern. Extremely N-rich conditions has nevertheless found to be useful for the growth of GaN nano-columns [89].

If the growth temperature is decreased continuously, Fig. 2.2 shows that the growth window becomes narrower and narrower until it ceases completely. This means that there is no room for adjustments of the Ga flux to reach the desired bilayer growth regime. A minuscule increase of the Ga flux ($1<\phi_{\mathrm{Ga}}$) leads to Ga droplet formation whereas a very small decrease of the Ga-flux ($1>\phi_{\mathrm{Ga}}$) results in N-rich growth with a rough plateau-valley sample surface morphology as an outcome. Each and single Ga atom must be matched by a N atom (stoichiometric growth) in order to avoid droplets and N-rich growth conditions. Stoichiometric growth conditions are impractical and are therefore avoided, because of the extreme control over the growth parameters that is required.

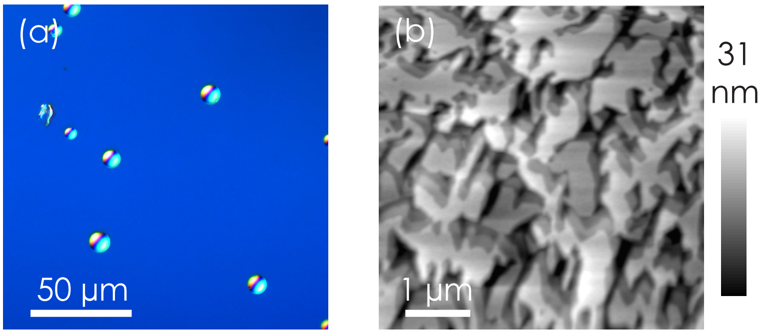

Figure 2.3: DIC optical microscopy image of a GaN sample exhibiting droplets on its surface (a). AFM micrograph of a GaN layer showing plateau-valley surface morphology (P-V and RMS roughness of 41 and 6.2 nm, respectively).

Chapter 3

Optimization of heteroepitaxy of GaN, AlN, InN and (Al,In)N layers on SiC

In this Chapter we investigate the synthesis of the binary compounds GaN, AlN, InN and the ternary compounds (In,Ga)N and (Al,In)N on 6H-SiC along the (0001) direction. The primary objective is to obtain epitaxial layers of high optical quality in order to make these layers suitable for the application in Bragg reflectors. This requires transparent and homogeneous layers with smooth surface morphologies and abrupt interfaces. The secondary objective is to explore the impact of Si-doping on these epitaxial layers in order to investigate the feasibility of achieving vertically conducting Bragg reflectors.

Each section discusses the effect of the growth conditions on the properties of each respective compound.

3.1 Growth of GaN

It should be emphasized that the growth of high quality GaN layers by MBE is well established [114]. We will therefore not dwell on the details of GaN growth. In this Section we will instead immediately present our results which are benchmarked against results available from the literature.

This Section also presents the application of the different characterization techniques, which are used for all the grown materials.

Growth conditions The growth temperature for GaN was set to 760°C. This temperature is at the high end for GaN growth because at 800–810°C GaN starts dissociating resulting in lower growth rates and rough surface morphologies. Later, in Ch. 5 we will see that a higher GaN growth temperature is needed during the growth of AlN/GaN Bragg reflectors in order to counteract Al droplet formation. The plasma power was set to 300 W and the N_2 flux was set to 1 sccm corresponding to metal-stable or bilayer growth conditions with a recovery time of 10–20 s [Ch. 2].

RHEED The nucleation of GaN on SiC occurs through the formation of islands (Volmer-Weber or 3D growth). This give rise to the modulated streaks observed in the RHEED patterns depicted in Figs. 3.1 (a) and (b). Note that the zeroth and first order

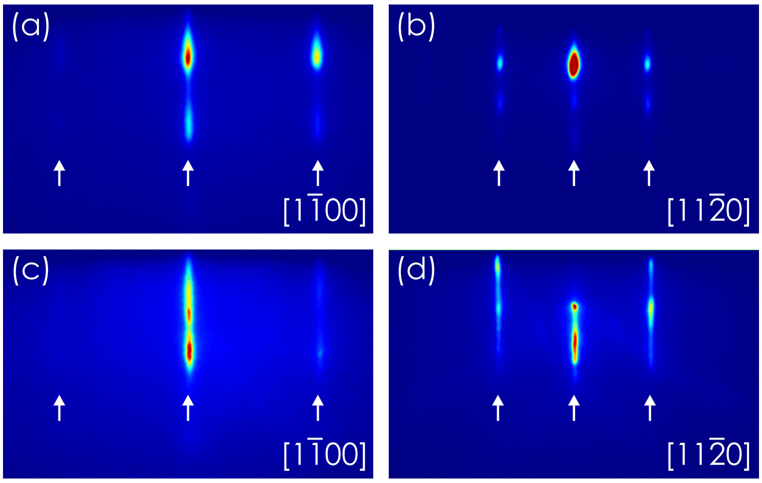

Figure 3.1: RHEED patterns observed during GaN nucleation on SiC (a) and (b). Figures (c) and (d) show the RHEED patterns 2 minutes after the nucleation. The white arrows denote the zeroth and first order bulk streaks. Kikuchi lines and crossings are observed can be observed in (c) and (d).

bulk streaks are indicated by white arrows in Figs. 3.1 (a)–(d). Figures 3.1 (c) and (d) show the RHEED pattern 2 minutes after the nucleation. We observe that the RHEED pattern is streaky and that Kikuchi lines and crossings are visible, which evidences a smooth and connected surface layer. The islands formed during the nucleation have now grown so large that they coalesce and the growth is now proceeding in a layer-by-layer manner (Frank Van der Merwe or 2D growth).

A transition from island to layer-by-layer growth that takes too long (>2 minutes) indicates that the Ga flux is too low resulting in N rich growth conditions. In this case the RHEED pattern exhibits spots and pronounced facets. The surface will become very rough unless the Ga flux is adjusted quickly so that Ga-stable growth conditions are reached.

Thickness determination For the growth of Bragg reflectors it is essential to achieve a good control of the thicknesses of the constituent layers. This will be discussed in more detail in Ch. 4. For thick layers we use spectroscopic ellipsometry (SE) and scanning electron microscopy (SEM) to determine the layer thicknesses (and thus the growth rate).

Spectroscopic ellipsometry is a very quick and non-destructive characterization technique that ultimately gives the complex refractive index $N = n + ik$ for a bulk material. The SE setup consists of a Hg lamp fixed at an incidence angle of 60° with respect to the sample surface normal. All SE measurements were carried out at room temperature (RT). Figure 3.2 shows the real and imaginary parts (n and k) of the complex refractive index for a 1.03 μm thick GaN layer grown on SiC. The GaN layer is transparent for photon energies below the band gap at RT (3.42 eV for GaN grown on SiC). Therefore, the complex refractive is modulated by interference fringes arising from the cavity that is formed by the GaN epitaxial layer being sandwiched between the SiC substrate and the air. Thus, what is observed is a pseudo refractive index N_{pseudo} given by the above mentioned combination of SiC substrate/GaN/air. From comparison to simulations, it was found that each oscillation roughly corresponds to 100 nm yielding a total thickness of 1000 nm which is in good agreement with SEM

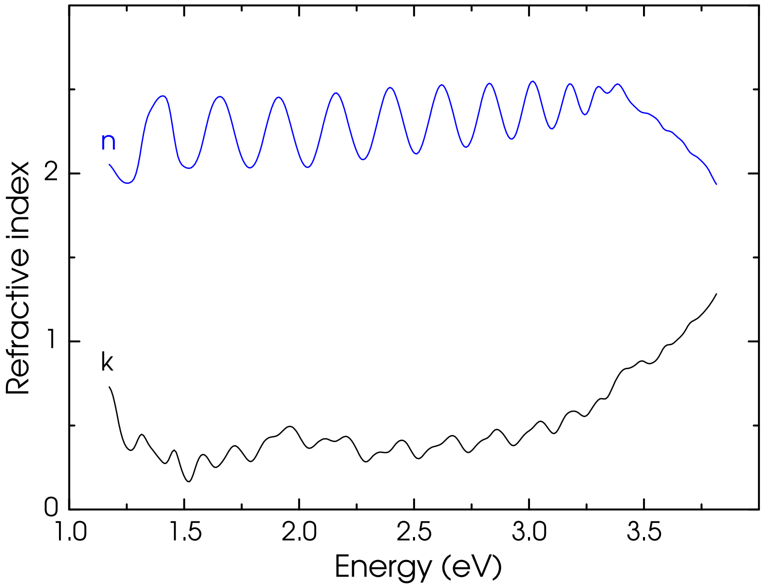

Figure 3.2: Real *n* (top) and imaginary *k* (bottom) parts of the complex pseudo-refractive index N_{pseudo} obtained by SE for a 1.03 μm thick GaN layer grown on SiC. Note the abrupt dampening of the interference fringes at the GaN band gap (3.42 eV) due to absorption.

measurements [Fig. 3.3]. This allowed us to use SE as a routine technique for approximate but quick first estimations of the layer thicknesses. The clearly resolved interference fringes also evidence a smooth surface morphology because the interference fringes tend to be damped or absent altogether in the case of a rough surface.

Cross-sectional scanning electron microscopy was employed when a higher accuracy of the thickness determination was needed. A DSM 982 Gemini (Carl Zeiss Company) SEM with a maximum acceleration voltage of 30 kV and a typical beam current of 0.1–0.5 nA was used to measure the sample layer thicknesses through secondary electron imaging. Figure 3.3 shows a cross-sectional SEM micrograph of the GaN layer in Fig. 3.2. The GaN layer is the bright area with the SiC substrate to the right (dark grey). We see that the layer is 1.03 μm thick. It should be noted that SEM (and SE) was used primarily for thickness measurement for thick layers or, if needed, for an independent evaluation of thickness data coming from x-ray diffraction (XRD) measurements. We will see later that, in the case of multilayer structures or thin layers, XRD is a more accurate and much quicker method to determine the layer thicknesses.

Surface morphology Optical microscopy in combination with atomic force microscope (AFM) was used to characterize sample surface morphologies.

A differential interference-contrast (DIC) optical microscope (Zeiss Axiotech) with a maximum magnification of 1000× and fitted with a CCD camera was used to determine the presence of droplets or remnants of droplets ("footprints"), crystallites and cracks on the sample surface. The AFM scans were performed with a Veeco Dimension 3100 atomic force microscope. The instrument was operated in tapping mode with a Si cantilever. All measurements were done under ambient conditions. Figure 3.4 (a) shows a DIC optical microscopy image from a GaN sample. The surface is free of cracks and other features. An AFM micrograph of a GaN sample over a 2×2 μm^2 area is shown in Fig. 3.4 (b). We observe clearly resolved monolayer steps separated by

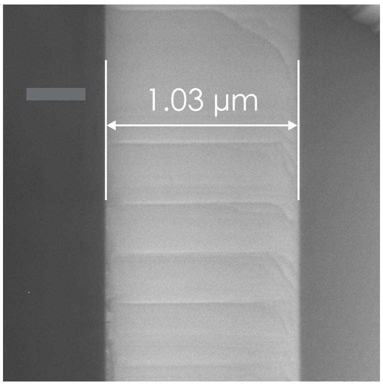

Figure 3.3: Cross-sectional SEM micrograph of a GaN layer grown on SiC. The GaN layer is the bright area with the SiC substrate to the right (dark grey).

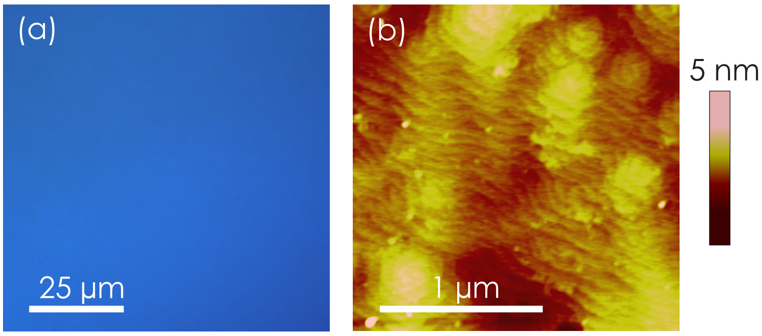

Figure 3.4: DIC optical microscopy image of a GaN sample (a). AFM micrograph from the surface of a GaN sample (b). Monolayer steps with a separation of 50 nm are clearly visible on the scanned 2×2 μm^2 area.

terraces with a width of 50 nm. The peak-to-valley (P-V) roughness is 4.11 nm and the root-mean-square (RMS) roughness is 0.31 nm.

Strain and structural properties We used XRD as the principal method to determine the strain state, the lattice constant, the tilt and the twist, which are induced by dislocations and, in the case of thin layers or structures, the layer thicknesses. This method is non-destructive and much less time-consuming than transmission electron microscopy (TEM) since it does not require any sample preparation prior to measuring. The XRD measurements were performed with a Philips X'Pert PRO four-circle triple-axis diffractometer equipped with a CuKα_1 ($\lambda_{\mathrm{CuK}\alpha_1}$=0.1540562 nm) source in the focus of a multilayer x-ray mirror and a Ge(022) hybrid monochromator. The instrumental broadening amounts to 0.0067° or 24 arcsec. The strain state was probed by performing ω-2θ scans with a three-bounce Ge(022) analyzer for the GaN(0002) reflection, which allows to determine the peak positions with a very high accuracy. X-ray rocking curves (XRC) in asymmetric coplanar geometry for the $(10\bar{1}5)$ and $(10\bar{1}\bar{5})$ reflections were recorded to determine the a and c lattice constants. XRC scans are performed with a wide open detector at fixed position θ_B, leading to an angular acceptance of 1° for our diffractometer. A very quick estimate of the polar orientational spread or tilt t can be obtained by carrying out symmetric ω-scans for the GaN(0002) reflection. The full-width-at-half-maximum (FWHM) or width, for short, of this XRC gives information that is a combination of the tilt and the lateral correlation length. More time-consuming reciprocal space maps (RSM) are needed to completely decouple the tilt and the lateral correlation length. By comparing the results from RSM and XRC we got to know that the lateral correlation length component of the XRC width is minor in our layers and therefore the symmetric XRC scans are a good measure of the tilt.

In Ref. [102] a model is presented, which yields very accurate values of not only the tilt but also the twist α or the azimuthal orientational spread. Here, the width of XRC or ω-scans of asymmetric reflections recorded in quasi-symmetric skew-geometry configuration (quasi-symmetric since ω=θ) are used as input parameters. In principle, only one reflection is necessary, but a better accuracy is achieved with several scans. Reference [102] also gives a good description of the skew-geometry configuration. The values obtained for the tilt and twist give a qualitative assessment of the crystal quality in terms of dislocation density. The expressions from Refs. [69] and [17] are the most commonly used to calculate the edge and screw dislocation density. However, as shown in Ref. [44], the estimate of the dislocation density by XRD is possible only with the knowledge of the type of the dislocation distribution (e.g., random, granular or columnar) as given by TEM. It should be noted that the symmetric and asymmetric XRC of the SiC substrate reflections were found to have a width close to the instrumental resolution, which shows that substrate mosaicity as well as strain-induced bending, which is significant for very thick films, can be neglected in the context of this work. In addition, because of the high intensity and narrow width of the SiC substrate peak essentially all measurements were optimized using the SiC(0006) reflection, which was also used as a reference peak.

Table 3.1 summarizes the morphological and the structural properties for two GaN samples grown under similar conditions. Sample M8363 is 1 μm thick and sample M8376 has a thickness of 0.85 μm. Note that t and α are inversely related to each other. If one optimizes exclusively t then this leads to a large α. One has to optimize both t and α until a minimum is reached [34].

Optical properties Photoluminescence (PL) is a very powerful tool for probing the sample purity and the effects contributing to the inhomogeneous broadening of the emission linewidth. Continuous wave (CW) PL spectra were obtained by exciting the samples with the 325 nm line of a He-Cd laser at a maximum power of 30 mW which gives an excitation power density of 230 W/cm^2. Optical density filters of different magnitudes were used to adjust the excitation power to the desired power level, which was measured by a power meter. A He-cooled cryostat was used to cool the samples down to a minimum temperature of 4 K. The samples were mounted on a heating element, which allowed for controlled temperature dependent measurements up to

Table 3.1: Morphological and structural properties of two GaN samples grown under similar conditions. Listed are the P-V and the RMS roughness as well as the tilt t and twist α.

Sample	P-V (nm)	RMS (nm)	t (°)	α (°)
M8363	4.11	0.31	0.065	0.378
M8376	5.73	0.37	0.082	0.316

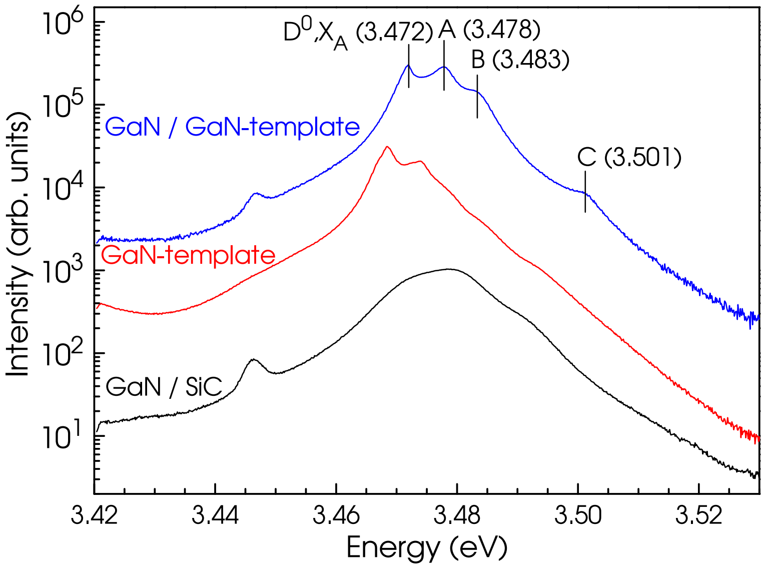

Figure 3.5: PL spectra of a 1 μm thick GaN layer grown on a GaN template (top) and on SiC (bottom). The samples were grown simultaneously. The middle PL spectrum was obtained from the GaN template itself.

400 K. The luminescence was dispersed by a grating with 600 lines/mm before entering a monochromator having a focal length of 1 m. The detection was accomplished by a liquid nitrogen cooled CCD camera. All data were corrected for the PL system response. Micro-photoluminescence (μPL) is a variant of the standard CW PL setup. Here, the setup is essentially the same except that the He-Cd laser beam is focused into a microscope lens before it strikes the surface. This allows mapping of the PL on a micrometer scale and it also allows excitation densities up to 100 kW/cm^2. Figure 3.5 shows μPL spectra from a GaN layer grown on a GaN template (top), from the GaN template itself (middle) and from a GaN layer grown on SiC (bottom). We see that for the epi-layer grown on the GaN template the donor bound exciton D^0,X_A and the A, B and C free excitons are visible at 3.472 eV, 3.478 eV, 3.483 eV and 3.501 eV, respectively. The width of the D^0,X_A exciton emission peak is 2.7 meV. The corresponding width for the GaN template is 5.1 meV. We can also see that the A, B and C excitonic peaks of the GaN template are much less distinct. The GaN layer grown on SiC shows no distinguishable features whatsoever because of its much higher dislocation density. From these results we can draw the conclusion that the chosen growth conditions are most appropriate for GaN growth. Given a low defect density substrate, GaN layers exhibiting excellent optical properties can be grown. However, in Ch. 5 it will be shown that GaN templates are unsuitable for the growth of AlN/GaN Bragg reflectors. Therefore, in this work, all samples were grown on SiC yielding PL spectra that resemble Fig. 3.5 (bottom). The sharp peak at 3.447 eV observed in the top and bottom spectra is due to the outgoing resonance with the free-exciton state for fourth-order Raman scattering.

Electrical properties Knowledge of the carrier concentration is crucial for the implementation of electrically driven semiconductor devices. In this work we determine the carrier concentration with Hall measurements using the van-der-Pauw geometry. Ohmic contacts made of Au-Ge were deposited by a current discharge evaporation technique. Prior to the Hall measurements, all samples were etched in HCl:H_2O (1:3) to remove In from the sample mounting. Hall measurements give the carrier concentration over the whole sample thickness. Therefore, the layers were grown on semi-insulating SiC substrates in order to avoid to measure the conductance through the substrate. The samples were mounted in a cryostat enabling temperature dependent measurements between 4–400 K.

Hall measurements were performed routinely on all samples that were doped with Si. Unintentional doping of GaN is the unavoidable result of having O impurities in the MBE system. This impurity acts as a shallow donor [22]. Hall measurements on unintentionally doped samples reveal the background level of O donors and, thus, give a measure of the purity of the MBE system. For instance, after opening the MBE system for maintenance a few GaN calibration samples were grown for determining the growth rate. Hall measurements were always performed on these unintentionally doped samples to reveal the background level of O. The O concentration in our system yields a background electron concentration in the order of 5×10^{16} cm^{-3} with a mobility of $\sim$11 cm^2/(Vs) due to dislocation scattering.

3.2 Growth of AlN

This Section describes the growth of AlN layers of high quality suitable for AlN/GaN Bragg reflectors. Further, we discuss the impact of Si-doping on the morphological, structural and of course, the electrical properties of these layers. In Ch. 5 we will see that only one type of doping is needed for our purposes. For the reasons outlined in this Section, we therefore concentrate on n-type doping.

Growth conditions The AlN samples were grown at a substrate temperature of 830°C. The plasma power was adjusted to 300 W and the N_2 flux was set to 1 sccm corresponding to Al-stable growth conditions with a recovery time of 10–20 s. These growth conditions yield a growth rate of 435 nm/h. All AlN layers are 0.8 μm thick. The Si doping concentration was adjusted by varying the Si effusion cell temperature between 1120–1205°C.

RHEED AlN nucleates two-dimensionally on SiC evidenced by a RHEED pattern which immediately becomes streaky (1×1) at the start of the growth. This 2D nucleation results from the good wetting of the SiC surface by Al [115]. The RHEED pattern remains streaky throughout the growth. A 4 minute growth interruption at the nominal growth temperature of 830°C produced a (1×3) RHEED pattern as shown in Figs. 3.6 (a) and (b), corresponding to a $(\sqrt{3} \times \sqrt{3})$R30° reconstruction caused by a 1–2 monolayer (ML) thick Al adlayer on the growth front and thus metal-stable growth conditions[56]. Growth interruptions at lower substrate temperatures (<810°C) result in a (2×6) pattern [Figs. 3.6 (c) and (d)], which corresponds to the $(2\sqrt{3} \times 2\sqrt{3})$R30° reconstruction obtained for an Al coverage exceeding 2 ML [56]. We avoid this regime to prevent accumulation of excess Al which in turn could lead to the formation of Al droplets.

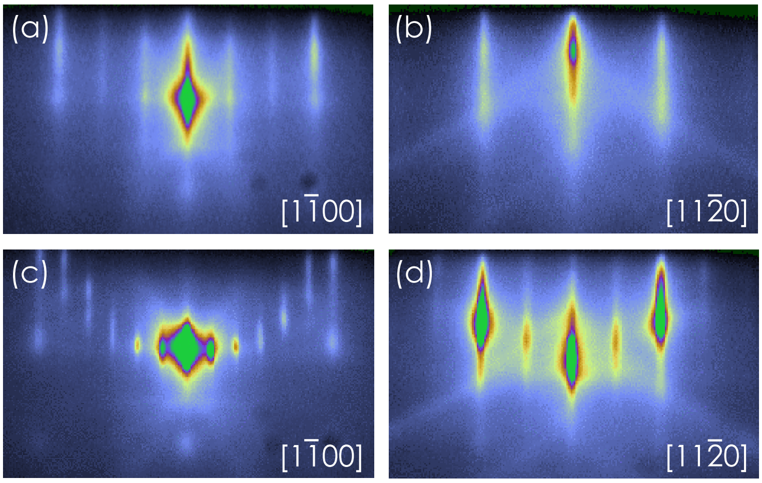

Figure 3.6: RHEED patterns observed during growth interruptions at two different growth temperatures. Figures (a) and (b) show the (1×3) pattern observed at 830°C and higher whereas Figs. (c) and (d) show the (2×6) pattern which is observed at 810°C and lower.

Effects of Si doping on surface morphology and structural properties The surface morphology was examined by DIC optical microscopy and AFM (Park-Scientific) operating in contact mode. Scanning electron microscopy was used to measure the sample thicknesses. All samples are 0.8 μm thick. The crystal quality was investigated by recording ω-scans across the symmetric AlN(0002) and the asymmetric AlN$(10\bar{1}2)$ reflections. The Si concentration was determined by SIMS.

Figure 3.7 shows a DIC optical microscope image from a Si-doped AlN sample (M8362). We observe that the surface is free of cracks and other features.

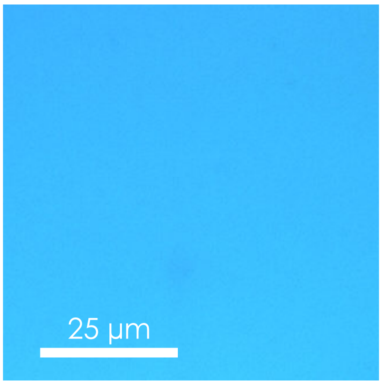

Figure 3.7: DIC optical microscope image of a Si-doped AlN sample (M8362). The surface is free of cracks and featureless.

Figure 3.8 shows AFM micrographs of samples M8332 (a), M8340 (b), M8345 (c) and M8362 (d) [Table 3.2]. Undoped AlN films [Fig. 3.8 (a)] exhibit a very smooth surface with clearly resolved monolayer steps, which is characteristic for step-flow growth. In contrast, the Si-doped films develop a surface morphology indicative of step-bunching caused by pinning of the step motion due to Si adatoms. These Si-induced bunches are between 10–15 ML high regardless of the Si concentration. However, the terrace shape is seen to evolve systematically with increasing Si concentration. Sample M8340, with the lowest Si concentration [Fig. 3.8 (b)], exhibits steps bunched together. These

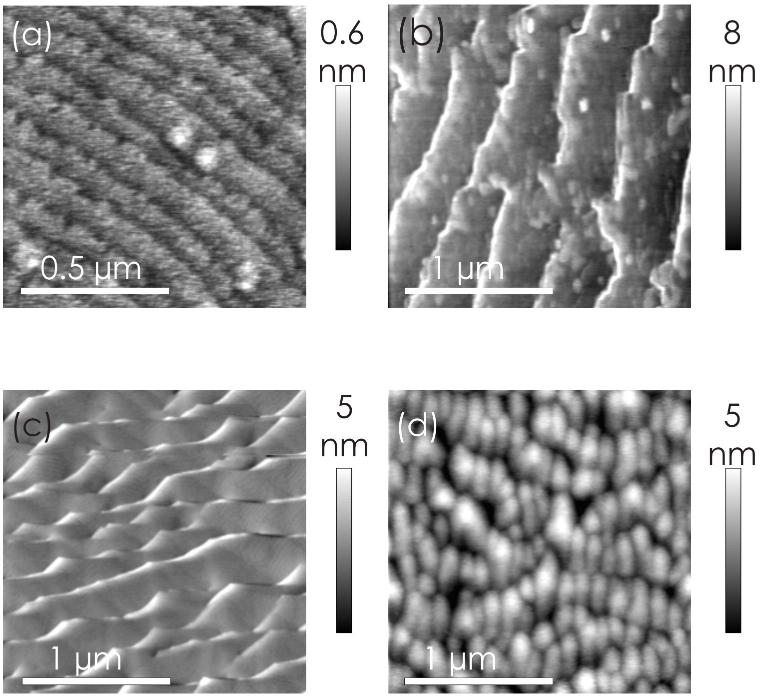

Figure 3.8: AFM micrographs of samples M8332 (a), M8340 (b), M8345 (c) and M8362 (d). In (a), monolayer steps with a separation of 100 nm are clearly visible. In (b), bunched steps building up ridges with a maximum height of 8 nm and a lateral separation of 200 nm are evident. In (c), these ridges start to break up into individual peaks. In (d), this breakup is complete and only individual peaks are observed.

bunched steps form ridges that are running essentially parallel to each other, which resemble the surface morphology of the undoped sample M8332, but on a larger scale. The pinning of step motion becomes evident for sample M8345 [Fig. 3.8 (c)]. Here, triangular peaks along the lateral extension of the ridges have formed. In sample M8362 [Fig. 3.8 (d)], the ridges have broken up entirely into isolated peaks. It should be noted that these isolated peaks have a very low aspect ratio since they are 200 nm wide but only 3 nm high. Similar peak formation, but with a much higher aspect ratio, have been reported for AlN:Si films grown by metal-organic vapor-phase epitaxy (MOVPE) [46].

Table 3.2 summarizes the morphological and the structural properties for five AlN samples grown under similar conditions except for the Si concentration. Listed are the Si concentration ([Si]), the peak-to-valley roughness (P-V), the root-mean-square roughness (RMS), the full width at half maximum (FWHM) of the AlN(0002) and the AlN$(10\bar{1}2)$ reflections and the twist (α). The corresponding values from another research group have been included as a comparison. We see that tilt [FWHM of ω-scans in the (0002) reflection] and twist of all AlN samples, doped as well as undoped, are comparable to the values of tilt and twist measured for GaN epitaxial layers that were grown in the same MBE system [Table 3.1]. For the undoped AlN layers the RMS roughness is 0.07–0.34 nm and it increases to 0.7–1.5 nm for the Si-doped layers. The peak-to-valley value increases from 0.64–1.7 nm for the undoped samples to 6.6–9 nm for the doped samples.

We can conclude that the crystal quality and the surface morphology of both the doped and the undoped AlN epitaxial layers are very well comparable to our best

GaN layers. Furthermore, even heavy Si-doping (6×10^{20} cm^{-3}) does not degrade the structural properties of the AlN films. The morphology of these films is characterized by Si-induced step-bunching, but remains smooth with a root-mean-square roughness of about 1 nm.

Electrical properties Having a band gap of 6.2 eV, undoped AlN is an insulator. It is generally considered to be a ceramic material that is electrically indifferent to doping. A number of theoretical studies predict that it is essentially impossible to overcome the insulating properties of AlN [26, 100, 101, 128]. According to these studies, n-type doping is inhibited by the low formation energy of triply charged Al vacancies V_{Al}^{3-} in n-type AlN. These vacancies act as deep acceptors which compensate the Si donors. This results in a pinning of the Fermi-level close to the midgap. The situation for p-type doping is even worse because of two reasons. Firstly, the acceptor levels are much deeper leading to a much lower charge carrier density at room temperature. Secondly, since the formation energy of the dominating compensating defects V_N^{3+} and Al_i^{3+} is lower than in the case of the corresponding defect for n-type doping [100]. This interpretation is widely accepted since essentially all earlier attempts to produce semiconducting AlN films have failed [48, 57, 78, 127].

Recently, however, several groups using both MOVPE and MBE, have succeeded in obtaining semiconducting AlN [35, 45, 71, 104, 105, 106]. It has been suggested by a number of researchers, that the insulating nature of AlN, in previous reports, is closely related to the presence of O [76]. According to Refs. [22, 67] the formation energy for a defect complex consisting of O on an N-site and an Al vacancy (V_{Al}–O_N) is low and has a high binding energy. The presence of O can therefore increase the density of Al vacancies through the formation of V_{Al}–O_N complexes. Electrically, this complex is acting as a deep acceptor and would therefore compensate the Si donors. It has also been predicted that O undergoes a DX transition in AlN [22, 68]. Oxygen that has undergone a DX transition behaves as a deep acceptor, which could compensate shallow donors. Utmost purity might therefore be crucial for achieving controlled n-type doping of AlN [10].

We determined the mobility, the carrier concentration and the resistivity by temperature dependent (77–400 K) Hall measurements using the van-der-Pauw geometry. The results of these measurements are summarized in Table 3.3. From SIMS measure-

Table 3.2: Structural and morphological properties of doped and undoped AlN samples. Listed are the Si concentration ([Si]), the P-V and the RMS roughnesses, the FWHM of the AlN(0002) and the AlN($10\bar{1}2$) reflections and α. Corresponding values from another group have been included as reference.

Sample	[Si] (cm^{-3})	P-V (nm)	RMS (nm)	FWHM (0002) (°)	FWHM ($10\bar{1}2$) (°)	α (°)
M8332	—	0.64	0.07	0.069	0.204	0.318
M8338	—	1.7	0.34	0.051	0.284	0.417
M8340	4×10^{19}	6.6	1.5	0.071	0.250	0.368
M8345	1.5×10^{20}	7.0	0.65	0.147	0.189	0.235
M8362	6×10^{20}	9.0	1.0	0.150	0.232	0.299
Ref. [35]	1×10^{21}	—	1	0.042	—	—

ments we determined the O background to be 1×10^{18} cm^{-3}. The samples were etched in HCl:H_2O (1:3) to remove In from the sample mounting prior to the Hall measurements. We see that the electron concentration scales with the Si concentration in a consistent way up to a value of 7.4×10^{17} cm^{-3}, which is five times higher than the yet highest reported value of 1.5×10^{17} cm^{-3} in Ref. [76].

Figure 3.9 (a) shows the resistivity of samples M8340, M8345 and M8362 as a function of inverse temperature. As expected intuitively, the resistivity of the samples scales with the Si concentration over the entire temperature range. The difference in resistivity is more pronounced at lower temperatures. We do not observe any Hall effect at temperatures below 200, 150 and 100 K for samples M8340, M8345 and M8362, respectively, as indicated by the arrows in Fig. 3.9 (a). We interpret these findings in the following way: At low temperatures, the resistivity of the layers is governed by impurity-band conduction, and thus no Hall effect occurs. For samples M8345 and M8362, the higher Si concentration results in a larger width of the impurity band as compared to sample M8340. This leads to a significantly lower resistivity at low temperatures. At a certain critical temperature, activation of electrons from the impurity band into the conduction band sets in, which give rise to a Hall effect. In addition, we observe for all samples that the mobility increases with temperature [Fig. 3.9 (b)], which confirms that the fraction of free electrons participating in conduction is indeed increasing with temperature. At room temperature and above, free electrons occupying the conduction band are dominating the electrical transport in our samples.

If we assume an activation energy for a hydrogenic Si-donor level of 60 meV (neglecting central-cell corrections) and use an effective electron mass of $0.32m_0$ [111] we have to assume a concentration of 2.4×10^{19} cm^{-3} for the deep compensating levels in order to match the experimental result of a free carrier concentration of 1.4×10^{17} cm^{-3} for a Si concentration of 4×10^{19} cm^{-3} (M8340). For a Si concentration of 6×10^{20} cm^{-3} we have to assume a density of 1.4×10^{20} cm^{-3} for the deep compensating levels to match the experimental result of 7.4×10^{17} cm^{-3} free carriers (M8362). This increase in the concentration of deep compensating levels might point at silicon self-compensation at higher Si concentrations or an increasing concentration of Al vacancies, as predicted theoretically. On the other hand, if we assume a constant compensating deep-level concentration of 1×10^{18} cm^{-3}, which corresponds to the maximum O background in our samples according to SIMS, we obtain the experimental electron concentrations, but with a Si-donor level located at 165 meV (M8340) and 180 meV (M8362), respectively. These two limiting extremes indicate that Si is in fact a comparatively shallow

Table 3.3: Electrical properties of Si-doped AlN samples. Listed are the Si concentration ([Si]) determined by SIMS, the carrier concentration n, the Hall mobility μ at RT and the resistivity ρ at RT.

Sample	[Si]	n	μ	ρ (RT)
	(cm^{-3})	(cm^{-3})	(cm^2/Vs)	Ωcm
M8340	4×10^{19}	1.4×10^{17}	23	2.5
M8345	1.5×10^{20}	3.6×10^{17}	12	1.7
M8362	6×10^{20}	7.4×10^{17}	11	1.5
Ref. [104]	3×10^{19}	9.5×10^{16}	—	—
Ref. [76]	4×10^{19}	1.5×10^{17}	25	150

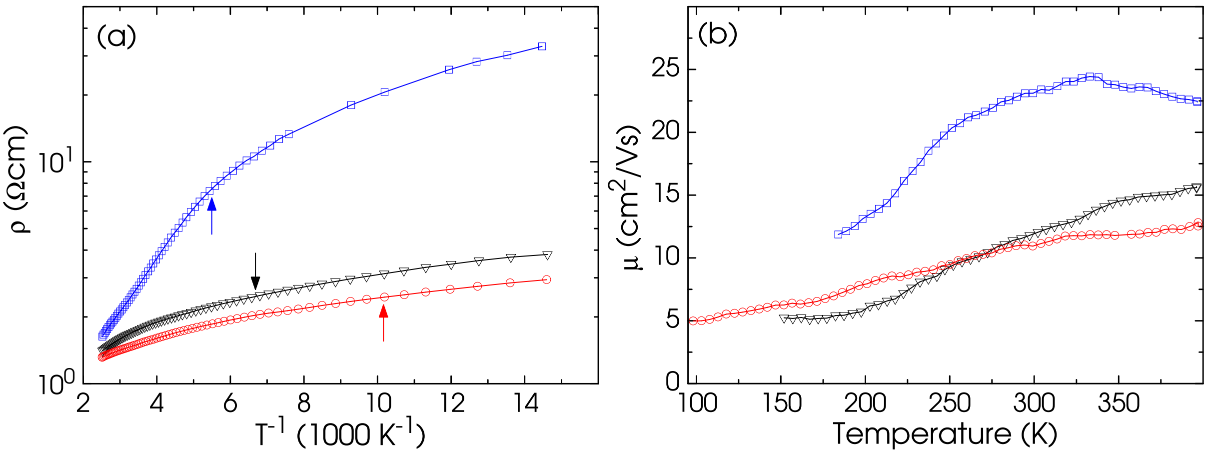

Figure 3.9: Resistivity of samples M8340 (□), M8345 (▽) and M8362 (◯) as a function of the inverse temperature (a). Mobility as a function of temperature for the three samples (b). The lines are a guide to the eye. The arrows indicate the temperature of the onset of the Hall effect.

(60–180 meV) donor in AlN.

The conclusion from our AlN:Si experiments is that it is possible to obtain semiconducting (n-type) AlN. The free electron concentration increases with increasing Si-doping.

3.3 Growth of InN

In this section we discuss the synthesis of InN. We will see that the well established growth conditions outlined in Ch. 2 for AlN and GaN, are not directly applicable for InN. These experiments were performed mainly in order to study the extreme end of the compositional continuum of (Al,In)N as part of the optimization of this ternary compound. However, InN is in itself a very interesting material because, due to the severe growth conditions, its properties are much less known than the properties of GaN and AlN. For instance, the band gap of InN is currently under revision since a large majority of recent publications related to InN report a value of 0.7 eV for the band gap of InN instead of the previous value of 2 eV [107]. It should be noted that growth of InN($000\bar{1}$) as described in Ref. [122] will not be treated here since this is incompatible with the growth of high-quality AlN and GaN which is required for this work.

Growth conditions It is well established that growing GaN and AlN under metal-stable conditions produces epitaxial layers which exhibit both a high crystal quality and a smooth surface. Choosing a sufficiently high growth temperature will yield a high desorbing flux of the group-III element from the growth front. This results in a steady-state metal coverage of the surface while avoiding accumulation of excess metal which eventually leads to droplet formation [Ch. 2]. It is not straightforward to adopt this metal-stable growth method for InN since InN dissociates at a temperature that is lower (500–550°C) than the desorption temperature of In (≈650°C). This has the important consequence that In-rich growth can be induced by merely increasing the temperature above the dissociation point of InN (but below the In desorption point).

When InN starts decomposing, N escapes leaving droplets of In on the surface since the temperature is too low for In desorption. In-rich growth of InN leads to droplet formation and inclusions of crystalline In in the epitaxial layer. Accumulation of In can thus be inhibited only by growing under exactly stoichiometric conditions, which is virtually impossible, or by growing under N-rich conditions.

The InN growth temperature was varied from 420°C to 540°C with the N_2 flux set to 2 sccm. The growth rate of the InN layers was found to depend sensitively on the growth temperature.

RHEED All InN layers exhibited a wurtzite transmission RHEED pattern, reflecting a three-dimensional growth front. This 3D growth is expected because of the large lattice mismatch between for instance InN and GaN (11%) or InN and SiC (15%). A weak superimposed reflection pattern was observed for layers grown under In-rich conditions. In droplets occurred on the surface of these latter layers as well as crystalline In inclusions in the layers.

Strain and structural properties and surface morphology The surface morphology was investigated by DIC optical microscopy and AFM (Park-Scientific) operating in contact mode. Cross-sectional SEM was used to measure the sample thicknesses. We investigated the crystal quality by recording x-ray rocking curves across the symmetric InN(0002) reflection. A 10 mW He-Ne laser emitting at 632.8 nm together with a liquid nitrogen cooled Ge photodetector was used for the Raman measurements.

All samples are black in color and mirror-like to the naked eye. Figure 3.10 shows a DIC optical microscope image from sample M8294. We observe that the surface is fairly smooth and free of cracks.

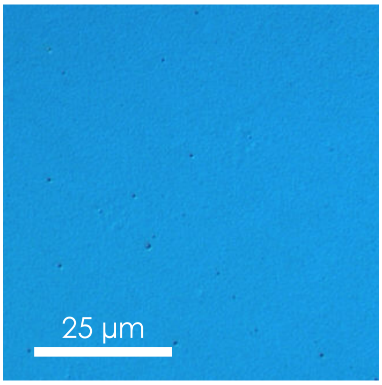

Figure 3.10: DIC optical microscope image of the surface of InN sample M8294. The surface is fairly smooth.

Figures 3.11 (a)–(d) show AFM micrographs of InN layers grown on a GaN buffer layer. The samples were grown at successively lower growth temperatures [Table 3.4]. Sample M8282 (a) was grown at the highest temperature. As mentioned before, this effectively resulted in In-rich growth conditions. Samples M8293 (b), M8294 (c) and M8304 (d) were grown at lower temperatures and thus under N-rich conditions. There is a distinct change in the surface morphology with decreasing substrate temperature. Sample M8282 exhibits a plateau-valley morphology with a very smooth surface on the

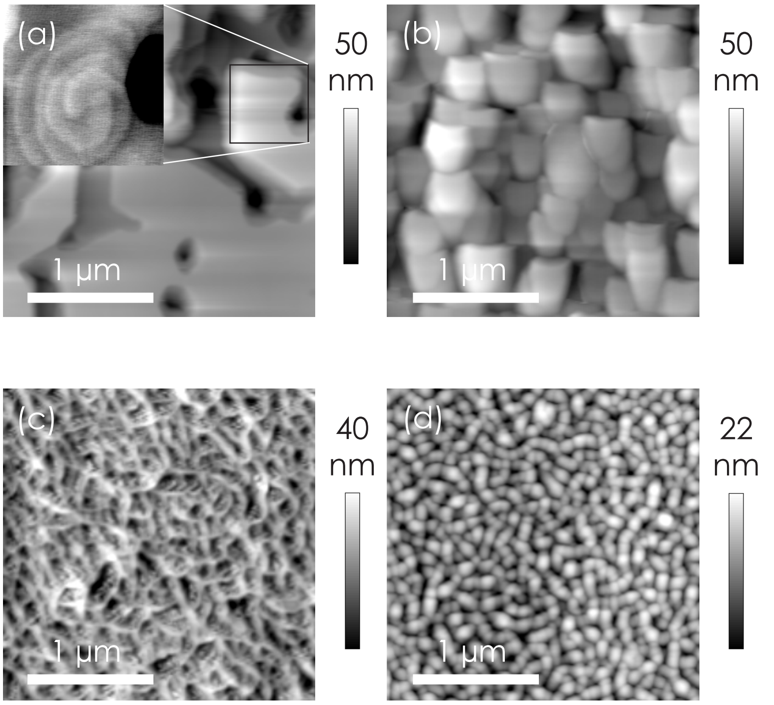

Figure 3.11: AFM micrographs of InN samples M8282 (a), M8293 (b), M8294 (c) and M8304 (d) grown on a GaN buffer layer. The inset in (a) shows a 0.5×0.5 μm^2 close-up of a plateau.

plateaus. The inset in Fig. 3.11 (a) shows a monolayer growth spiral on a plateau. The P-V and RMS values of the inset are 2 nm and 0.16 nm, respectively. In contrast, the samples grown at lower temperatures and under N-rich conditions develop a sponge-like morphology. Deep valleys and atomic steps, as observed on sample M8282, are absent. These morphologies have also been been observed by other groups [27, 37].

Figure 3.12 (a) shows the symmetric x-ray rocking curve for the InN(0002) reflection from sample M8282. We see the SiC(0006), GaN(0002) and InN(0002) reflections, respectively. Crystalline In-inclusions in the layer give rise to the reflection peak between GaN(0002) and InN(0002). Figure 3.12 (b) shows the corresponding results for sample M8301 which was grown under N-rich conditions. No In-inclusion related peak is visible here. All samples grown under In-rich conditions show this In-inclusion related peak.

Figure 3.13 shows the Raman spectrum of sample M8282. The E$_2$(high), A$_1$(LO) and 2A$_1$(LO) phonons can be observed at 489, 594 and 1185.5 cm^{-1}, respectively. A FWHM of the E$_2$(high) phonon mode of 4.7 cm^{-1} attests to the comparatively low disorder (heterogeneous strain) in this InN layer.

Table 3.4 summarizes the morphological and the structural properties of the presented InN layers. We list the growth temperature T$_G$, the layer thickness d (determined by SEM), the P-V and the RMS roughness, the FWHM of XRC of the InN(0002) reflection and the FWHM of the E_2(high) phonon mode ΔE_2. Samples M8282 and M8456 were grown In-rich. All other samples were grown N-rich. For comparison, corresponding values from other research groups have been included. All samples were grown on a buffer layer except sample M8295 which was grown directly on the SiC substrate. This sample has the broadest InN(0002) XRC peak but it remains smooth. Sample M8302 was grown on an AlN buffer layer. The structural and morphological

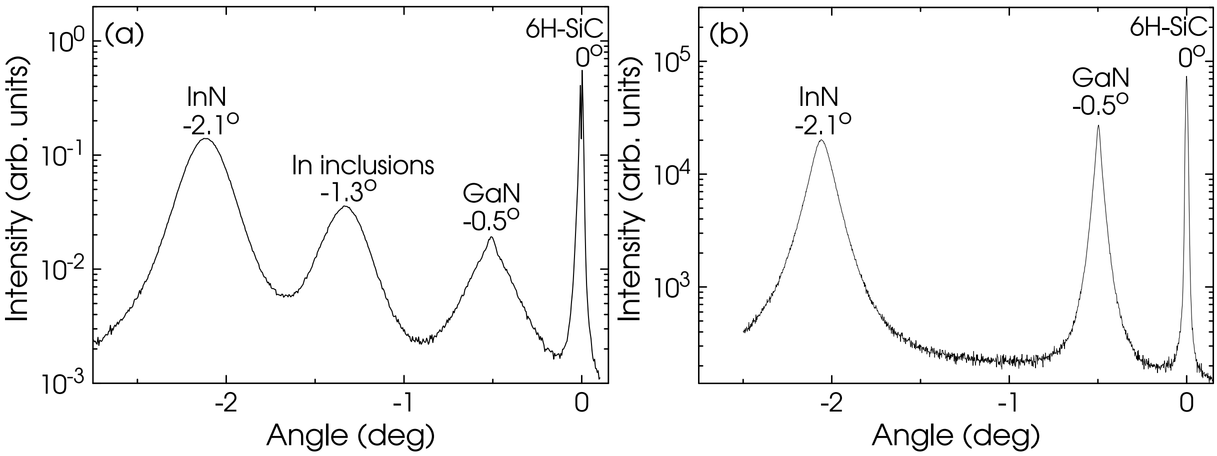

Figure 3.12: Symmetric x-ray rocking curves for the InN(0002) reflection of sample M8282 (a) grown In-rich and sample M8301 (b) grown N-rich. In (a), crystalline In-inclusions give rise to the reflection peak between the GaN(0002) and InN(0002) reflections. In (b), no In-inclusions are observed.

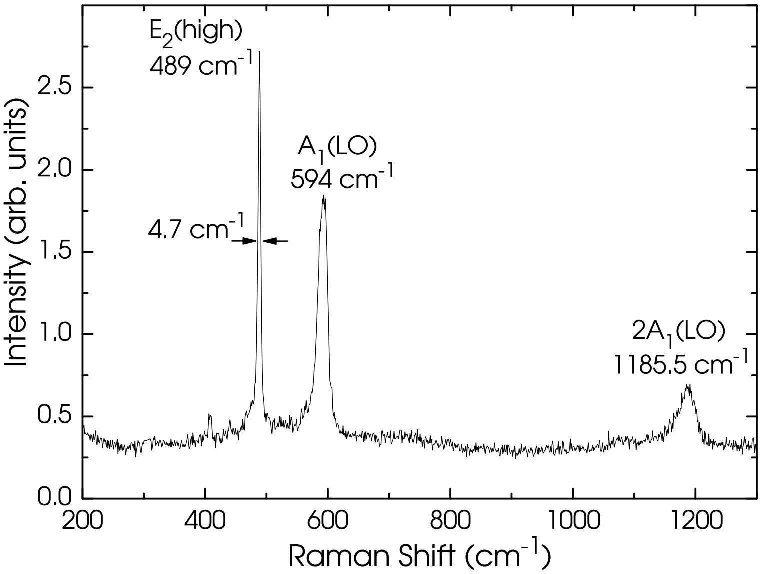

Figure 3.13: Raman spectrum of sample M8282 obtained at room temperature.

properties of this sample are similar to the other samples which were grown on a GaN buffer layer. The samples become progressively smoother with decreasing growth temperature. Our RMS values (4.4–15.9 nm) compare well with reported values of other groups [37, 60]. The crystal quality on the other hand reaches an optimum at intermediate temperatures (460–500°C). Our values (0.128–0.384°) of the FWHM of the XRC for the InN(0002) reflection and the FWHM (4.7–6.7 cm^{-1}) of the E_2(high) phonon mode compare with the best results reported in the literature [19, 42, 60, 63, 64, 66, 122]. However, when we compare the structural and morphological properties of InN with AlN and GaN grown in the same MBE system we see that the InN layers are of inferior quality. The RMS is one order of magnitude higher for the InN films and the FWHM of the (0002) XRC reflection is a factor 2–3 larger.

Table 3.4: Structural and morphological properties of the presented InN layers. We list the growth temperature T_G, the layer thickness d (determined by SEM), the P-V, the RMS, the FWHM of XRC of the InN(0002) reflection and the FWHM of the E_2(high) phonon mode ΔE_2. Samples M8282 and M8456 were grown In-rich. All other samples were grown N-rich.

Sample	T_G (°C)	d (nm)	P-V (nm)	RMS (nm)	FWHM (0002) (°)	ΔE_2 (cm^{-1})
M8282	540	120	59	10.2	0.240	4.7
M8456	375	135	—	—	0.155	—
M8293	500	240	61	9.4	0.200	—
M8294	460	260	68	7.9	0.150	6.4
M8295	460	270	54	5.2	0.827	—
M8301	460	450	83	15.9	0.128	5.4
M8302	460	450	68	6.1	0.146	5.3
M8303	440	500	37	5.2	0.384	—
M8304	420	500	34	4.4	0.360	6.7
Ref. [60]	460	120	—	6	0.402	—
Ref. [59]	550	100	—	10	0.883	—

Optical properties As mentioned in the beginning of this Section, an overwhelming majority of recent publications related to InN report a band gap of 0.7 eV for InN [20, 21, 66, 120, 121] instead of the previous value of 2 eV from Ref. [107].

We determine the band gap of InN by a combination of PL and transmittance measurements. A 10 mW He-Ne laser emitting at 632.8 nm together with a liquid nitrogen cooled Ge photodetector was used for the PL measurements. The optical transmittance was measured by a Fourier-transform spectrometer at 300 K. The spectra were corrected for the spectral response of the system by normalizing them to the spectral response of bare SiC substrates.

Figure 3.14 shows a PL spectrum of sample M8282 performed at 6 K. The spectral position of the PL line is 0.78 eV and its FWHM is 82 meV. The PL peak rapidly diminishes in intensity with increasing temperature until it becomes undetectable at temperatures above 200 K. Concerning the emission from our samples, we found that all samples grown under N-rich conditions exhibit very weak PL signals or none at all. In contrast, the emission intensity of samples grown under In-rich conditions is considerably stronger.

The next Paragraph will show that our layers have very high background carrier concentrations. For sample M8282 the measured unintentional electron concentration is 1.6×10^{20} cm^{-3}. Because of this high background doping, the PL peak energy is a more reliable indicator of the (renormalized) band gap than transmission measurements which are subject to a large Burstein-Moss shift induced by the high carrier density. Therefore, we attribute the PL peak to a band-to-band recombination of electrons from the bottom of the degenerate conduction band to photo-generated holes in the valence band.

The optical transmission spectra of samples M8301–M8303 which are among our thickest InN films (450–500 nm), is shown in Fig. 3.15 (a). From the measured transmittance T, we obtain a zeroth order approximation of the absorption coefficient $\alpha =$

$-\ln(T)/d$. Figure 3.15 (b) shows $(\alpha E)^2$ vs. E, which for parabolic bands should be a straight line and whose extrapolation to zero yields the band edge. We observe that for the three samples shown here, the estimated band gap lies in the range 1.1–1.2 eV. These values are in good agreement with those found in Ref. [119] considering that the background carrier concentration of samples M8301 and M8302, is between 6×10^{19} and 7×10^{19}.

Electrical properties The carrier concentration and the Hall mobility was determined by Hall measurements (van der Pauw geometry) using ohmic Au/Ge contacts. Excess In from the sample mounting was removed by HCl:H_2O(1:3) before the Hall measurements took place.

The results of our electrical characterization of the samples are summarized in Table 3.5. Electron concentrations and mobilities reported from other groups have been included as a comparison. We see that our values compare fairly well with values found in the literature.

In conclusion we observe that samples grown under In-rich conditions have better electrical and optical properties than those grown under N-rich conditions. The surface morphology and crystal quality are similar to N-rich grown samples. However, In-rich grown samples have crystalline In inclusions in the layers as evidenced by XRD [Fig. 3.12] and droplets on the surface. The fact that the dissociation temperature of InN is lower than the desorption temperature of In is the major obstacle in finding the most suitable growth conditions for InN. High temperature growth, which has been employed successfully for GaN and AlN, will inevitably result in accumulation of In which, in turn, leads to droplet formation and In-inclusions. Growing under exact stoichiometric conditions seems to be the only remedy to this problem but this requires an extreme control of the In and N fluxes and is therefore not a practical solution. These suboptimal growth conditions for InN are the reasons for the inferior quality of this material as compared to AlN and GaN layers.

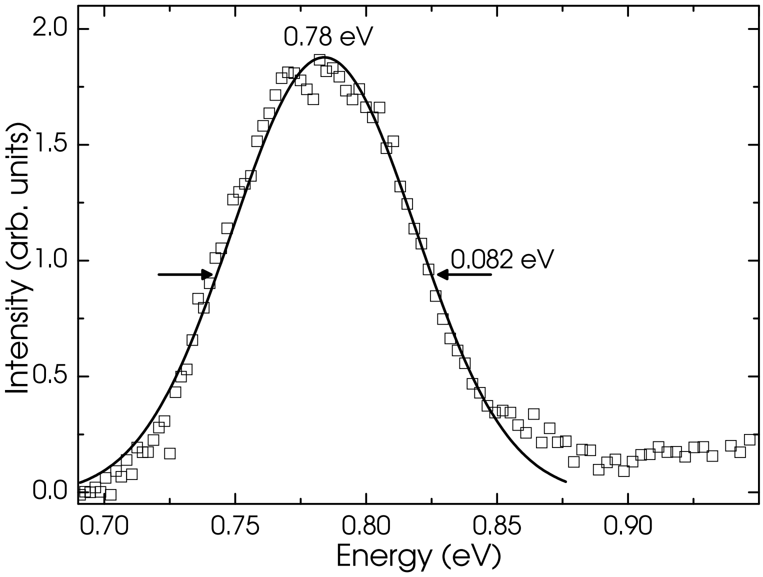

Figure 3.14: PL spectrum at 6 K of sample M8282. The solid line is a Gaussian fit to the data for the determination of the FWHM and the peak energy position.

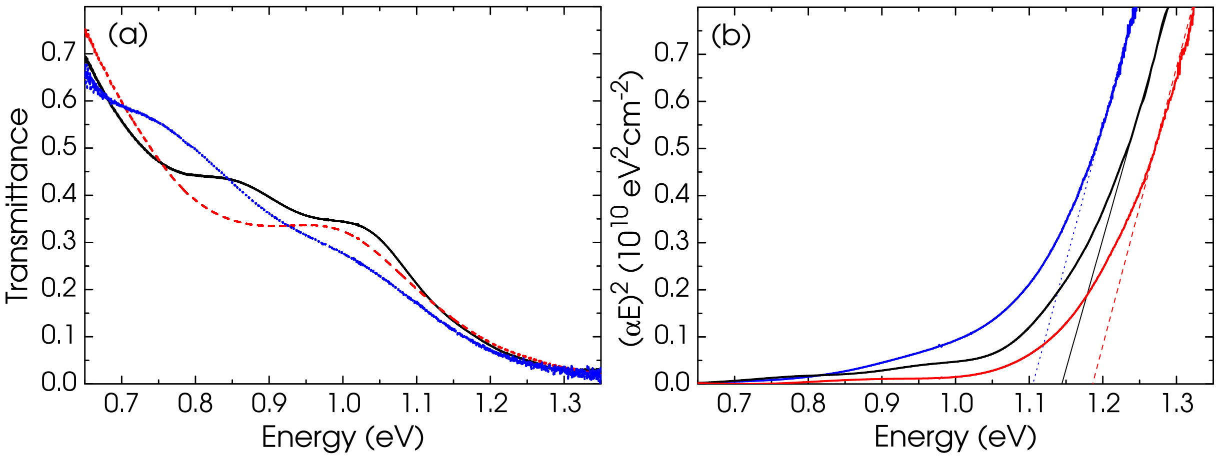

Figure 3.15: Optical transmission spectra recorded at room temperature for samples M8301 (dotted line), M8302 (line) and M8303 (dashed line) (a). The fringes are due to thickness interferences. Squared absorption coefficient vs. photon energy (b). The lines are linear extrapolations down to zero absorption which indicates the band gap for each of the samples.

3.4 Growth of (Al,In)N

(Al,In)N epitaxial layers with an In content of x_{In}=0.18 are lattice matched to GaN. This has two important consequences. Firstly, it allows the growth of crack-free (Al,In)N/GaN Bragg reflectors on low defect density GaN templates. Secondly, it admits a fully epitaxial growth of microcavities. In Refs. [13, 14, 24] both types of structures were successfully demonstrated using metal-organic chemical vapor deposition (MOCVD). Here, the results were excellent with crack-free and coherently grown structures that were more than 2 μm thick. As we will see in Ch. 5 neither growth on GaN templates nor on thick GaN buffer layers, allows fully epitaxially grown microcavities with the AlN/GaN system. These were the main reasons for investigating the (Al,In)N compound.

Table 3.5: Electrical properties of InN epitaxial layers. Listed are the carrier concentration n and the Hall mobility μ.

Sample	n (cm^{-3})	μ (cm^2/Vs)
M8282	1.6×10^{20}	819
M8294	5.6×10^{19}	441
M8301	6.1×10^{19}	441
M8302	6.8×10^{19}	375
M8304	6.5×10^{19}	344
Ref. [64]	1×10^{20}	600
Ref. [27]	4.1×10^{18}	846
Ref. [61]	1.49×10^{18}	1098
Ref. [21]	1.2×10^{19}	1900

One disadvantage with the choice of $Al_{0.82}In_{0.18}N/GaN$ for Bragg reflectors is that the difference in refractive index between $Al_{0.82}In_{0.18}N$ and GaN is smaller than between AlN and GaN (0.23 vs. 0.36). The result is that one has to grow a larger number of $Al_{0.82}In_{0.18}N/GaN$ periods in order to reach the same reflectance as for AlN/GaN based Bragg reflectors. In principle, this does not impose a problem since $Al_{0.82}In_{0.18}N$ is lattice matched to GaN. Therefore, no strain is accumulated which could lead to crack formation. A much harder problem, which will discussed later in this Section, is imposed by the large miscibility gap between InN and AlN.

RHEED All (Al,In)N layers nucleated two-dimensionally on GaN as evidenced by an initially streaky RHEED pattern. The layers were grown under N-rich conditions. After 2–3 minutes a transition from a perfectly streaky RHEED pattern to a pattern with streaks having an undulated shape (modulated streaks), as shown in Fig. 3.16, occurred. From this point, the RHEED pattern remained essentially unchanged throughout the growth but the modulations became slightly more pronounced. At the end of a growth run also a pattern corresponding to facets was usually observed.

Impact of the growth conditions on the surface morphology and the structural quality The sample surfaces were examined by DIC optical microscopy. Symmetric ω-2θ XRD measurements for the GaN(0002) reflection were used to determine the In-content and the film thickness. We used XRD reciprocal space maps to determine the strain state of the samples. The crystal quality was examined by recording x-ray rocking curves across the symmetric (0002) reflection. TEM provided important information about the microstructure of our samples and electron energy loss spectroscopy (EELS) gave information about the layer composition.

We saw in the Sections about AlN and InN that the growth conditions for these two materials are very different. It is therefore expected that growing an (Al,In)N compound might be very difficult. In fact, it is well known that (In,Ga)N is prone to spinodal decomposition due to the large miscibility gap between InN and GaN [39]. This tendency is even more pronounced for (Al,In)N. It has been predicted [65] that in the systems InN–GaN, AlN–GaN and AlN–InN the largest miscibility gap occurs for (Al,In)N. In the following we will see that extreme growth conditions are needed to grow layers with acceptable quality by MBE.

Figure 3.17 shows the phase-diagram deduced from 100–500 nm thick (Al,In)N layers with an In-content varying between 10–30%. All samples were grown on a GaN buffer layer. Homogeneous and crack-free samples were obtained only by choosing the growth parameters from the shaded area. The onset of phase-separation is in the

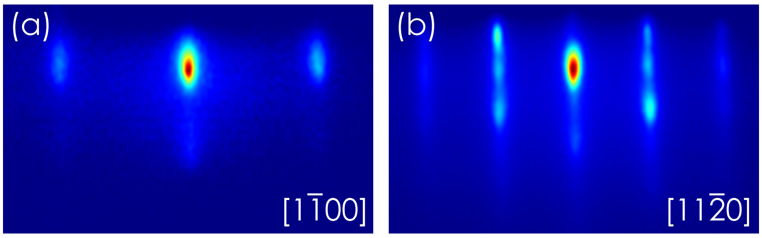

Figure 3.16: RHEED pattern observed for all (Al,In)N layers after 2–3 minutes of N-rich growth on GaN.

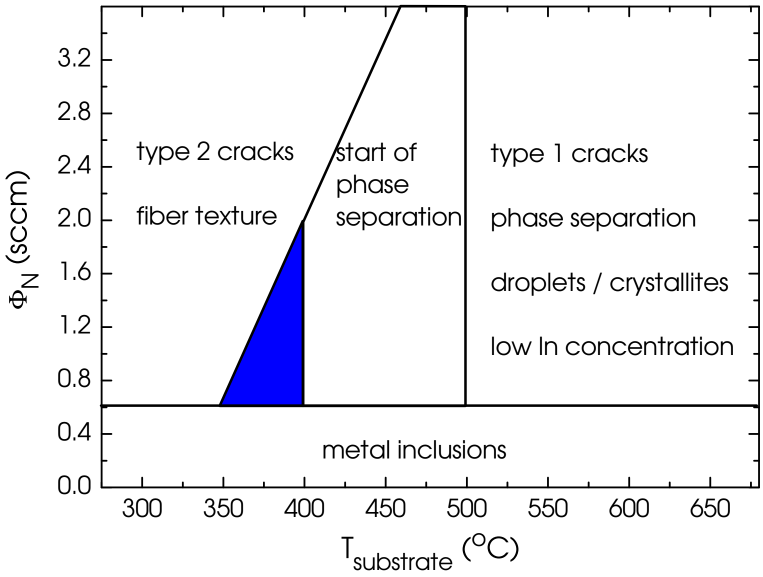

Figure 3.17: Phase diagram of 100–500 nm thick (Al,In)N layers with an In content of 10–30%. All layers were grown on a GaN buffer layer under N-rich conditions. Homogeneous and crack-free samples were obtained only by choosing growth conditions from the shaded area.

400–500°C region. At a temperature higher than 500°C, the segregated InN starts to decompose leaving In droplets on the surface. It becomes increasingly more difficult to incorporate 18% In which is required for the desired lattice matched condition. Practically no In is incorporated at a temperature of 600°C or above. The low In-content leads to crack formation (type 1 cracks) due to the tensile strain that the layer experiences from the underlying GaN buffer layer. It should be noted that at this growth temperature (600°C) (In,Ga)N layers of excellent quality can be grown as has been done in the course of this work.

Figure 3.18 shows a DIC optical microscopy image of a 160 nm thick (Al,In)N sample (M8425) grown at 660°C under extremely N-rich conditions (N-flux of 3 sccm) on a GaN buffer layer. In droplets of varying size can be observed despite the N-rich growth conditions [Ch. 2]. Following the discussion above, these In droplets are the result of segregated InN that has decomposed. The epitaxial film has thus a very low In-content [Fig. 3.19] and is therefore under a high tensile strain due to the GaN buffer. This is the reason for the massive crack formation that is observed in Fig. 3.18.

Figure 3.19 shows an ω-2θ XRD scan for the GaN(0002) reflection of sample M8425 which was grown at 660°C on a GaN buffer layer. A weak and broad $Al_{0.92}In_{0.08}N$ peak can be observed. This layer of low In content experiences a large tensile strain from the underlying GaN buffer layer. The result is a massive crack formation as observed in Fig. 3.18. We can also see a crystalline In related peak [-1.32° relative to SiC(0006)] which is the consequence of phase segregation [Fig. 3.18]. The cause of this In peak is that the segregated InN is decomposing since the growth temperature of 660°C is above the dissociation temperature for InN.

A cross-sectional TEM micrograph of a sample grown at 600°C is shown in Fig. 3.20. Phase separation can be observed in the form of 0.5–0.6 μm wide In-rich polycrystalline remnants of In-droplets. The layer between the droplets have a low and very inhomogeneous In-content (6–14%) as revealed by EELS measurements. A very interesting finding is that this layer actually is comprised of a self-organized superlattice consisting of alternating In-rich and In-poor (Al,In)N layers with a period of 13–14 nm. The period is not a result of the sample rotation because it would yield a period of 0.7 nm. These features are therefore the effects of the phase separation and has indeed been predicted recently in Ref. [18]. Figure 3.21 shows a magnification of the layer. The white arrows indicate the periods. The layer grows through a columnar growth mode. The columns are 50–100 nm wide and show a low tilt but a large twist.

Type 2 cracks In order to avoid type 1 cracks and droplets, we drastically lowered the growth temperature down to 300–375°C. This action inhibits the phase separation and increases the In-content in the (Al,In)N layers. As mentioned, the effect of the low In-content in the samples grown at high temperatures, was that the underlying GaN buffer layer induced a high tensile strain in the low In-content (Al,In)N layer. The high

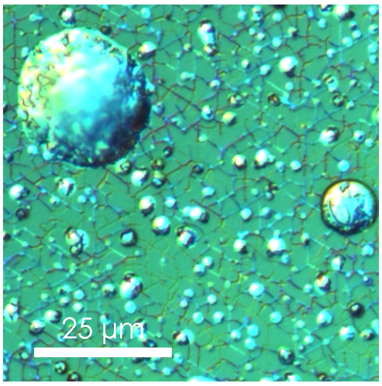

Figure 3.18: DIC optical microscopy image of sample M8425 which was grown at 660°C under extremely N-rich conditions on a GaN buffer layer. In droplets of varying size and a network of cracks are visible.

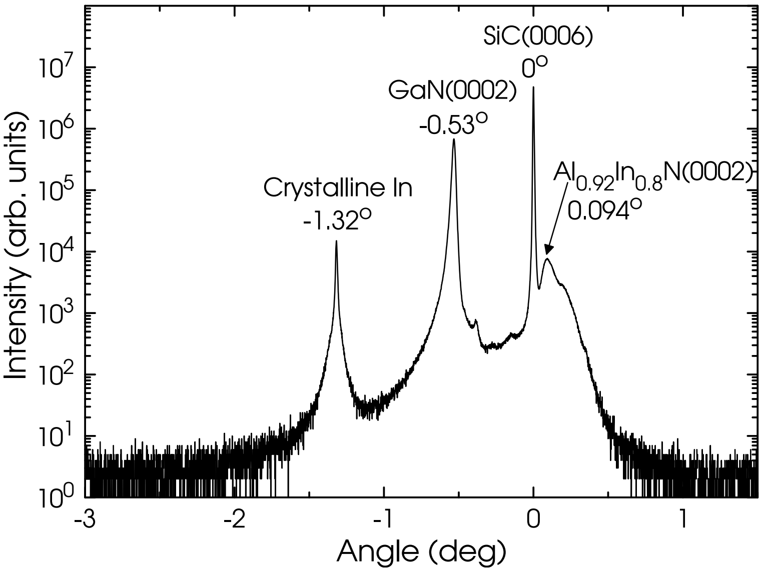

Figure 3.19: XRD ω-2θ scan for the GaN(0002) reflection of sample M8425 grown at 660°C under extremely N-rich conditions on a GaN buffer layer. A weak and broad $Al_{0.92}In_{0.08}N$ peak is visible very close to the SiC(0006) peak. Crystalline In contained in either droplets or inclusions is giving rise to the peak just left of the GaN(0002) peak. All peak positions are relative to the SiC(0006) peak position.

tensile strain lead to crack formation.

Our samples grown in the 300–375°C range have an In-content between 11 and 27%. The low growth temperature allowed a good control over the In incorporation and we could therefore achieve the desired In-content of 18% required for lattice matching.

Figure 3.22 shows DIC optical microscopy images of the surfaces of three samples grown at 375°C (a) and 300°C (b–c). We used a nitrogen flux of 2.0 sccm for all samples which are 140–200 nm thick. The In-contents are 26.6% (a) and 18.5 and 17.5%, respectively in (b) and (c). The sample in (a) should be under a strong compressive strain whereas the samples in (b) and (c) should be very close to lattice matched conditions.

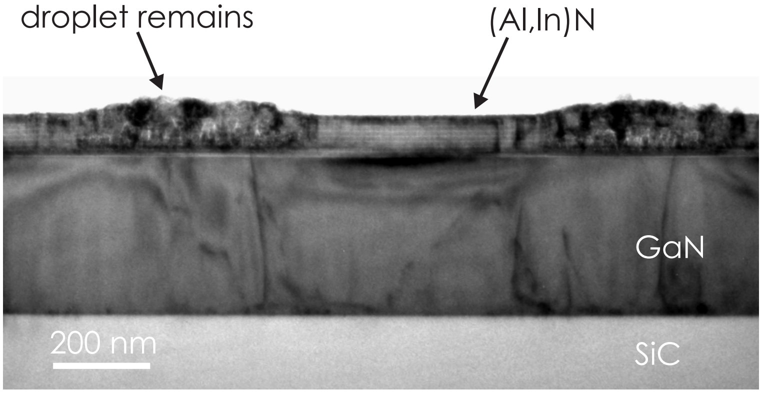

Figure 3.20: Cross-sectional TEM micrograph of a sample grown at 600°C. Large In-rich polycrystalline In-droplet remnants are observed. The layer between the droplets has a low and very inhomogeneous In-content.

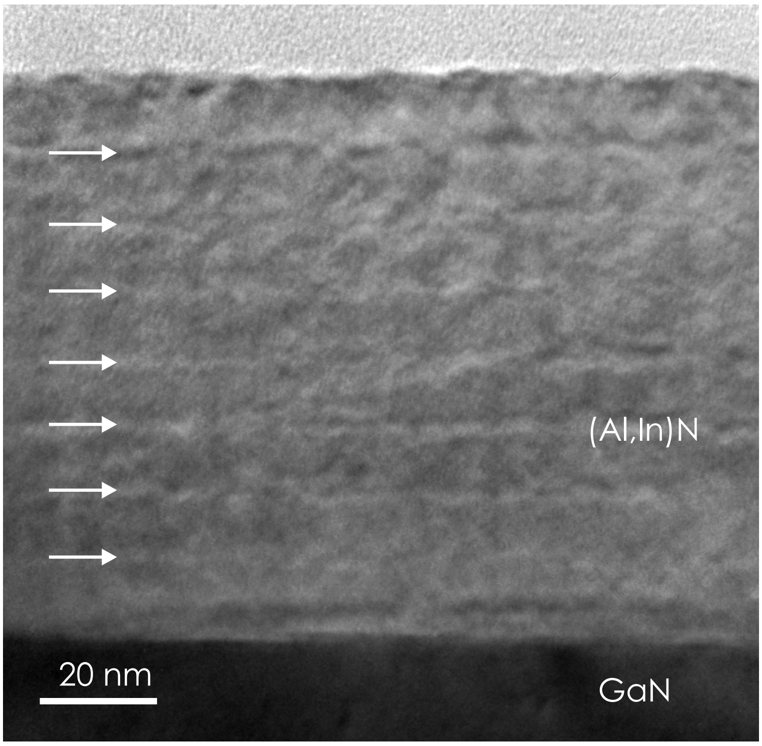

Figure 3.21: Self-organized superlattice consisting of alternating In-rich and In-poor (Al,In)N layers with a period of 13–14 nm. This micrograph is a magnification of the (Al,In)N layer depicted in Fig. 3.21. The white arrows indicate the periods.

We see that the surface morphology is similar in all cases. A dense network of small hairline thick cracks and less dense large cracks are visible in all samples. We can also see region where the epitaxial film has completely detached from the substrate surface. These very thin free standing regions give rise to the optical interference fringes visible particularly well in (a).

Essentially all films grown under similar low temperature conditions as the samples shown in Fig. 3.22 and with the right In-content of 18%, exhibited cracks. This was a very surprising finding because layers under a slight compressive strain ($0.20 > x_{\text{In}} > 0.18$) or under lattice matched conditions ($x_{\text{In}}=0.18$) should in principle not show any cracks. For this reason we denote this type of cracks as type 2 cracks emphasizing that their origin is different from the origin of the type 1 cracks.

Figure 3.23 shows an ω-2θ XRD measurement for the (Al,In)N(0002) reflection that is typical for all low temperature grown samples. The uppermost curve in Fig. 3.23 (a) shows the experimental data from a 126 nm thick $\text{Al}_{0.73}\text{In}_{0.27}\text{N}$ layer and the lowest curve is a fit to the experimental data. We see that we can fit the main peak positions and the widths correctly. The simulated interference fringes though, have an intensity that is too low. We see also that the shape of the simulated curve is different. An acceptable fit can only be achieved by including a strain gradient [Fig. 3.23 (b)]. Here, we assume that the layer is experiencing a progressively larger tensile strain evolving 20 nm into the layer from the GaN/$\text{Al}_{0.73}\text{In}_{0.27}\text{N}$ interface. At a first glance, this is expected since an In-content of 27% yields an in-plane lattice constant a that is larger than that of GaN and therefore the layer relaxes. However, the same behavior is observed even for samples that have the desired In-content of 17–18% which is required for the layers to be lattice matched to GaN. It should be emphasized that for these apparently lattice matched samples we have to assume that the strain gradient is evolving from a strain-free lattice matched state at the GaN/(Al,In)N interface to a gradually larger tensile strain. This is a seemingly paradoxical assumption because there is, at first glance, no reason for a layer that is lattice matched to the buffer layer, to be under tensile strain. Nevertheless, the RSM displayed in Fig. 3.24 shows that this is indeed the case. Figure 3.24 depicts a RSM obtained from a 170 nm thick (Al,In)N layer with an In-content of 17%. It is therefore lattice matched or nearly lattice matched to GaN. The contour plot shows that there are two peaks related to the (Al,In)N layer. One of the

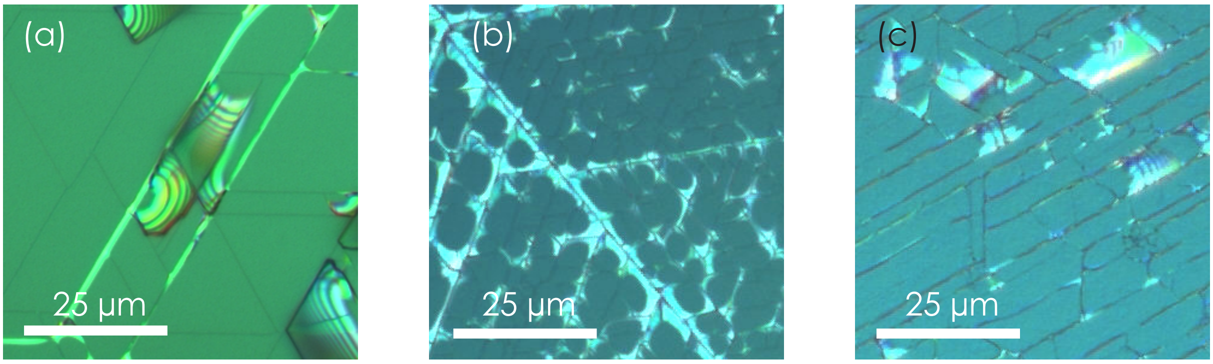

Figure 3.22: DIC optical microscopy images of the surfaces of three samples grown at 375°C (a) and 300°C (b–c). The In-contents are 26.6% (a) and 18.5 and 17.5% in (b) and (c), respectively. The surface morphology is very similar in all images. Regions where the epitaxial film have completely detached from the substrate surface give rise to the optical interference fringes visible particularly well in (a).

peaks [coherent (Al,In)N in Fig. 3.24] is on the same horizontal position (black dashed line in Fig. 3.24) as the peak related to the GaN buffer layer. Because a shift in the horizontal position in a RSM corresponds to a shift of the in-plane lattice constant a we can conclude that the part of the (Al,In)N layer closest to the GaN buffer layer has the same a as GaN. It is thus coherent to the underlying GaN buffer layer. The second peak [strained (Al,In)N in Fig. 3.24] lies to the left of the GaN peak which means that the a value is larger than that of GaN. We can immediately compare the in- (a) and out-of-plane (c) lattice constants for the two (Al,In)N peaks because a vertical shift in a RSM directly corresponds to a shift of c. The in- and out-of-plane lattice constants are related through Poisson's relations and Vegard's law. The results calculated from these relations should be fairly consistent with the results from the RSM. However, when using Vegard's law both with and without bowing [58] and Poisson's relations a large discrepancy is found when compared to the results from the RSM.

We examined our low temperature grown samples by TEM in order to better understand the contradicting XRD results and ultimately the cause for the type 2 cracks. Figure 3.25 shows a cross-sectional TEM micrograph of a 145 nm thick $Al_{0.79}In_{0.21}N$ sample grown at 300°C with an N-flux of 2.0 sccm. No phase separation can be observed. In addition, EELS measurements show that In has been incorporated homogeneously in the layer. As in the case of the high temperature grown samples, the layer exhibits columnar growth but here the width of the columns is much smaller (20–40 nm). Skew geometry XRD measurements reveal that the columns have a small tilt but a large twist (2°) which also is in line with high temperature grown samples. Despite of the much higher quality of this layer we can observe cracks as indicated by the black arrows in Fig. 3.25.

Based on the results from the XRD and TEM measurements, it will be shown in the following that the formation of type 2 cracks can be explained by tensile stresses induced by crystallite coalescence and grain boundary formation as proposed by Nix and Clemens [85].

The low growth temperature and the high N-flux results in a columnar growth of (Al,In)N. These 20–40 nm wide columns have a small tilt but a considerable twist of

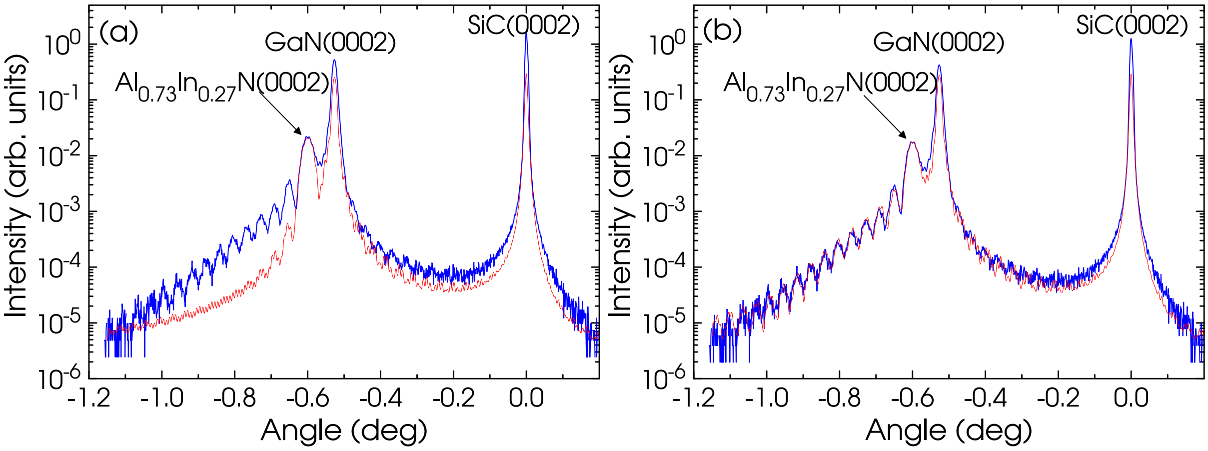

Figure 3.23: X-ray ω-2θ scan for the (Al,In)N(0002) reflection. The uppermost curve is the experimental data and the lowermost is a fit. In (a) the fit is done without a strain gradient. In (b) a strain gradient is included yielding an almost perfect fit (lower curve) to the experimental data (upper curve).

≈ 2°. Columns with an In-content of 16–18% grow initially coherent (a_{GaN}=$a_{(Al,In)N}$) to the GaN buffer layer. This means that there are no misfit dislocations at the GaN/(Al,In)N interface, which is in agreement with the TEM results. As the growth progresses, the column surfaces spontaneously start "snapping" together thereby forcing the columns to coalesce and to form grain boundaries. This occurs since after the formation of grain boundaries the system will have an energy that is lower than the energy needed for sustaining free column surfaces.

The coalescence process causes a gradual build-up of elastic tensile strain in the growing columns despite the fact that they are lattice matched or nearly lattice matched to GaN. This gradual change of the lattice constants is what we observe in our XRD measurements. The tensile strain can be relaxed if enough material is reaching the

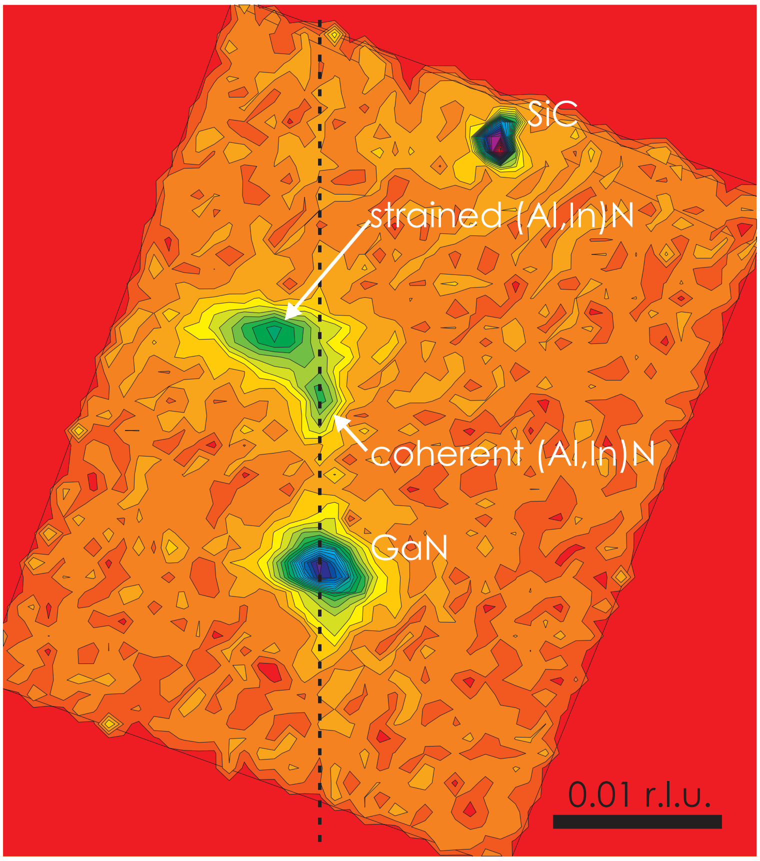

Figure 3.24: Reciprocal space map of a 168 nm thick $Al_{0.83}In_{0.17}N$ layer grown at 300°C with a N-flux of 2 sccm. Indicated are the peaks corresponding to the SiC substrate, the GaN buffer layer and the coherent and strained $Al_{0.83}In_{0.17}N$.

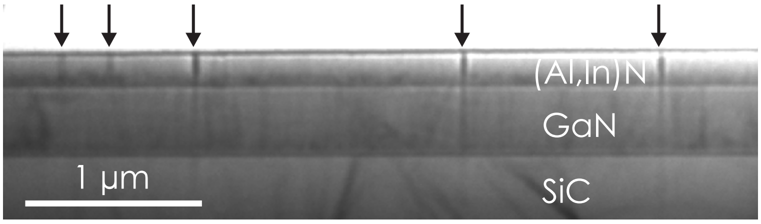

Figure 3.25: Cross-sectional TEM micrograph of a 145 nm thick $Al_{0.793}In_{0.207}N$ sample grown at 300°C with an N-flux of 2.0 sccm. The black arrows indicate cracks in the layer.

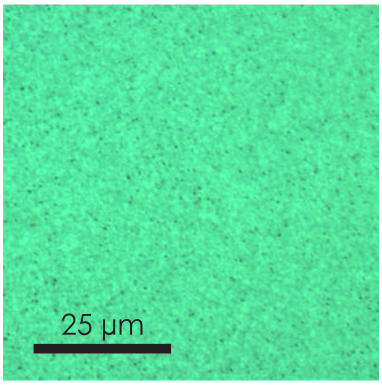

Figure 3.26: DIC optical microscopy image of a 600 nm thick sample grown under growth conditions chosen from the shaded area of Fig. 3.17. No cracks can be observed.

grain boundaries. However, at the employed low temperature and high N-flux the adatom mobility is so low that the incoming atoms are incorporated very close to their arrival point. The tensile strain increases and at a certain thickness it becomes so high that the layer cracks.

Intermediate region The solution to the cracking problem discussed in the previous paragraph is to increase the adatom mobility. This can be achieved by increasing the growth temperature, decreasing the N-flux and decreasing the growth rate. All these proposed actions are however, limited to a very narrow window since an increase of the adatom mobility promotes phase separation. Indeed, samples exhibited phase separation and InN crystallite formation already at a growth temperature as low as 450°C. The metal-rich growth conditions that are commonly used for the growth of many nitrides to increase the adatom mobility, cannot be used here because they give rise to metal inclusions in the layer and, eventually, they lead to a transition to polycrystalline growth.

Our growth experiments show that by choosing the growth conditions from the shaded area in Fig. 3.17 (corresponding to a growth rate of $\approx$ 200 nm/h), homogeneous and crack-free layers up to a thickness of 600 nm can be obtained. Figure 3.26 shows a DIC optical microscopy image from the surface of a crack-free 600 nm thick $Al_{0.8}In_{0.2}N$ sample grown at 400°C with an N-flux of 1 sccm. An ω-2θ XRD scan of this sample is shown in Fig. 3.27. We achieve a good agreement between simulation and experimental data without including a strain gradient. These results seem to clear the path to (Al,In)N/GaN based Bragg reflectors which are discussed in Ch. 6.

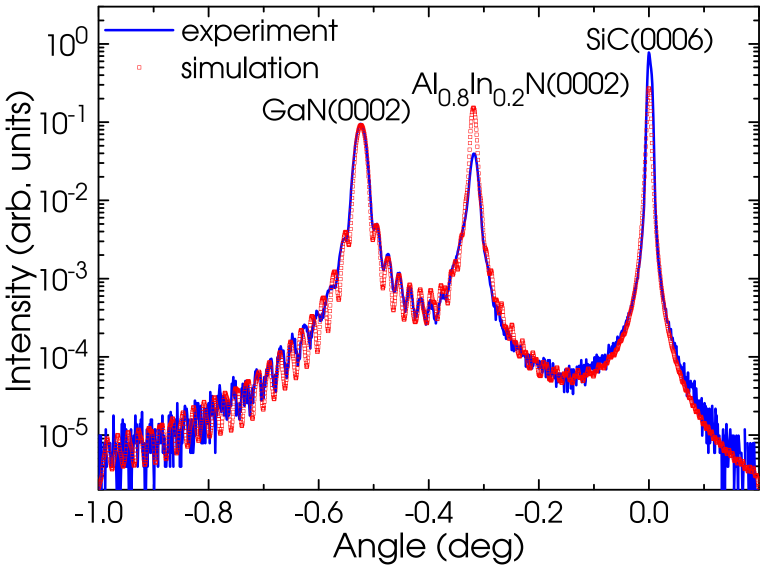

Figure 3.27: XRD ω-2θ XRD scan for the GaN(0002) reflection of the sample shown in Fig. 3.26. No strain gradient was needed to fit the experimental data.

Chapter 4

Fundamentals of Bragg reflectors

A brief introduction is given here to the theoretical framework behind Bragg reflectors in general and how this theory is applied to (Al,Ga,In)N based Bragg reflectors in particular. After introducing the notion of quarter-wave layers, the transfer matrix method is described in the context of the well-known problem of calculating the theoretical reflectance for a single boundary between two semi-infinite media. The transfer matrix method is extended to the case of a single layer which finally is extended once again to include periodic layered structures such as Bragg reflectors. This successive extension—from a single boundary to a single film to a multilayer structure—will show the great advantage of using transfer matrices.

4.1 Theoretical reflectance and bandwidth

It is well known that when light is going from a material with a lower refractive index to a material with a higher refractive index, the phase of the reflected wave is shifted π radians with respect to the incident wave (going from higher to lower refractive index produces no phase shift) [9, 33]. Therefore, in a thin, homogeneous and isotropic film with a uniform thickness d corresponding to

$$d = \frac{\lambda}{4n} \tag{4.1}$$

where λ is the wavelength of the incident light and n is the refractive index of the film, the reflected waves from the front and back surfaces are in phase and give rise to constructive interference. This statement applies provided that the film is bounded by media of different refractive indices. Such a film is called a quarter-wave layer. A periodic layered structure consisting of alternating quarter-wave layers of two different materials with different refractive indices will exhibit resonance reflection at a certain wavelength. This is analogous to the diffraction of x-rays by crystal lattice planes. For this reason, such a structure is called a Bragg reflector. The distance between the crystal lattice planes in the x-ray case, is analogous to the Bragg reflector period P which is given by adding the thicknesses of the two quarter-wave layers of which the period consists

$$\mathrm{P} = d_1 + d_2 = \lambda \left(\frac{1}{4n_1} + \frac{1}{4n_2} \right). \tag{4.2}$$

By designing these structures properly, a reflectance equal to or exceeding 0.99 can be obtained. In comparison, high-reflectance metal mirrors have reflectances that vary between 0.99 and 0.9 in the near-IR and visible spectrum. For example, a silver mirror has a reflectance of 0.987 for IR light (1240 nm) and 0.864 for deep-violet light (413 nm) [117]. Aluminum mirrors have a slightly higher reflectance at shorter wavelengths, 0.924 for deep-violet light [117]. These values are too low for devices such as VCSELs that rely on a very high reflectance. Bragg reflectors are therefore necessary to implement these devices. In addition, the peak reflectance wavelength of a Bragg reflector is, through the relation $d = \lambda/(4n)$, a design parameter. By changing the layer thicknesses, the peak reflectance wavelength can be adjusted to occur at any desired wavelength in, for instance, the visible spectrum.

The general expression for the reflectance is obtained by considering the classical problem of incident, reflected and transmitted plane electromagnetical (EM) waves of visible frequencies at a boundary between two transparent media. A solution to this problem is given by applying Maxwell's equations for the electric and magnetic fields at the boundary together with the related boundary conditions which require that the tangential components of the electric and magnetic waves are continuous at the interface. The result are equations that give the amplitudes of the transmitted and reflected waves in terms of the incident wave. Since we consider homogeneous and isotropic media, the s- or TE- and p- or TM-polarized waves are independent of each other and can be treated separately.

In the following the s-polarized case is treated. The electric field E is parallel to the y-axis and is assumed to travel in the xz-plane [Fig. 4.1(a)]. Further, the angle of incidence is assumed to be below the critical angle θ_c for total reflection. The field is written as the sum of a right- and a left-traveling wave $E = A_R e^{-ik_x x} + B_L e^{-ik_x x} = A(x) + B(x)$ where k_x is the x-component of the wave vector and A_R and B_L are constants in each medium.

By introducing a matrix formulation [124, 125], the relation between incident, reflected and transmitted wave amplitudes of the s-polarized wave at an interface between two semi-infinite media can be written in a very compact form as

$$D_0 \begin{pmatrix} A_0 \\ B_0 \end{pmatrix} = D_1 \begin{pmatrix} A_1' \\ B_1' \end{pmatrix} \Leftrightarrow \begin{pmatrix} A_0 \\ B_0 \end{pmatrix} = D_0^{-1} D_1 \begin{pmatrix} A_1' \\ B_1' \end{pmatrix} \tag{4.3}$$

where A_0 and B_0 are the tangential components of the electrical field of the s-polarized wave for the incident and reflected waves of medium 0 at the boundary [Fig. 4.1(a)]. Further, A_1' denotes the tangential component of the electrical field of the transmitted s-polarized wave of medium 1 at the boundary and D_j is the so called dynamical matrix for the s-polarized light

$$D_j = \begin{pmatrix} 1 & 1 \\ n_j \cos(\theta_j) & -n_j \cos(\theta_j) \end{pmatrix}, j = 0, 1 \tag{4.4}$$

where n_j is the complex refractive index and θ_j the angle of the incident light of medium j, respectively. Note that the B_1' component is zero in the case of a single

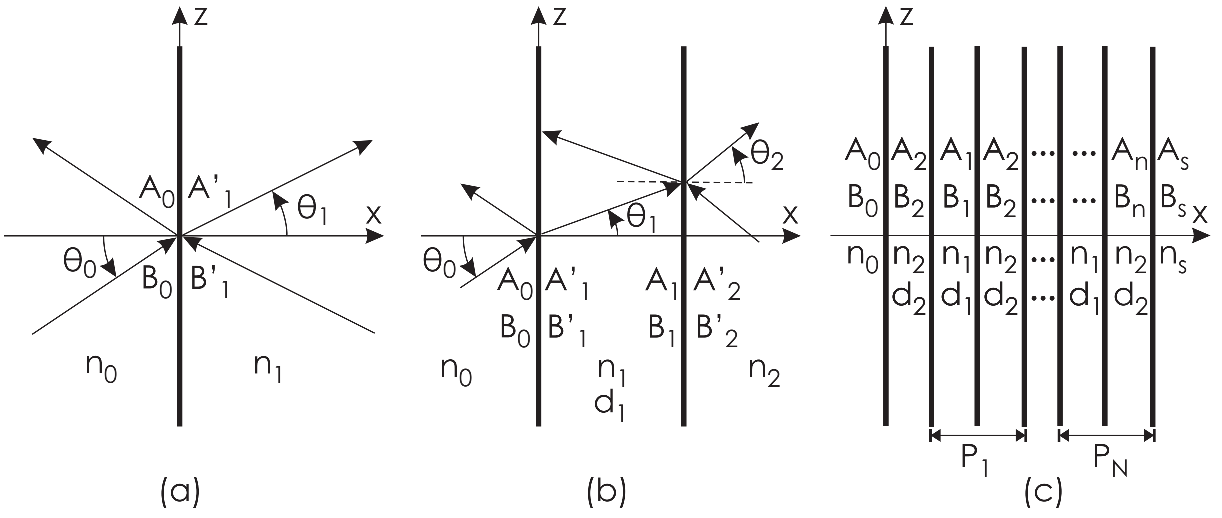

Figure 4.1: Geometrical configuration for a boundary between two semi-infinite media (a), for a thin film of a finite thickness bounded by two different materials (b), and for a periodic layered structure (c). The symbols are defined in the text.

boundary between two semi-infinite media. From Eq. 4.3 the definition of the reflectance for the s-polarized light R_s is given as

$$R_s = \left|\frac{B_0}{A_0}\right|^2 = |r_s|^2 = \left|\frac{n_0\cos(\theta_0) - n_1\cos(\theta_1)}{n_0\cos(\theta_0) + n_1\cos(\theta_1)}\right|^2 \tag{4.5}$$

where r_s is Fresnel's reflection coefficient for s-polarized light. Thus, R_s is the ratio between the tangential components at the boundary of the incident and the reflected waves.

If we extend the single boundary case to the case of having a thin film or layer of a finite thickness d_1 bounded by two different semi-infinite media [Fig. 4.1(b)], the wave amplitudes at the two interfaces within the film are related by

$$\begin{pmatrix} A_1' \\ B_1' \end{pmatrix} = P_1 \begin{pmatrix} A_1 \\ B_1 \end{pmatrix} \tag{4.6}$$

where

$$P_1 = \begin{pmatrix} e^{i\phi_1} & 0 \\ 0 & e^{-i\phi_1} \end{pmatrix} \tag{4.7}$$

is the propagation matrix which describes the wave propagation in the film and ϕ_j signifies the phase given by

$$\phi_1 = k_1\cos(\theta_1)d_1 = k_{1x}d_1 = \frac{2\pi n_1 d_1}{\lambda}\cos(\theta_1) \tag{4.8}$$

where k_j is the absolute value of the wave vector and λ is the wavelength of the incident light, respectively.

By successively applying Eq. 4.3 at each of the interfaces

$$\begin{pmatrix} A_0 \\ B_0 \end{pmatrix} = D_0^{-1}D_1 \begin{pmatrix} A_1' \\ B_1' \end{pmatrix} \tag{4.9}$$

$$\begin{pmatrix} A_1 \\ B_1 \end{pmatrix} = D_1^{-1} D_2 \begin{pmatrix} A_2' \\ B_2' \end{pmatrix} \tag{4.10}$$

together with with Eq. 4.6 we can relate the components A_0, B_0 and A_2' and A_2' through

$$\begin{pmatrix} A_1 \\ B_1 \end{pmatrix} = D_0^{-1} D_1 P_1 D_1^{-1} D_2 \begin{pmatrix} A_2' \\ B_2' \end{pmatrix} = M \begin{pmatrix} A_2' \\ B_2' \end{pmatrix} = \begin{pmatrix} M_{11} & M_{12} \\ M_{21} & M_{22} \end{pmatrix} \begin{pmatrix} A_2' \\ B_2' \end{pmatrix} \tag{4.11}$$

where M is called the transfer matrix. Here B_2' is zero since only a transmitted wave exists in this medium. From Eq. 4.11 we obtain the reflectance as

$$R_s = \left| \frac{B_0}{A_0} \right|^2 = \left| \frac{M_{21}}{M_{11}} \right|^2 \tag{4.12}$$

where M_{11} and M_{21} are given in Eq. 4.11. We observe that in Eq. 4.11 each interface is represented by a dynamical matrix of the corresponding bounding media and that the phase shift is represented by a propagation matrix. This observation makes the expansion to a periodic structure such as a Bragg reflector straightforward. If we consider a Bragg reflector [Fig. 4.1(c)] having N periods where each period consists of two quarter-wave layers made of materials 1 ($j = 1$) and 2 ($j = 2$), the transfer matrix is given by

$$M = D_0^{-1} D_2 P_2 D_2^{-1} \left(D_1 P_1 D_1^{-1} D_2 P_2 D_2^{-1} \right)^{\mathrm{N}} D_s \tag{4.13}$$

where D_0 and D_s correspond to the dynamical matrices of air ($n_0 \approx 1$) and the substrate, respectively. The substrate and the air are considered as semi-infinite media. Equation 4.12 gives the reflectance as $R_s = |M_{21}/M_{11}|^2$.

The derivation of the corresponding equations for the p-polarized EM wave is completely analogous to the s-polarized case and the form of the equations is the same even if the equations themselves are different.

If we consider light at normal incidence ($\phi_{1,2} = \pi/2$) the equation for the reflectance of s-polarized light equals that of p-polarized light $R = R_s = R_p$. In the following only normal incidence is considered. For device applications, this is a simple, but very important special case that yields the maximum possible reflectance (assuming that the angle of incidence is above the critical angle θ_c for total internal reflection). Figure 4.2 shows a calculated reflectance spectrum based on Eq. 4.12 of a 20-period Bragg reflector consisting of alternating AlN and GaN quarter-wave layers which are 53.4 nm (AlN) and 45.5 nm (GaN) thick. The light is incoming at normal incidence and the indices of refraction used are $n_1 = 2.1$, $n_1 = 2.5$, $n_0 = 1$ and $n_s = 2.7$ for AlN, GaN, air and the SiC substrate, respectively. The peak reflectance occurring at 450 nm (blue color) is 0.997. We see that the Bragg reflector exhibits a wide high-reflectance region which is called a stopband. The stopband is symmetrically positioned around the peak reflectance wavelength λ_0. The BW of the stopband is given by

$$\Delta\lambda = \lambda_0 \frac{4}{\pi} \arcsin\left(\frac{|n_2 - n_1|}{n_2 + n_1} \right). \tag{4.14}$$

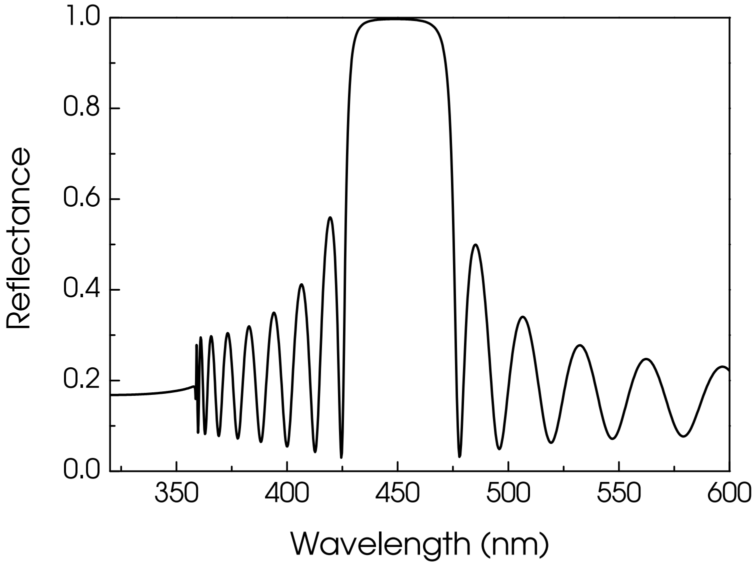

Figure 4.2: Reflectance of a 20-period AlN/GaN Bragg reflector as a function of the wavelength of the incident light. The refractive indices used are $n_1 = 2.1$, $n_2 = 2.5$, $n_0 = 1$ and $n_s = 2.7$ and correspond to AlN, Gan, air and SiC, respectively. The peak reflectance is 0.997 at 450 nm for AlN and GaN quarter-wave layer thicknesses of 53.4 and 45.5 nm, respectively.

With $n_1 = 2.1$ and $n_2 = 2.5$ the BW equals to ≈50 nm. The smaller peaks in Fig. 4.2 come from interference of wavelengths away from the peak reflectance wavelength. The imaginary part k of the complex refractive index $n + ik$ gives rise to optical absorption. When the incoming light has an energy that is below the bandgap of a material the effect of the imaginary refractive index is negligible and only the real part n has an effect. The material is transparent for the incoming light. When the energy of the light is approaching the bandgap the imaginary part of the complex refractive index increases rapidly and the material is becoming opaque. At approximately 360 nm the GaN layers (medium 2) start to absorb the incoming light. This is why the interference fringes abruptly disappear above 360 nm. The complex refractive index will be discussed in the next section. Since the substrate is regarded as semi-infinite there is no interference arising from the back side of the substrate.

It is useful to rewrite Eq. 4.13 as

$$R = R(N) = \left(\frac{1 - \frac{n_2^2}{n_s n_o} \left(\frac{n_1}{n_2} \right)^{2N}}{1 + \frac{n_2^2}{n_s n_o} \left(\frac{n_1}{n_2} \right)^{2N}} \right)^2 \tag{4.15}$$

because we can then clearly see the relation between the peak reflectance and the number of periods N. Figure 4.3 shows the maximum achievable reflectance as a function of the number of periods N for a Bragg reflector designed for three different peak reflectance wavelengths at normal incidence. When N becomes very large the reflectance approaches 1. The refractive indices are the same as for the Bragg reflector used for the simulation depicted in Fig. 4.2 ($n_1 = 2.1$, $n_2 = 2.5$, $n_0 = 1$ and $n_s = 2.7$).

From Eqs. 4.14 and 4.15 we see that a large difference $|n_2 - n_1|$ between the refrac-

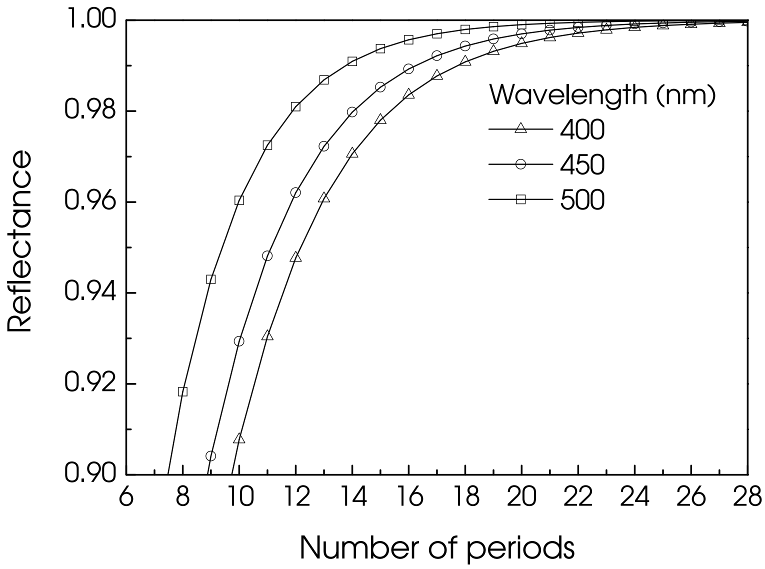

Figure 4.3: Theoretical maximum reflectance per number of periods for an AlN/GaN Bragg reflector designed for different peak reflectance wavelengths. The refractive indices used are $n_1 = 2.1$, $n_2 = 2.5$, $n_0 = 1$ and $n_s = 2.7$ for AlN, GaN, air and SiC, respectively.

tive indices of the materials that constitute the period yields a large BW and a high reflectance with a minimum number of periods. This leads to the conclusion that materials for Bragg reflectors should be chosen in such a way that they maximize the difference of the refractive indices of the materials. In the case of nitride based Bragg reflectors this is a choice that comes at a high price as we will see in the next section.

Complex refractive index It is evident from the treatment in the first section that the refractive index n plays a central role in determining the quarter-wave layer thickness, the number of periods needed for a certain desired reflectance and the BW. Of course, in order to reliably calculate the reflectance for a Bragg reflector, it is important to use accurate values for n.

The refractive index n constitutes the real part of the complex refractive index N which is defined as

$$N = n + ik \tag{4.16}$$

where k is the so called extinction coefficient. The complex refractive index is related to the frequency dependent dielectric function or constant ϵ of a material through

$$N^2 = \epsilon = \epsilon(\omega) \tag{4.17}$$

where ω is the angular frequency of the incident light. The dielectric function can be separated into a real and imaginary part according to

$$\epsilon = \epsilon_1 + i\epsilon_2 \tag{4.18}$$

where $\epsilon_1 = \epsilon_1(\omega)$ and $\epsilon_2 = \epsilon_2(\omega)$ correspond to the frequency dependent real and imaginary parts, respectively, which are related to n and k by

$$\epsilon_1 = n^2 - k^2 \tag{4.19}$$

$$\epsilon_2 = 2nk. \tag{4.20}$$

The optical constants n and k describe the dispersion and the absorption in a material, respectively. They can be determined by measuring the transmittance and the reflectance. For normal incidence the intensities of the transmitted light I_t and the reflected light I_r are given by

$$I_t = I_0 \frac{\left(1 - R^2\right) e^{-\alpha d}}{1 - R^2 e^{-2\alpha d}} \left(1 - \frac{n^2}{k^2}\right) \tag{4.21}$$

$$I_r = I_0 R \frac{1 - e^{-2\alpha d}}{1 - R^2 e^{-2\alpha d}} \tag{4.22}$$

where I_0 is a constant and d is the thickness of the layer and where α is the absorption coefficient which is defined as

$$\alpha = \frac{2\omega k}{c} \tag{4.23}$$

and R is the reflection coefficient which for normal incidence is

$$R = \frac{(n-1)^2 + k^2}{(n+1)^2 + k^2}. \tag{4.24}$$

We determined the refractive indices of AlN and GaN by variable angle spectroscopic ellipsometry (VASE). Our values compare very well to the measurement data given in Ref. [91] which are considered to be the most accurate and reliable to date. Reference [91] also provides a model that accurately fits the presented data points and that gives a smooth transition at the bandgap and above. Any accurate calculation of the dielectric function near the bandgap edge of a semiconductor should include the effects of optical absorption by excitons. Such a model which accounts for the excitonic absorption near the bandgap, was presented in the work of Elliott [25]. In this work the band-to-band absorption is modified by a factor which analytically expresses the excitonic contribution to the absorption. Sometimes this factor is called the Sommerfeld factor [16].

The Kramer-Kronig relations (KKR) [9, 126] provide a link between absorption and dispersion and makes it possible to obtain the expression for the dispersion if the expression for the absorption is known and vice versa. However, the mathematical treatment of applying KKR on an expression that includes the Sommerfeld factor is very cumbersome. Therefore, the Sommerfeld factor is often approximated to a much simpler function or omitted completely in order to be able to apply KKR. Despite the mathematical difficulties, a correct application of KKR on the full expression including the Sommerfeld factor has been performed in Ref. [84]. The following expression is based on Ref. [84] and gives the DF both below and above the bandgap (DF $\equiv \varepsilon_e$) as

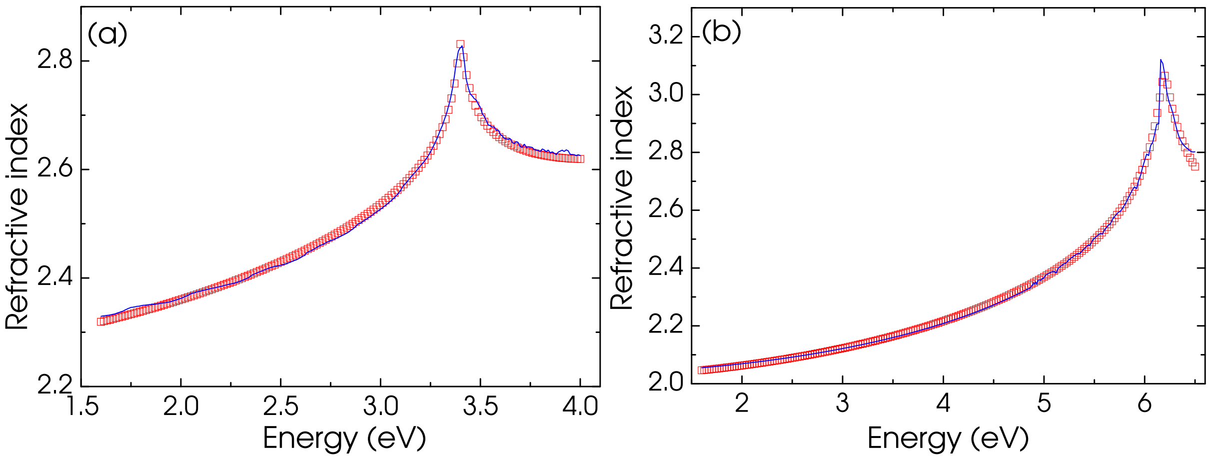

Figure 4.4: Experimental (line) refractive index from spectroscopic ellipsometry measurements and simulated (squares) refractive index for GaN (a) and AlN (b).

$$\varepsilon_e = \varepsilon_{1X} + b_X E^2 - a_X \left\{ \ln\left[\left(\frac{E-E_g}{\gamma}\right)^2 + 1\right] + \ln\left[\left(\frac{E+E_g}{\gamma}\right)^2 + 1\right] - i\left[\frac{2\arctan\left(\frac{E-E_g}{\gamma}\right) + 2\arctan\left(\frac{E+E_g}{\gamma}\right)}{1+e^{\left(E_g-E\right)/\gamma}}\right]\right\} \tag{4.25}$$

where ε_{1X}, b_X and a_X are constants. The photon energy and the bandgap are denoted as E and E_g, respectively and γ is a broadening-factor, which depends on the quality of the crystal. Equation 4.25 does not include the effect of the discrete excitonic states because the impact on the refractive index is negligible at room temperature. If primarily the absorption is sought then one should include the discrete states.

To obtain the refractive indices for bulk GaN and AlN we fit Eq. 4.25 to our AlN and GaN VASE data [Fig. 4.4]. This fit is used for accurate calculations of quarter-wave layer thicknesses and for simulations of reflectance spectra. It also compares very well with Ref. [91]. The refractive indices for the AlN and GaN layers in our Bragg reflectors must be adjusted slightly due to the strain that these layers experience. Photoreflectance measurements on our Bragg reflectors show that the bandgap of GaN is blueshifted by 100 meV. The AlN bandgap on the other hand, is necessarily redshifted by approximately the same energy (100 meV). This results in a rigid shift of ≈100 meV of the corresponding curves in Fig. 4.4. For a certain energy, the GaN layers of the Bragg reflector will have a lower refractive index with respect to the curve in Fig. 4.4 (a). The AlN layers on the other hand, will have a higher refractive index as compared to Fig. 4.4 (b). The slightly smaller contrast in refractive index, which is the consequence, has a small effect (0.3%) on the peak reflectance of the AlN/GaN Bragg reflectors. Omitting the excitonic absorption, as often can be seen in the literature, creates a significant change of the refractive indices. Figure 4.5 shows a comparison between the real refractive indices of GaN based on functions with [Eq. 4.25] and without excitonic effects [12]. As shown, the difference is not negligible. A continuous transition at the GaN bandgap can be observed for the calculation based on Eq.4.25. In

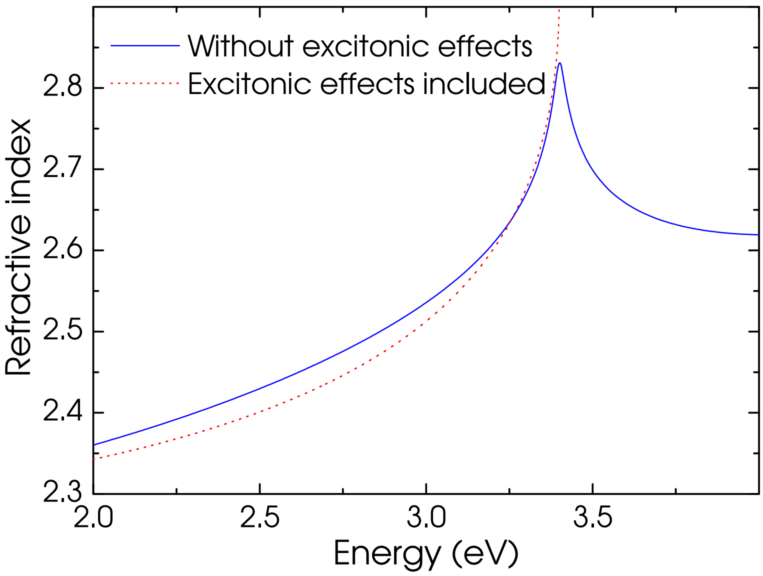

Figure 4.5: The real refractive indices based on dielectric functions with and without excitonic absorption.

contrast, the calculation where the excitonic effects have been omitted, diverges at the bandgap.

4.2 Considerations for nitride-based Bragg reflectors

In Ch. 1 and in the previous section we discussed the necessity of employing Bragg reflectors as high-reflectance components for optoelectronic devices such as VCSELs and RCLEDs. In order to obtain a high reflectance it is important to have well defined layer thicknesses, abrupt and smooth interfaces and a smooth surface. These criteria pose challenges for the growth. Furthermore, a Bragg reflector should *ideally* have the following properties: a large Δn, a small lattice mismatch between the materials for the quarter-wave layers and n- and p-conductivity. Since this work is concerned with investigating the epitaxial growth of Bragg reflectors, it must be possible to grow them *in situ*. The latter properties are discussed in the following with an emphasis on (Al,Ga,In)N based Bragg reflectors for potential optoelectronic device applications in the blue-violet wavelength range (400–450 nm).

Theoretical reflectance and bandwidth of (Al,Ga,In)N based Bragg reflectors In theory, when selecting materials for nitride based Bragg reflectors, any properly chosen combination out of the (Al,Ga,In)N materials group can be used as long as it is transparent in the desired wavelength range, which in our case is between 400 and 450 nm (3.10–2.76 eV). However, following the discussion in the previous section, it is highly desirable to have a large difference between the refractive indices of the constituent materials of the Bragg reflector. At 450 nm the largest difference Δn in refractive indices between nitrides that are still transparent, is between AlN and GaN whose refractive indices are 2.11 and 2.47 respectively. These values give a Δn of $2.11 - 2.47 = 0.36$. An example of a simulated reflectance spectrum for a high-reflectance (R$=0.997$) 20-

period AlN/GaN Bragg reflector was presented in the preceding section [Fig. 4.2]. All other combinations of transparent materials from (Al,Ga,In)N will yield a lower Δn, which for the same number of periods, results in a lower reflectance and BW. We can therefore draw the conclusion that, from an optical standpoint, AlN and GaN are the preferred candidates for the realization of nitride-based Bragg reflectors for wavelengths ranging from near-UV to blue to green.

Combinations of other materials commonly used for Bragg reflectors, such as, for example, combinations of SiO_2, ZrO_2 and HfO_2 [87, 97, 98, 109], offer a much higher difference in refractive index. However, it is not possible to grow these materials *in situ* together with (Al,Ga,In)N because O is a highly undesirable impurity that acts as a dopant in GaN. Furthermore, these materials are polycrystalline or amorphous, which drastically complicates subsequent growth of, for instance, the active region. One of the main advantages with the choice of AlN and GaN for Bragg reflectors is that the mirror structures can be grown monolithically, which allows for subsequent growth of for instance, pn-junctions and MQWs. Depending on the approach the *ex situ* processing steps can be greatly reduced or excluded completely. Of course one could shift the burden from epitaxy to processing by employing techniques such as lift-off and wafer bonding [108]. Here, essentially only the active region is grown epitaxially. This region is then freed from the substrate and any sacrificial epitaxial layers by a lift-off procedure. It should be emphasized that what is left is a thin free-standing film which includes the active region. The film is attached to a wafer by a wafer bonding procedure followed by contacting and further processing. Bottom and top dielectric Bragg reflector are applied by, for example, sputtering or bonding. The scope of this work is to explore the feasibility of epitaxial growth of VCSELs. This is why the processing approach has not been investigated. It should be pointed out that both techniques have their advantages and disadvantages. External processing might be closer to the realization of VCSELs but *in situ* methods offer a more cost-effective approach. It should also be stressed that none of the two main paths have yet resulted in an electrically driven VCSEL. It is therefore still an open question which approach is the most suitable for the purpose of realizing a VCSEL.

There are however, two major difficulties associated with the choice of AlN and GaN for DBRs. Firstly, AlN is commonly assumed to be an insulator which would prohibit obtaining vertically conducting AlN/GaN structures. Secondly, and most critically, the large lattice mismatch between GaN and AlN frequently causes crack formation.

Cracks A lattice mismatch of 2.4% between GaN and AlN often leads to crack formation due to the accumulation of tensile strain in these structures [83]. Figure 4.6(a) shows a typical cracked surface as revealed by differential interference-contrast optical microscopy. An AFM micrograph of the same sample is displayed in Fig. 4.6(b). The flow-controller responsible for regulating the N flux partially failed during the growth of this sample. This resulted in a higher-than-normal N flux which was also fluctuating. As a consequence the structure was effectively grown N rich which induced cracking. A cracked surface does not necessarily lead to a large reduction of the reflectance, but in almost all cases it does. Therefore, for purely optical purposes, a cracked sample might still be acceptable. For instance, the cracked sample depicted in Fig. 4.6 still has

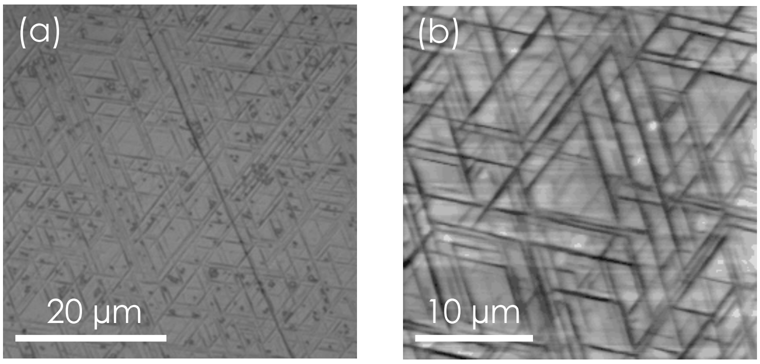

Figure 4.6: A differential interference-contrast mode optical microscope image (a) and an AFM micrograph (b) obtained from the surface of a cracked 21.5 period AlN/GaN Bragg reflector sample.

a reflectance of 0.95–0.97. Device processing for electrical purposes is essentially impossible if the sample is cracked. The cracks create voids that go through the epitaxial layer. These voids could, for instance, be filled by metal after a metalization step and they would effectively act as short circuits.

Since the cracking issue is a major obstacle for the realization of *in situ* grown VCSELs and RCLEDs it has spurred the development of a wide variety of successful approaches in order to reduce the strain in nitride based Bragg reflectors and thereby lowering the risk of crack-formation or preventing cracks to form altogether. Most of the devised techniques for lowering the strain have, however, a negative impact on the optical performance of the Bragg reflectors.

Vertical conductivity and current aperture As mentioned earlier, one of the properties of an ideal Bragg reflector for VCSEL or RCLED purposes is vertical conductance. The importance of this property is elaborated in the following with the intent of realizing a VCSEL device.
Before an electrically driven VCSEL can be achieved the problem of defining a current aperture must be overcome. The current aperture depends on the geometrical configuration of the device and its purpose is to confine the current in the active region [15]. Without a current aperture, the emission output power would be very low because of the low current density in the active region. The most common technique to create a current aperture in existing VCSEL technology, is based on selective chemical etching and selective oxidation of the constituent materials of the device. However, there are no known selective chemical etching or selective oxidation techniques applicable to (Al,Ga,In)N materials. Thus, unless vertical current injection through the Bragg reflector is achieved, one has to rely on lateral current injection techniques which require additional *ex situ* processing steps for defining a current aperture [Fig. 4.7 (a)]. One such technique could be proton implantation. In order to avoid additional processing, it is highly desirable to have the Bragg reflectors themselves conducting vertically. Using the metal-oxide mirrors described in the previous paragraph (SiO_2, ZrO_2 and HfO_2) is in this context an inadequate choice because these materials are insulating in addition to being unsuitable for *in situ* growth.

Figure 4.7 (b) shows a scheme for a VCSEL with a vertical current injection through a conducting n-type Bragg reflector grown on a conducting substrate. The white ar-

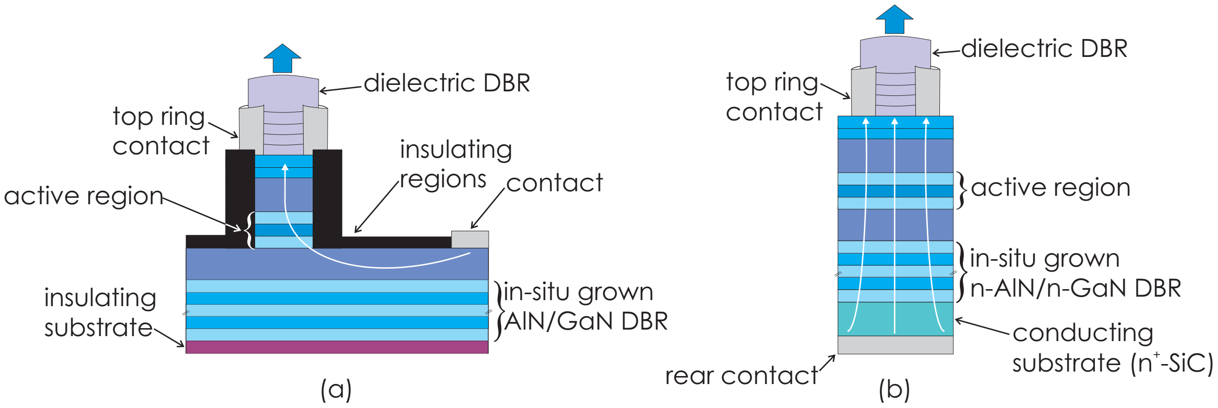

Figure 4.7: Two proposed schemes for the realization of a electrically driven VCSEL emitting in the blue/violet wavelength range. The scheme in (a) uses a non-conducting Bragg reflector and the scheme in (b) uses a conducting Bragg reflector. The white arrows schematically indicate the current flow in the structures.

rows indicate schematically the current flow in the two structures. Contacts are applied on the front-side of the structure and on the back side of the substrate. No extra processing is needed for the definition of the current aperture since the vertical geometry is inherently defining such an aperture. It should be noted that the region that includes the (In,Ga)N active layer and the GaN cavity is so thick that it will relax to an in-plane lattice constant that is close to GaN. Subsequent growth of AlN will give rise to cracks because the AlN layers will experience the full tensile strain induced by the relaxed cavity resulting in crack-formation. This is the reason for applying a dielectric Bragg reflector on the front side of the device *ex situ*.

Doping of $Al_xGa_{1-x}N$ It is commonly believed that AlN is invariably insulating by nature. A number of theoretical studies predict that it is essentially impossible to overcome the insulating properties of AlN [26, 101, 128]. According to these studies, n-type doping is inhibited by the low formation energy of Al vacancies in n-type AlN. Acting as triply charged acceptors, these vacancies compensate the Si donors, which results in a pinning of the Fermi level close to the midgap. In addition, the huge conduction band offset between GaN and AlN (2.2 eV) seems to completely hinder a carrier flow across the heterointerfaces. Nevertheless, Si-doping of low Al content $Al_xGa_{1-x}N$ has been demonstrated and has resulted in n-type layers of good conductivity [3, 47, 76, 77, 88, 104, 112, 129] and lately a small but growing number of reports concerning the doping of pure AlN has been published [47, 48, 71, 76, 78, 104, 105, 106]. Still, there are no reports about Si-doped $Al_xGa_{1-x}N$/GaN Bragg reflectors. Only a very few attempts on p-type doping of $Al_xGa_{1-x}N$ have been reported. One of the highest hole concentration values is found in Ref. [43] where Mg was used as a p-dopant and a hole concentration of 2.7×10^{17} cm^{-3} was measured for a Mg concentration of 8×10^{19} cm^{-3} and a Al content of 0.45. There are no reports on p-type doping of pure AlN.

In Chapter 5, n-type AlN/GaN Bragg reflectors will be presented.

Material comparison In the following the most common choices of materials for strain-mediating approaches will be briefly described.

$Al_xGa_{1-x}N/Al_yGa_{1-y}N$ layers A very common approach is to reduce the lattice mismatch by using ternary $Al_xGa_{1-x}N$ layers either in combination with GaN or with a second ternary layer $Al_yGa_{1-y}N$ [8, 28, 55, 74, 79, 80, 90, 95, 96, 113, 116]. The Al content composition of the ternary layers must be low enough to prevent cracking but still large enough to give a reasonable difference between the refractive indices of the two layers of the period. This compromise between low Al-content and difference in refractive index is the drawback of this method. Because of the small difference in refractive index a very large number of periods are needed to obtain a high reflectance. Figure 4.8 shows a calculation based on Eq. 4.3 of the maximum theoretical reflectance of Bragg reflector structures grown with different combinations of nitrides from the (Al,Ga,In)N group. All structures were assumed to be grown on SiC substrates. We see that the reflectance reduces as soon as any combination apart from AlN/GaN is used. As previously mentioned, the AlN/GaN combination represents the optical optimum because it possesses the largest difference in refractive index of any other combination of (Al,Ga,In)N materials that are transparent at the desired wavelength range of 400–450 nm. For example, in Ref. [96] 43 periods of $Al_{0.34}Ga_{0.66}N/GaN$ yielded a reflectance of 0.98 and a BW of only 14 nm.

Strain-balanced buffer layers Another common strain-reduction technique involves the growth of some type of strain-balanced buffer layer such as an (Al,Ga)N layer [80, 110] or a thick (~ 1 μm) AlN layer [8]. In the case of an (Al,Ga)N buffer layer the composition of Al and Ga must be adjusted so that the in-plane lattice constant of the buffer layer $a_{(Al,Ga)N}$ corresponds to the average in-plane lattice constant $\bar{a}$ of a free-standing, fully relaxed, and in itself coherent Bragg reflector structure. The value of $\bar{a}$ is calculated by minimizing the total strain energy of the Bragg reflector. Since $a_{(Al,Ga)N} = \bar{a}$ is fulfilled the structure will not experience any additional strain. This condition minimizes the risk of crack-formation. The reasoning behind employing a thick AlN layer follows a similar but somewhat simpler path. In this case cracking is avoided by providing a moderate compressive strain to the Bragg reflector since a structure under compressive strain does not relax by cracking. A thick enough AlN layer is fully relaxed and has an in-plane lattice constant $< \bar{a}$. Therefore, as desired, the AlN buffer layer exerts a compressive strain on the Bragg reflector. The advantage of using buffer layers is that the impact on the optical properties of the structures is negligible. Other related techniques based on the concept of providing compressive strain include the growth of optically asymmetric Bragg reflectors [81, 83] where the layers under tensile strain are grown much thicker than what is required by the $\lambda/4$ criterion, and AlN and $Al_xGa_{1-x}N$-insertion layers periodically inserted between the nominal $Al_xGa_{1-x}N/GaN$ layers of the Bragg reflector [23, 113]. Again, as in the case of using $Al_xGa_{1-x}N/Al_yGa_{1-y}N$ layers, these techniques have a negative effect on the reflectance and BW [Fig. 4.8].

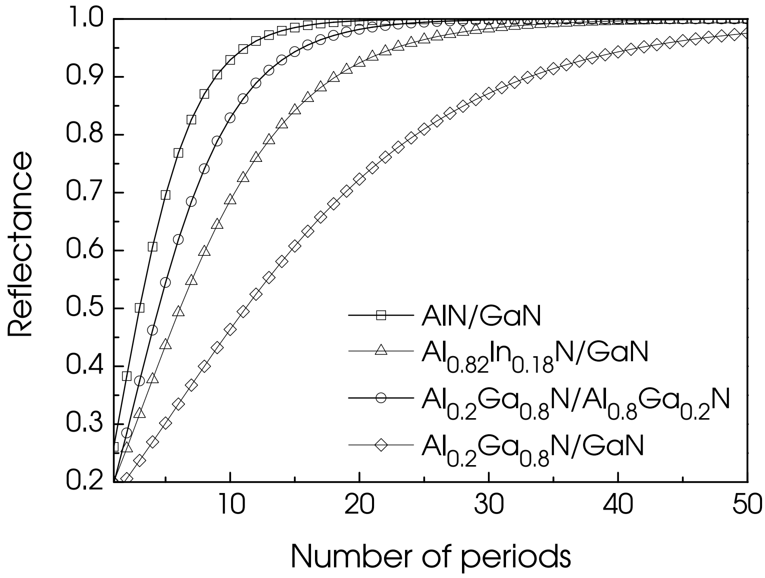

Figure 4.8: Reflectance as a function of the number of periods for a few different material combinations in the (Al,Ga,In)N group for Bragg reflectors.

Lattice matched (Al,In)N An elegant strain reduction approach is described in Ref. [13]. Here, the problem of the lattice mismatch is completely eliminated by the growth of nearly lattice matched (Al,In)N/GaN Bragg reflectors. This lattice matched growth comes at the expense of a reduction of the difference in refractive index. This is in principle not a problem since a lattice matched condition allows the growth of a very large number of periods without any accumulation of strain. The reflectance loss due to the small Δn can thus be compensated by growing a number of additional (Al,In)N/GaN periods.

Direct growth of AlN/GaN In theory, the simplest and most straightforward approach is to grow binary AlN/GaN Bragg reflector structures directly on the substrate without using any strain-mediating techniques. This approach does not have any impact on the reflectance and BW because the full Δn can be used. The optimum growth regimes of GaN and AlN are not too far away from each other which means that both materials can be grown under conditions that yield layers of a very good quality in all respects.

These attractive properties have spurred a substantial number of attempts to grow AlN/GaN Bragg reflectors [29, 82]. However, as Fig. 4.6 shows us, the large lattice mismatch of 2.4% very often leads to crack-formation. Therefore, in practice this method is one of the most difficult to employ. A major improvement of this approach is presented in Chapter 5 where we will see that by a proper choice of substrate and growth procedure the GaN layers will relax only partially. The tensile strain in the AlN layers is therefore small enough to prevent cracking. This result allows the growth of crack-free structures of a very high reflectance.

Chapter 5

AlN/GaN Bragg reflectors

In this chapter, we discuss the successful synthesis of both Si-doped and undoped AlN/GaN high-reflectance Bragg reflectors grown on 6H-SiC(0001) substrates. A reflectance of ≥ 0.99 for a 20.5 period Bragg reflector was achieved. Vertical conductivity measurements show that the doped structures are vertically conducting in contrast to the undoped structures, which are highly resistive.

The initial section treats the specific growth conditions for the AlN/GaN structures. We will see that the disparate growth conditions of AlN and GaN require special care when growing Bragg reflectors consisting of both these materials. In the subsequent sections the surface, structural, optical and electrical properties are presented.

5.1 Growth

Initial considerations In order to obtain high-reflectance Bragg reflectors, it is very important to achieve a well-defined period and abrupt and smooth interfaces between the quarter-wave layers throughout the structure. Any deviation from the quarter-wave criterion will result in a reduction of the reflectance. In addition, the surface must be smooth on, at least, the scale of the desired wavelength otherwise the reflectance at normal incidence is reduced by scattering. This also means that the surface must be free of droplets (≈ 1 μm) and cracks.

Evidently, also the employed substrate surfaces must be of a very high standard. Almost all Bragg reflectors were grown directly on 6H-SiC substrates with GaN always being the first layer. The employed 6H-SiC wafers were either hydrogen etched or polished by NovaSiC [Ch. 2]. A few structures were grown with an AlN buffer layer between the substrate and the Bragg reflector.

As shown in Ch. 3, the optimum growth regimes for GaN and AlN differ in temperature by almost 100°C. This complicates the task of choosing the best growth conditions for the growth of the AlN/GaN Bragg reflectors. For example, growing GaN under the nominal growth conditions for AlN (830°C) requires a very high Ga flux in order to counterbalance the extreme desorption rate of Ga because of the much higher growth temperature. Only a small fraction of the impinging Ga flux would actually be incorporated into GaN since most of the Ga would be wasted through desorption. On the other hand, if one chooses to grow under the nominal conditions for GaN (740°C) then the risk of Al droplet formation increases drastically because the desorption rate of Al is very low at this low temperature. Therefore, under the assumption of metal-stable or N-limited growth [Ch. 2], excess Al will accumulate on the surface. Uncontrollable Al accumulation will eventually lead to Al droplet formation.

Growth conditions The AlN/GaN Bragg reflectors were grown under metal-stable and thus N-limited conditions [Ch. 2] at 780°C, which represents a compromise between the different optimum growth regimes of GaN (740°C) and AlN (830°C). Since this temperature is higher than the nominal growth temperature for GaN, a substantially higher Ga flux was used to counter the higher Ga desorption rate due to the higher temperature. At the same time, this growth temperature is lower than the optimum one for AlN, leading to a higher probability for Al-droplet formation. Therefore, due to the high Ga flux and the low Al desorption rate, the amount of excess metal had to be closely monitored and controlled in order to prevent droplet formation. This was achieved by introducing growth interruptions [Ch. 2]. Each GaN layer was followed by a 5–10 s growth interruption which was increased to 30 s after an AlN layer. Once the surface became free of excess metal, an abrupt low-to-high intensity transition of the RHEED pattern could be observed. As was shown in Ch. 2, the time between the closing of the Al or Ga shutters until the low-to-high RHEED intensity transition defines the recovery time, which indicates the required time to rid the surface of excess metal. The growth interruption must be adjusted such that it is longer than the recovery time else there will not be enough time to clear the surface from excess metal. However, the growth interruption must not be too long to prevent the surface from being roughened.

Like during nominal growth of AlN and GaN both desorption and growth is simultaneously taking place through the recovery time since the N flux is kept uninterrupted throughout the growth. It is important to recognize this fact else the growth rate Γ will be overestimated once the layer thicknesses have been determined.

A combination of x-ray, reflectometry and SEM was used to determine the AlN and GaN layer thicknesses with an accuracy of ± 0.5 nm. This will be treated in more detail in the following sections. The thickness determination is important because the layer thicknesses are used to calibrate Γ and, further, they serve as input-parameters for reflectance simulations. An over- or underestimation of Γ results in layers that are too thin or too thick, respectively. This has the consequence that the stopband shifts away from the desired position. For example, if the AlN layer has a thickness of 52.8 nm after opening the Al shutter for 437 s followed by a recovery time of 20 s the effective growth rate is $\Gamma_e = 52.8/(437 + 20)$ nm/s $= 0.116$ nm/s $\Leftrightarrow$ 418 nm/h. Excluding the recovery time yields $\Gamma = 0.121$ nm/s $\Leftrightarrow$ 435 nm/h which is 4% higher than Γ_e.

It should be noted that the 30 s growth interruption that followed the AlN layers was not long enough to produce a $(2\sqrt{3} \times 2\sqrt{3})$R30° reconstruction [Ch. 3]. Much longer growth interruptions are needed, between 3 and 4 minutes, to develop this reconstruction. During the growth itself a streaky RHEED pattern was observed indicating a smooth surface.

The Si concentration used in the Bragg reflectors was 4×10^{19}–1.5×10^{20} cm^{-3} and was adjusted by varying the effusion cell temperature. The Si concentrations were confirmed by SIMS.

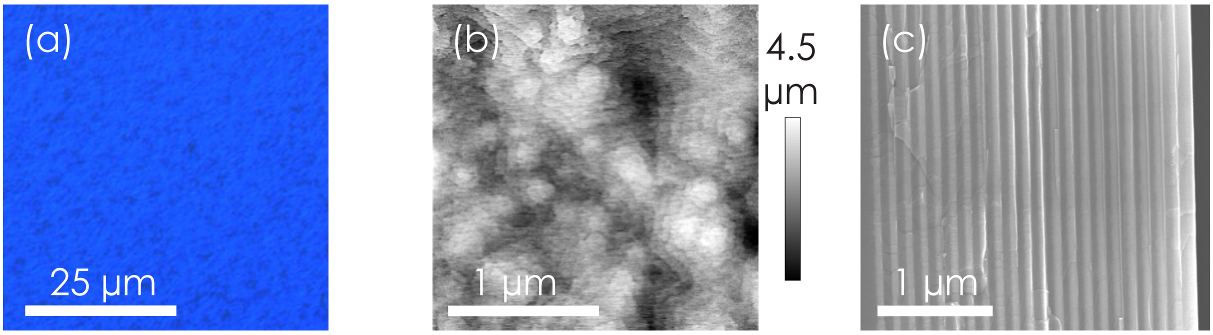

Figure 5.1: (Differential interference-contrast mode optical microscope image of a Si-doped 21.5 period AlN/GaN Bragg reflector (a). AFM micrograph of the surface of a 21.5 period undoped Bragg reflector (b). SEM micrograph of a cross-section (side view) of a 21.5 period sample (c).

5.2 Surface and interface properties

An optical microscope fitted with a CCD-camera and operating in differential interference-contrast mode together with AFM operating in contact mode and SEM were used to investigate the surface morphology and to determine the presence of cracks and droplets.

Figure 5.1 (a) shows an example of a crack-free surface of a Si-doped 21.5 period AlN/GaN Bragg reflector as obtained by differential interference-contrast optical microscopy. This picture should be compared with Fig. 4.6(a) in Ch. 4 which shows the surface of a cracked sample. An AFM micrograph of a crack-free surface of an undoped 21.5 period Bragg reflector taken over a 2×2 μm^2 area is shown in Fig. 5.1(b). A very smooth surface morphology with clearly resolved monolayer steps can be observed. Figure 5.1(c) shows an SEM image of a cross-section (sideview) of an undoped 21.5 period Bragg reflector. The leftmost (bottom) layer constitutes the SiC/GaN boundary and the rightmost layer (top surface) is the GaN/air interface. We see that the alternating GaN (bright) and AlN (dark) layers exhibit abrupt and smooth interfaces throughout the more than 2 μm thick structure. No cracks can be observed.

Figure 5.2 show cross-sectional TEM micrographs obtained from a 21.5 period Bragg reflector. The TEM was operated in two-beam bright-field mode with the diffraction vector $\mathbf{g} = 0002$ [Figs. 5.2 (a–c)] and $\mathbf{g} = 11\bar{2}0$ [Fig. 5.2 (d)], respectively. To achieve the $\mathbf{g}_{0002}$ imaging condition, the sample is tilted in such a way that the (0002) planes fulfill the Bragg condition and, thus the interfaces are parallel to the incident electron beam (end-on projection). The contrast in Figs. 5.2 (a–c) appears chemically sensitive and it is therefore possible to determine the chemical abruptness of the interfaces. The complete structure, which is more than 2 μm thick, is shown in Fig. 5.2(a). The GaN/SiC interface is located in the upper right corner and the growth propagates from this interface in the direction that is perpendicular to it. We see that the interfaces are abrupt and smooth throughout the entire structure. The contrast reduction observed in the left part of Fig. 5.2(a) is due to the wedge like shape of the TEM samples with thinner regions closer to the surface. A magnification of the first 5 periods closest to the SiC substrate is shown in Fig. 5.2(b). It is evident that the interfaces are abrupt, smooth, homogeneous and parallel to each other. The only rough interface that can be found is between the SiC substrate and the first GaN layer. This roughness is expected because the Bragg reflector was grown on an as-received SiC substrate [Ch. 2]. It is clear however that this initial rough surface does not have an impact on the growth beyond the first GaN layer because, as we can see, already the first GaN/AlN interface is perfectly smooth. Furthermore, the TEM analysis reflects the microstructure, i.e. the character, the distribution and the density of the threading dislocations. In general, in order to observe threading dislocations the condition $\mathbf{g} \cdot \mathbf{b} \neq 0$ must be fulfilled, where **b** is the Burgers vector. The Burgers vector is $\langle 0001 \rangle$ for pure screw dislocations and $\frac{1}{3}\langle 11\bar{2}0 \rangle$ for edge dislocations. Therefore, screw dislocations are observed under $\mathbf{g} = 0002$ [Fig. 5.2 (c)] and edge dislocations are in contrast to $\mathbf{g} = 11\bar{2}0$. Consequently, we observe a much larger number of edge dislocations than screw dislocations, which is typical for MBE grown nitrides.

A triple-axis high-resolution x-ray diffractometer with a Si(022) analyzer crystal was used to determine the period of the Bragg reflectors. This method is more accurate than SEM and much less time-consuming than TEM.

Figure 5.3 shows an ω-2θ XRD scan of a 21.5 period Bragg reflector. We observe a large number of well resolved satellites. The envelope associated to GaN is visible to the left of the SiC(0006) peak. The corresponding envelope for the AlN is located to the right of the SiC(0006) peak. We can determine the period P according to the following formula

$$\mathrm{P} = \frac{\lambda_{\mathrm{CuK}\alpha_1}}{2\Delta\theta \cos\theta_{\mathrm{B}}} \tag{5.1}$$

where the $\lambda_{\mathrm{CuK}\alpha 1}$ is the wavelength of the x-rays (0.1540562 nm) and where θ_{B} is the Bragg angle for GaN (17.2860°). The following conditions apply for the growth rates since the Bragg reflectors are grown under N-limited conditions [Ch. 2]

$$\Gamma_{\mathrm{GaN}} = \Gamma_{\mathrm{AlN}} = \Gamma_{\mathrm{N}} \tag{5.2}$$

where Γ_{GaN} and Γ_{AlN} are the growth rates for GaN and AlN, respectively and where Γ_{N} is the growth rate as determined by the N-flux. Combining Eqs. 5.1 and 5.2 gives the thickness of the GaN layers as

$$\mathrm{d}_{\mathrm{GaN}} = \frac{\mathrm{t}_{\mathrm{GaN}}}{\mathrm{t}_{\mathrm{GaN}} + \mathrm{t}_{\mathrm{AlN}}}\mathrm{P} \tag{5.3}$$

where t_{GaN} and t_{AlN} are the growth times for the GaN and AlN layers. Finally, the thickness of the AlN layers is given by

$$\mathrm{d}_{\mathrm{AlN}} = \mathrm{P} - \mathrm{d}_{\mathrm{GaN}}. \tag{5.4}$$

The accuracy of the thickness determination is within ± 0.5 nm and compares well with SEM, TEM and optical measurements.

From the previous chapter we understand the importance of accurately controlling the layer thicknesses. The ω-2θ XRD scans together with Eqs. 5.1 through 5.4 provides the necessary feedback tool that is required for adjusting the growth rates from one growth run to another. In addition the obtained thicknesses are used as input parameters for reflectance simulations which will be discussed in the next section.

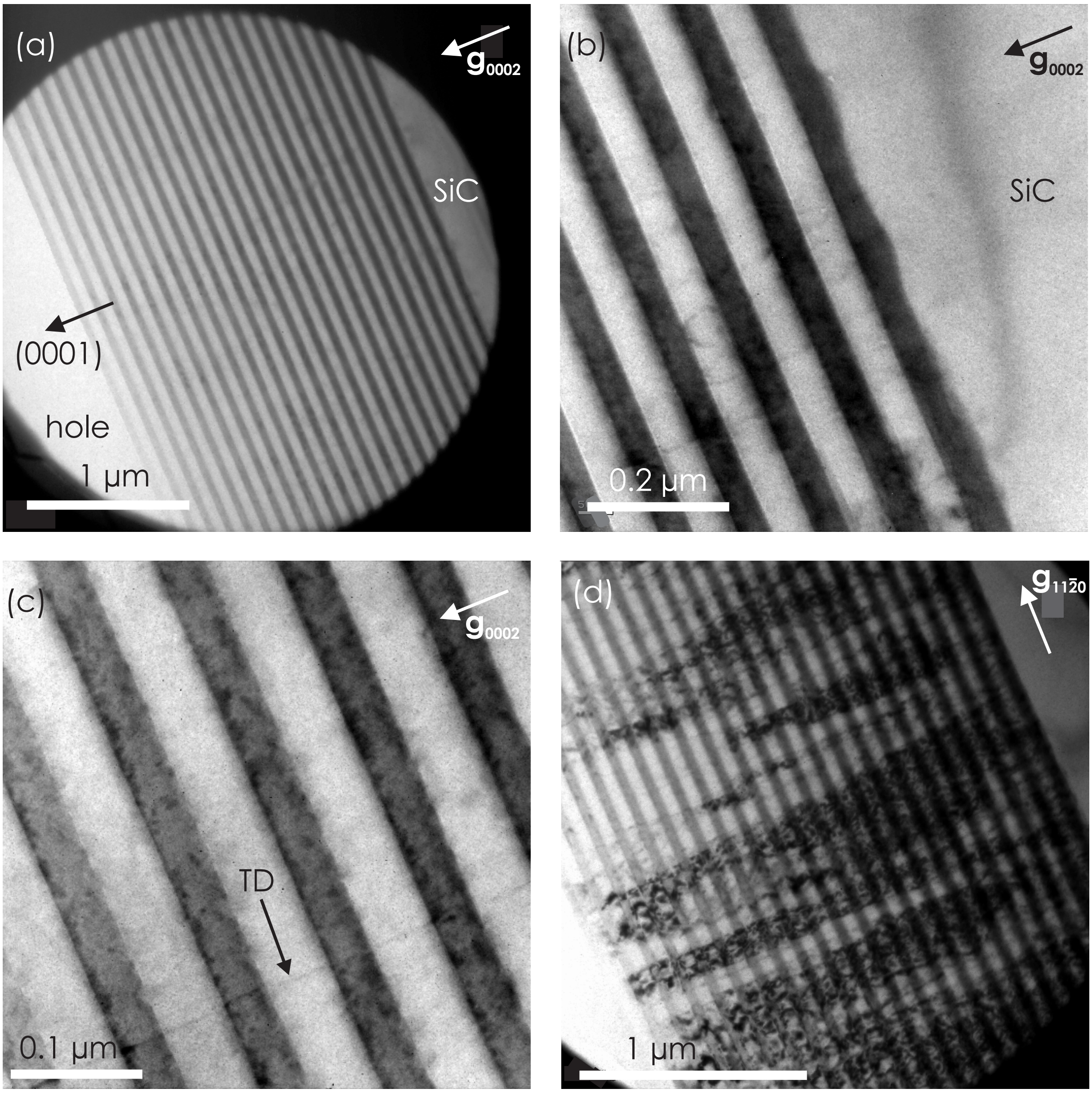

Figure 5.2: TEM micrograph of a 21.5 period Bragg reflector (a). The TEM was optimized for chemical composition. The SiC/GaN interface is to the right. The growth direction is (0001). Magnification of the 5 periods closest to the SiC substrate (b). Screw threading dislocation (TD) (c). A large number of edge dislocations (d).

5.3 Strain and structural properties

Raman spectroscopy was performed in order to clarify the reason for the absence of cracks in the Bragg reflectors. The measurements were done in the backscattering configuration using a He-Ne laser emitting at 632.8 nm.

Raman spectra from thick ($\approx 1\ \mu$m) GaN and AlN layers grown on SiC were compared to Raman spectra from both doped and undoped Bragg reflectors [Fig. 5.4]. We observe that the measured positions of the E_2 phonon peaks for the thick GaN and AlN layers are 566.3 cm^{-1} and 662.2 cm^{-1}, respectively. These values are in good agreement with values found in the literature and are consistent with the GaN layer being under

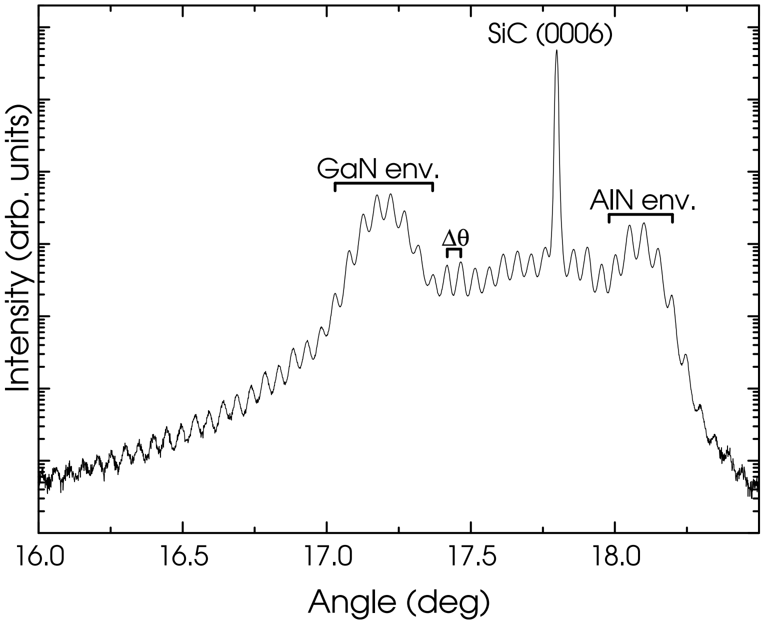

Figure 5.3: An $\omega - 2\theta$ XRD scan of a 21.5 period Bragg reflector. The envelopes related to the individual GaN and AlN peaks are positioned to the left and right of the SiC(0006) peak, respectively. $\Delta\theta$ denotes the angular separation between two satellites.

a slight tensile and the AlN layer being under a slight compressive strain [30, 31, 115]. However, we see that in the case of the Bragg reflectors, both doped and undoped, the position of the E_2 phonon peak of the GaN layer shifts to a higher wavenumber with $+20.5$ cm^{-1} reflecting a strong compressive strain of $-1.3\%\pm0.2\%$ [31, 115]. The position of the E_2 phonon peak of AlN, on the other hand, shifts towards a lower wavenumber with -23.0 cm^{-1} and is corresponding to an equally strong tensile strain ($+1.3\%\pm0.2\%$). [30, 31]. Since the GaN and AlN layers experience opposite strain of virtually equal magnitude, the structure approaches a strain-compensated state with a negligible residual net stress. This drastically lowers the risk of crack-formation. A thin ($\leq$ 50 nm) GaN layer grown on a 6H-SiC substrate experiences a compressive strain and does not fully relax. A subsequently grown thin AlN layer will therefore not experience the full tensile strain imposed by the underlying GaN layer. The smaller tensile strain greatly reduces the risk of crack formation in the AlN layer which does not relax. This effect repeats itself for every period in our structures and is ultimately the cause for achieving crack-free AlN/GaN Bragg reflectors.

It should be emphasized that the choice of growing the structures on 6H-SiC substrates was essential. Growing GaN on sapphire substrates induces a strong compressive strain on the GaN epitaxial layers because of the much larger lattice mismatch (16%). The most common approach to reduce the dislocation density arising from this large lattice mismatch is to grow a thick ($\approx$ 1 μm) GaN buffer layer before proceeding with the growth. A thick GaN layer is fully relaxed. Any AlN layer grown on the GaN buffer layer will therefore experience the full lattice mismatch between GaN and AlN. Of course this dramatically increases the risk of creating cracks in the AlN film. The same problem arises when GaN pseudo-substrates or templates are used.

A direct and accurate way to measure the in-plane and out-of-plane strain is to perform x-ray diffraction reciprocal space mapping (RSM). Figure 5.5 shows a RSM of

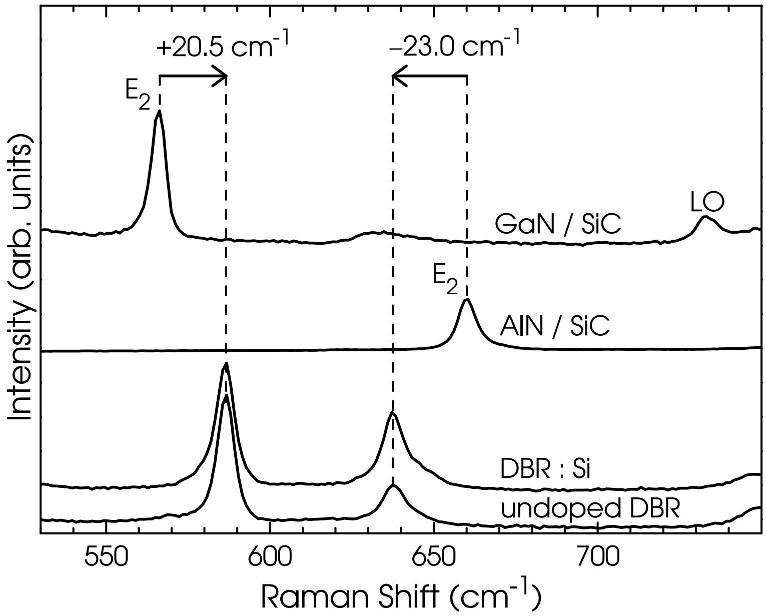

Figure 5.4: Raman spectra of a thick GaN (top) and a thick AlN (center) film and a doped (second from bottom) and an undoped DBR structure (bottom).

a 21.5 period Bragg reflector. The contour plot shows, from the top of the figure to the bottom, the AlN envelope, the SiC peak and the GaN envelope. The area between the AlN and GaN envelopes is related to the satellites. In a RSM a shift in the horizontal direction corresponds to a shift in the in-plane lattice constant a. On the other hand, a shift in the vertical direction corresponds to a shift of the out-of-plane lattice constant c. We observe that both the GaN and the AlN envelopes are on the same horizontal position (black dashed line in Fig. 5.5) in the RSM. This means that the Bragg reflector has relaxed to a strain-compensated state with an average in-plane lattice constant as expected from the Raman measurements.

It should be emphasized that the RSM unambiguously shows us that after the relaxation of the first GaN layer the following layers grow coherently. There is no gradual relaxation process taking place after the first GaN layer.

5.4 Optical properties

We employed a combination of reflectometry and ellipsometry to assess the reflectance of our structures. Reflectometry which in our case is performed by a commercially available setup, gives the correct position of the stopband and the correct BW. It is very difficult, however, to obtain an absolute value of the reflectance with this method because of its arduous calibration. For instance, the reference (Si wafer) must be of the same thickness as the sample. The sample has to be completely free of In which is used for mounting [Ch. 2] else it will not reflect at normal incidence. Further, the etching of In in HCl must be done very carefully not to deposit remnants of the In from the back side of the sample onto the surface. In addition, the reflectometer exhibits a non-linear behavior close to the cutoff wavelength of 400 nm. Therefore, without an independent and thorough calibration, the accuracy of the reflectance values is not better than ±5%.

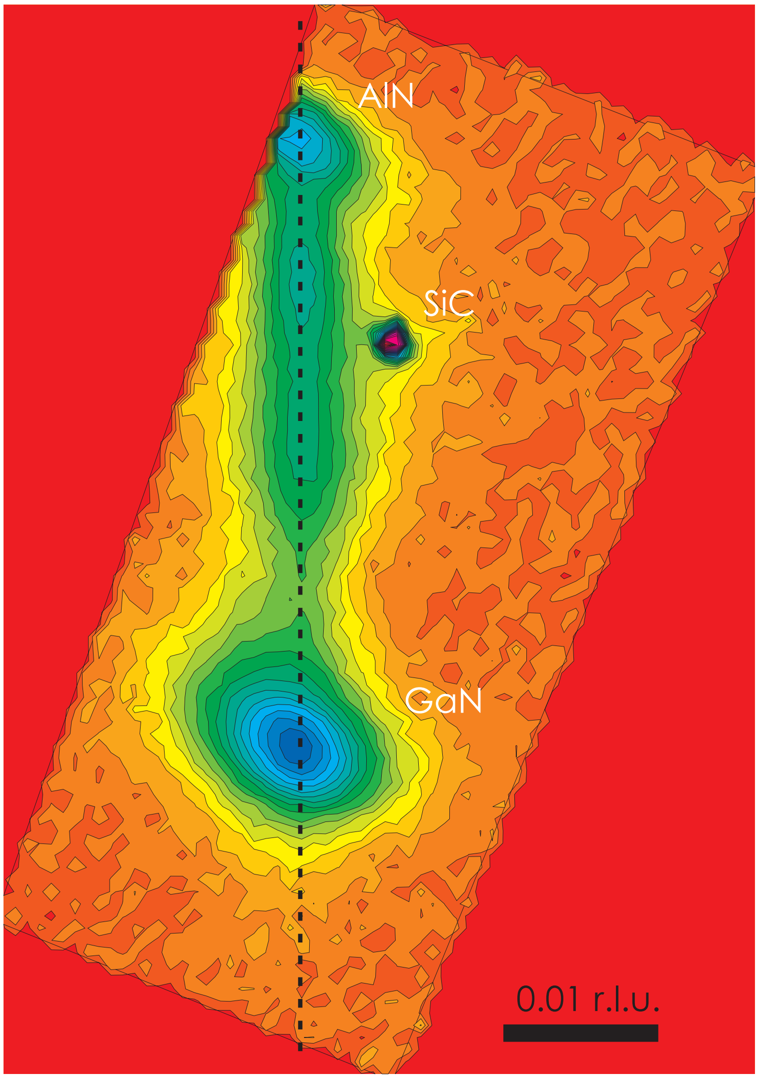

Figure 5.5: Reciprocal space map of a 21.5 period Bragg reflector. The black dashed line is a guide to the eye and indicates the horizontal position for the AlN and GaN envelopes and for the satellites.

Ellipsometry, on the other hand, is an absolute measurement method that gives the real and imaginary parts of the complex refractive index of a material. However, because it is impossible to perform ellipsometry at normal incidence, we can only calculate an apparent reflectance $\tilde{R}$ for normal incidence. Using Eq. 4.24 from Ch. 4 to calculate $\tilde{R}$

$$\tilde{R} = \frac{(n-1)^2 + k^2}{(n+1)^2 + k^2} \tag{5.5}$$

where n and k are the optical constants, will yield an apparent reflectance that is lower than the true reflectance due to the oblique incidence. An additional consequence is that the reflectance peak spectral position is shifted with respect to the true reflectance peak position.

Figure 5.6 (a) shows the reflectance spectrum of a 21.5 period Bragg reflector with a reflectance maximum of 0.99±0.05 at 453 nm and with a bandwidth of 40 nm as ob-

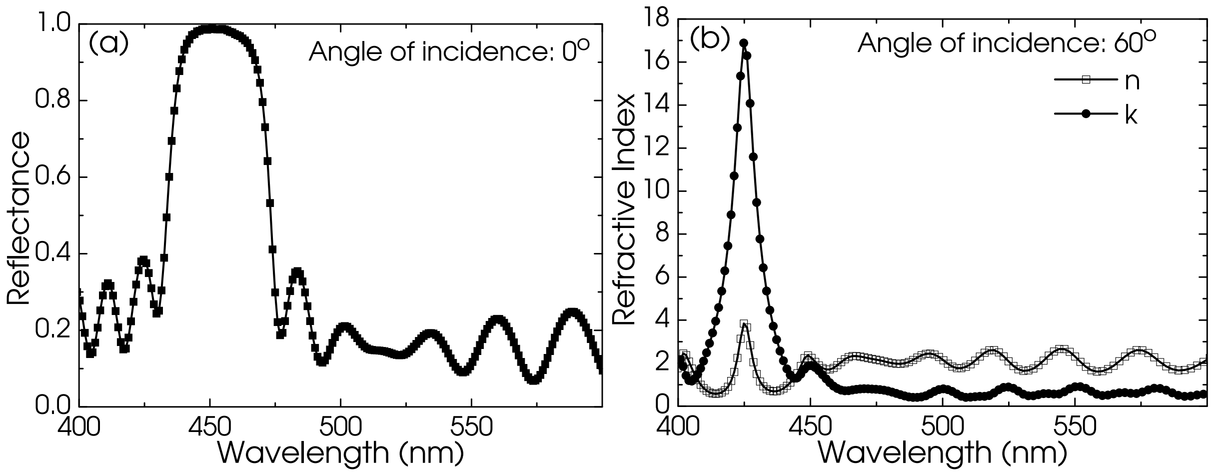

Figure 5.6: Reflectance spectrum of a 21.5 period Bragg reflector. The maximum reflectance is 0.99 at 453 nm with a bandwidth of 40 nm (a). The real and imaginary parts of the complex pseudo refractive index of the same Bragg reflector as determined by ellipsometry (b).

tained by a reflectometer. Figure 5.6(b) shows the optical constants of the same structure as shown in 5.6 (a) as obtained by an ellipsometer. It should be emphasized that these optical constants are the parts of a complex *pseudo* refractive index which is defined by the Bragg reflector structure as a whole. They are not the optical constants (*n* and *k*) of the individual AlN and GaN layers. The apparent reflectance spectrum based on the ellipsometry measurements is shown in Fig. 5.7. As expected from the discussion above, we observe that the stopband is shifted and that the maximum reflectance is lower as compared to the reflectance spectrum obtained by a reflectometer since the ellipsometry measurements were performed at an incidence angle of 60°.

In the following is presented how reflectometry and ellipsometry can be combined to yield accurate reflectance measurements.

Variable angle spectroscopic ellipsometry (VASE) was performed for a wide range of incidence angles. A fit is applied for each of the measurements. The fit relies on an accurate knowledge of the layer thicknesses which are obtained by XRD and a model for the surface and interface roughness. Finally a simultaneous fit of all the individual spectra is made and gives the best model for simulating the reflectance at normal incidence. In this final fit, only the model surface and interface roughness is varied. The thicknesses are assumed to be known and therefore kept constant. Figures 5.8 (a) and (b) show the VASE measurements and the corresponding individual fits for the Bragg reflector of Fig. 5.6 (a) and (b) for an incidence angle of 25° and 55°, respectively. The resulting model gives a reflectance spectrum at normal incidence that compares remarkably well with the reflectance spectrum obtained by the reflectometer. The accuracy of the reflectance is now within ±1% evidencing a well calibrated reflectometer.

The reflectance spectra of three undoped 21.5 period Bragg reflectors designed for two different wavelength ranges (450 nm and 550 nm) are shown in Fig. 5.10 (a). The structures have maximum reflectances of 0.99 (▽), 0.99 (▲) and 0.98 (□) at 454 nm, 457 nm and 561 nm, respectively. The BW is ≈40 nm for all structures except for the structure with the stopband at 561 nm (□) which has a BW of 46 nm. In Fig. 5.10 (b) the reflectance spectra of the two undoped Bragg reflectors having their stopbands at

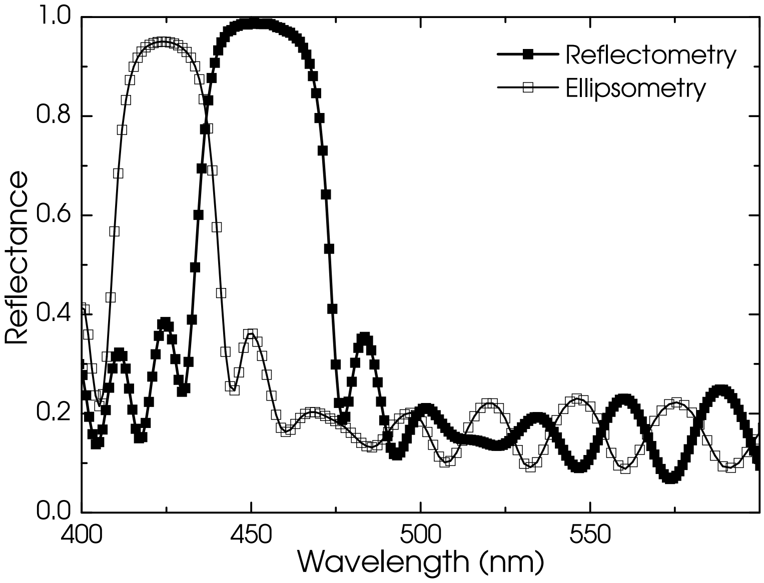

Figure 5.7: Comparison of the reflectance spectrum obtained by a reflectometry and the apparent reflectance spectrum acquired by ellipsometry. The stopband is shifted and the maximum reflectance is reduced in the apparent reflectance spectrum of the ellipsometry.

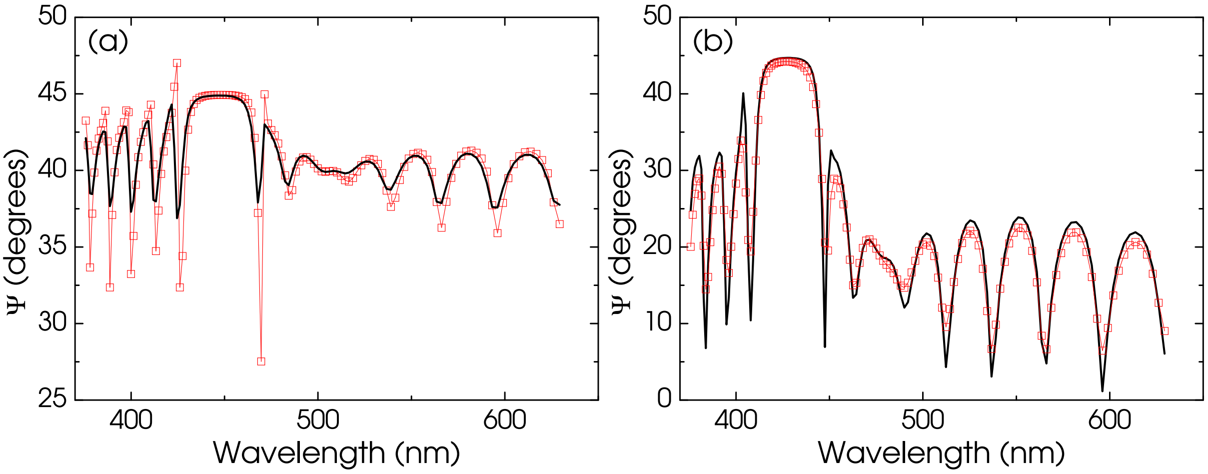

Figure 5.8: VASE measurements (squares) with the applied fits (lines) for incidence angles of 25° (a) and 55° (b), respectively.

454 nm (▽) and 457 nm (▲) are compared with the reflectance spectrum obtained from a Si-doped sample (■) which has a maximum reflectance of 0.99 at 444 nm with a BW of 41 nm. Thus, we can make the important observation that the Si-doping does not degrade the reflectance, at least for the range of Si-concentrations used here (4×10^{19}–1.4×10^{20} cm^{-3}).

The variation of the stopband position around the desired wavelength of, in this case, 450 nm is caused by slightly different AlN and GaN layer thicknesses in the different samples. These thickness variations which are very difficult to control, are the result of the fluctuation of the growth parameters from one growth run to another. For instance different substrate holders have slightly different thermal profiles. The amount of In used during the mounting and the substrate size are further examples of factors that have an impact on the thermal profile. Slightly colder or warmer growth conditions influence the incorporation and desorption of the incoming metals. This elucidates the importance of having a large stopband BW that can accommodate for small changes of the stopband position. The reflectance at 450 nm for the Bragg reflector with its stopband at 457 nm (▲) [Fig. 5.10 (a)] is 0.98 instead of 0.99. This reduction can be considered to be negligible for RCLED applications. It is still too large though for a VCSEL.

5.5 Electrical properties

Photo-lithography and Ar/Cl_2 reactive ion etching (RIE) were used to define mesa structures of different diameters (70, 230 and 450 μm) on the sample as a preparation for the electrical measurements. Rear and front contacts were applied by electron beam evaporation of Ni/Cr followed by deposition of Au for a total contact thickness of 165 nm. The contacts were alloyed at 750°C for 5 minutes.

Figure 5.11 shows the vertical I-V characteristics of a Bragg reflector with a Si concentration of 4×10^{19} cm^{-3}. The measurement was done at room temperature using two different contact diameters, each corresponding to one of the curves in Fig. 5.11. We see that the sample exhibits an ohmic behavior in the entire measurement range. In contrast, undoped Bragg reflectors exhibit a resistance which is at least four orders of magnitude higher than that of the doped Bragg reflectors. The resistance of this measurement setup is mainly determined by the tip- contact- and spreading resistance and it is therefore not possible to obtain the resistance of the structure itself.

Etching experiments were conducted for the purpose of determining the specific resistance of the Bragg reflector. Here, 100 nm of the epitaxial layer was etched away in successive steps and after each step the vertical resistance was measured. These experiments revealed that the vertical resistance depends linearly with the depth and we could also determine the specific series resistance R_0A. A structure having a Si

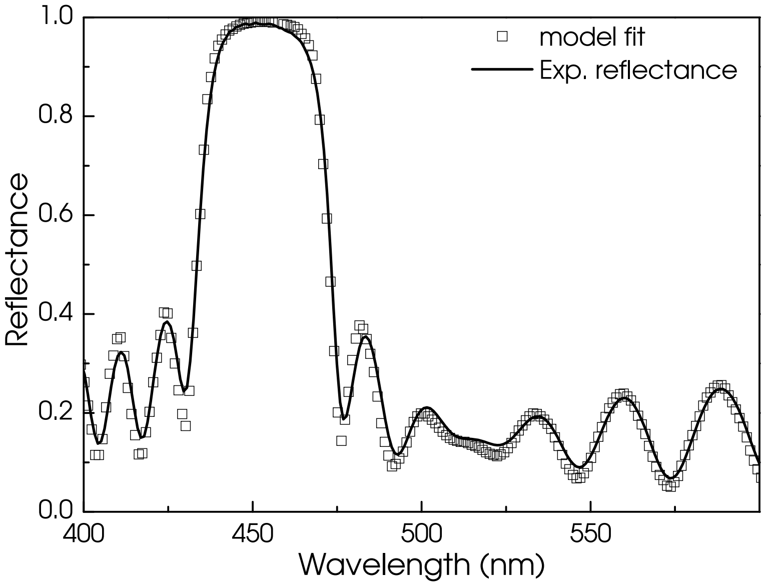

Figure 5.9: Reflectance spectrum of a 21.5 period Bragg reflector and the corresponding fit based on a model obtained from VASE measurements.

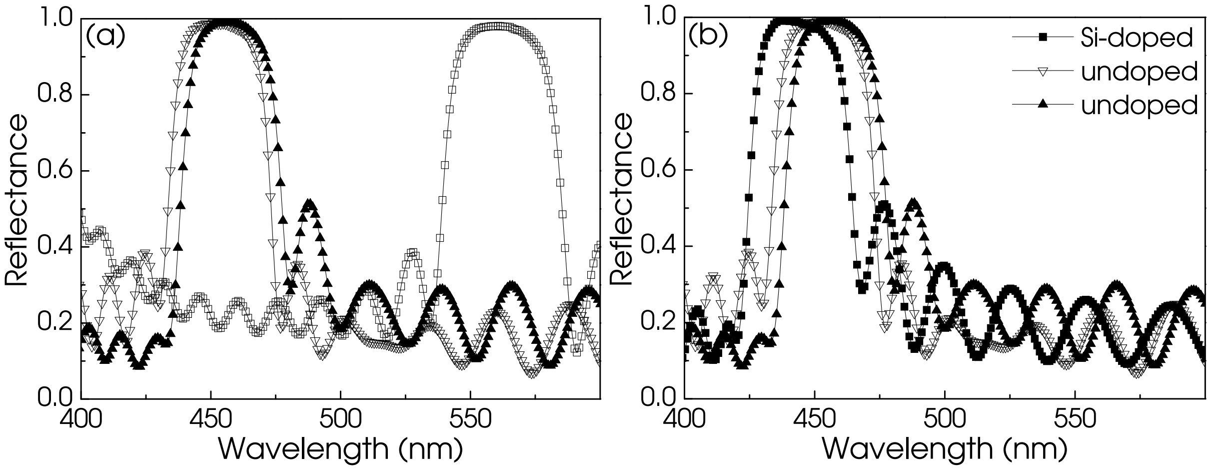

Figure 5.10: Reflectance spectra of three undoped Bragg reflectors (a). Reflectance spectrum of a Si-doped Bragg reflector (■) as compared to the reflectance spectra of two undoped structures (b).

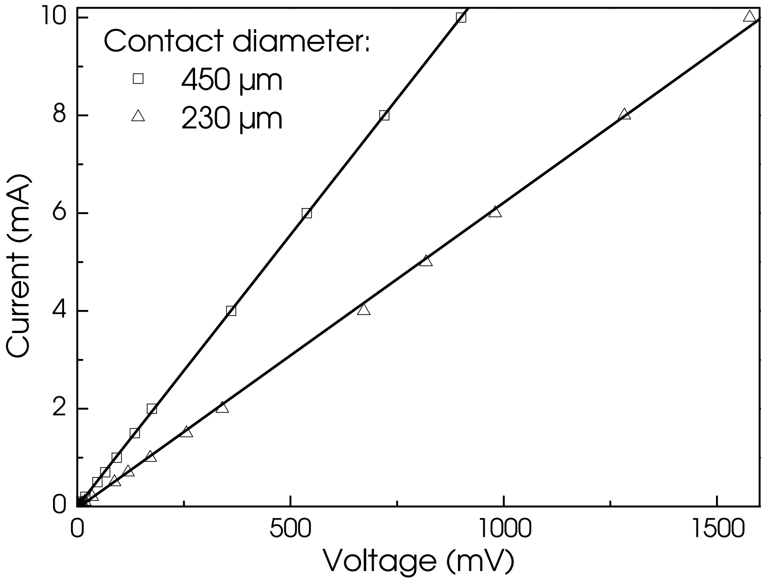

Figure 5.11: Room temperature I-V characteristics of a Si-doped Bragg reflector for two contact diameters. The Si concentration is $4 \times 10^{19}\text{cm}^{-3}$.

concentration of 4×10^{19} cm^{-3} yields a specific resistance of 4×10^{-3} Ωcm^2. A doping concentration of 1.4×10^{20} cm^{-3} gives a specific resistance of 2×10^{-3} Ωcm^2. The resistance of the doped Bragg reflectors measured at 77 K is only a factor of two larger than that measured at room temperature (RT) indicating that no significant carrier freeze-out occurs. Thus, these structures exhibit a metallic-like behavior. This metallic-like conductivity rises concerns about the possible presence of highly conducting paths in the doped Bragg reflectors. These paths might consist of screw dislocations since a large number of reports correlate leakage currents in GaN with screw dislocations [40, 41, 70, 93, 99]. In one of the reports, Ref. [70] also mixed dislocations are shown to be conducting. It should be noted, however, that the absence of such highly conducting paths in the undoped Bragg reflectors would be difficult to understand. None of the reports show a connection between edge dislocations and leakage paths. This is interesting because the density of edge dislocations in GaN is 1–2 orders of magnitude larger than the density of screw dislocations.

A combination of dynamic-contact electrostatic force microscopy (DC-EFM) [38], conductive AFM (C-AFM) and AFM was used to investigate the presence of conducting paths in our Si-doped Bragg reflectors. The DC-EFM setup, which does not require a conducting path between tip and sample, is sensitive to surface potential fluctuations or to surface charge density variations. The setup also gives a simultaneous AFM scan of the same area. This is very useful since it allows for a correlation between possible electrical features with surface morphology. Figure 5.12 (a) shows a DC-EFM map over a 10×10 μm^2 area of Bragg reflector with a Si-concentration of Si-concentration 4×10^{19} cm^{-3}. In this particular instrument configuration, the potential variations associated with conducting paths should be visible as well defined high-contrast white regions. No potential fluctuations can be observed within the lateral resolution ($\approx$70 nm) of the instrument. The map only reflects the measurement noise. The few small areas of higher contrast (black) can be attributed to surface contamination since their position coincides with that of the bright spots seen in Fig. 5.12 (b) which shows the simultaneously recorded AFM micrograph. The results from the DC-EFM measurements are an indication that no conducting paths are present in the Bragg reflectors. Furthermore, our x-ray results from the Bragg reflectors show that the density of screw dislocations [102] is less than 10^9 cm^{-2} which translates to an average distance of at least 0.3 μm between two screw dislocations. This distance is well within the resolution of the DC-EFM. However, C-AFM provides an even higher resolution and therefore, C-AFM was performed on our samples in order to obtain an independent and a conclusive measurement.

Figure 5.13 (a) shows a C-AFM micrograph over a 2×2 μm^2 area of the Bragg reflector shown in Fig. 5.12. The image is heavily distorted by external interference (50 Hz wall-plug AC 230 V) visible as the wavy pattern in Fig. 5.13 (a). The image was therefore filtered to eliminate all artificial high-frequency components. The result of this filtering procedure is shown in Fig. 5.13 (b). Note that the elongated horizontal black lines are an artifact from the filtering procedure. One observes that from the bottom and up, the image is gradually becoming brighter until a dark area again is encountered close to the top of the picture as indicated by the black arrow in Fig.5.13 (b). This gradual increase in brightness is the result of intentionally changing the bias between the conducting AFM tip and the sample surface. For a certain bias the current becomes large enough to destroy the AFM tip. This happened at the point which is indicated by the black arrow in Fig. 5.13 (b). Therefore, the area between the arrow and the top edge of Fig. 5.13 (b) represents no reliable measurements. The increase of the bias facilitates the detection of leakage paths occurring as high-contrast regions (spots) and result in in an inhomogeneous (random) brightness distribution in the C-AFM micrograph. We see no such randomly distributed spots. Instead, areas of homogeneous brightness are observed. This means that each spot of the sample scanned by the conducting AFM tip has basically the same conducting properties. Based on these C-AFM scans, we can therefore unequivocally state that no leakage paths are present in the Bragg reflector.

Selfconsistent Schrödinger-Poisson simulations of the Bragg reflector band profile were performed in order to gain a better understanding of the conduction mechanism. We used a freeware software package [94] to solve the Schrödinger and Poisson equations in the effective mass approximation. The polarization charges at the AlN/GaN

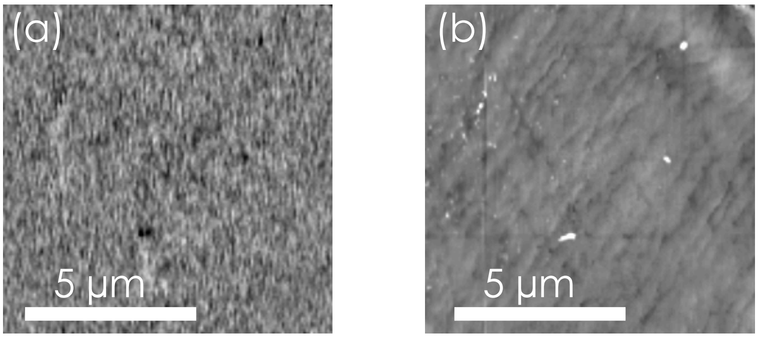

Figure 5.12: DC-EFM map over a 10×10 μm^2 area of a Bragg reflector with a Si-concentration of 4×10^{19} cm^{-3} (a). The map only reflects the measurement noise. The few small areas of higher contrast (black) can be attributed to surface contamination since their position coincides with that of the bright spots seen in the simultaneously recorded AFM micrograph (b).

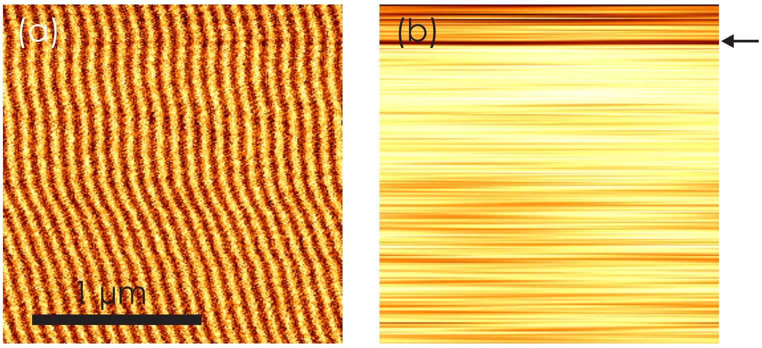

Figure 5.13: Conductive AFM micrograph of the Si-doped Bragg reflector shown in Fig. 5.12 (Si-concentration = 4×10^{19} cm^{-3}). In (a) an unfiltered image is shown. The arrow indicates where C-AFM tip was destroyed by the large applied bias. Therefore, the area between the arrow and the top edge of the image does not represent any reliable measurements.

interfaces were simulated by introducing 1 Å thick doping spikes at the interfaces with a sheet doping concentration of $n_S = 5 \times 10^{13}$ cm^{-2}. The AlN and GaN layer thicknesses were set to 44 and 58 nm, respectively. The electron effective mass is assumed to be 0.2 [92, 103] in the GaN and 0.3 in the AlN [72]. We set the Si concentration to 1.5×10^{20}cm^{-3} which is equal to the highest doping concentration used in the Bragg reflectors. All simulations were done for RT. Figure 5.14 shows the conduction band (CB) profile for a single AlN/GaN period as yielded by the selfconsistent Schrödinger-Poisson simulations. We observe that, except for very thin regions at the AlN/GaN interfaces, the polarization fields are screened (flat CB). More important, we see that the GaN layers are degenerate and the AlN CB minimum is very close (within the width of the Fermi-Dirac distribution at room temperature) to the Fermi level E_F. This leads to the important result that the AlN barriers at the interfaces are very thin (2–3 nm), which therefore allows for appreciable tunneling. However, if we assume a Si concentration of 4×10^{19}cm^{-3} corresponding to the lowest doping concentration used in the Bragg reflectors, the AlN barriers become too wide for tunneling to occur.

This apparent discrepancy is resolved by considering that an important physical mechanism is not included in the Schrödinger-Poisson simulation, namely, the auto-ionization of the Si donors due to the electric field [7, 62]. The simulation only includes thermal ionization and thus underestimates the electron concentration, particularly in

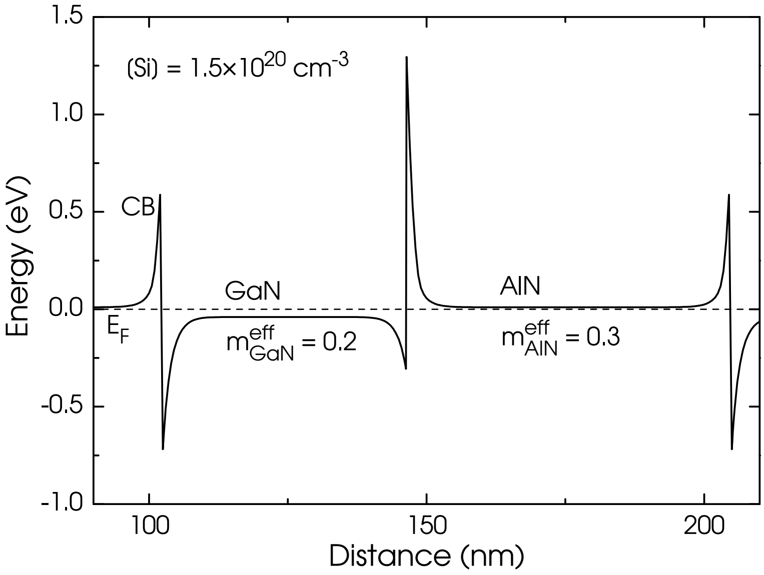

Figure 5.14: Conduction band profile for one period of AlN/GaN according to self-consistent Schrödinger-Poisson simulations. Note that the polarization charges at the AlN/GaN interfaces are effectively screened.

the AlN layers. By calculating the slope of the CB (due to the electric field) in the 58 nm thick AlN layers and with the knowledge of the Si donor level in AlN, the spatial distance from the Si donor level to the CB at the same energy can be calculated. Assuming a Si donor level at 60 meV yields a distance of 0.6 nm. A donor level of 180 meV gives a distance of 1.7 nm. These two values of the Si donor level represent the two extremes for the Si-donor level in AlN as determined in Ch. 3. A distance of 0.6–1.7 nm allows for a complete ionization of the Si donors through tunneling. The conclusion is that in the Bragg reflector structures the carrier concentration in the AlN layers approximately equals the Si donor concentration. The auto-ionization effect will essentially prevail even at low temperatures since the tunneling processes do not explicitly depend on temperature. This explains the metallic behavior observed in our Bragg reflectors.

A more specific calculation on how the tunneling rate R from the ground state of a hydrogenic impurity depends on the electrostatic field E is given in Ref. [7] and reads as follows.

$$R(E) = \omega \left(\frac{\alpha}{E}\right)^{2n^\star - 1} e^{-\frac{\alpha}{E}} \tag{5.6}$$

where α is given by

$$\alpha = \frac{2}{3} \frac{\hbar^2}{me(n^\star a)^3} \tag{5.7}$$

and where ω is defined as

$$\omega = \frac{me^4}{\hbar^3 \kappa^2 (4\pi\epsilon_0)^2} \frac{(6)^{2n^\star - 1}}{2(n^\star)^2 \left[\Gamma(n+1)\right]^2} \tag{5.8}$$

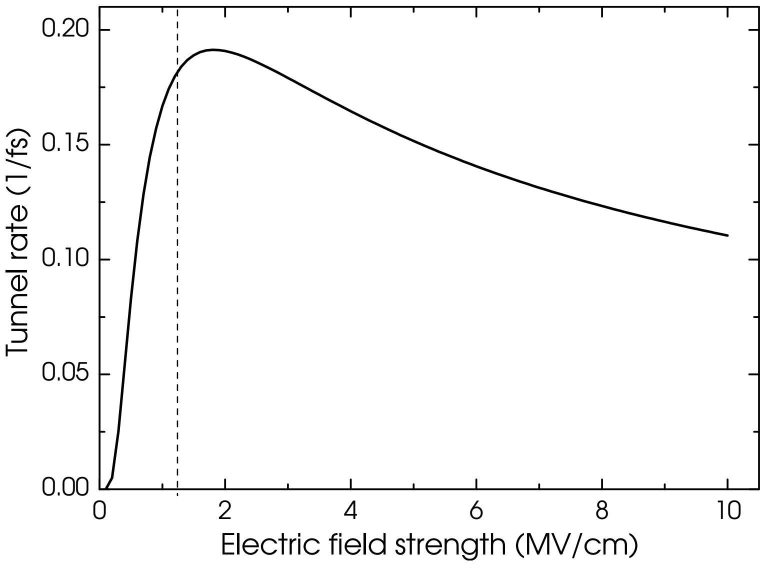

Figure 5.15: Tunneling rate as a function of the internal electrostatic field for a hydrogenic impurity in AlN. The dashed line indicates the internal electrostatic field (1.2 MV/cm) present in the AlN layers in the Bragg reflectors.

in which κ is the dielectric constant, m the mean effective mass, $n^\star$ the effective principal quantum number and a the Bohr radius according to $a = \hbar 4\pi\kappa\epsilon_0/me^2$.

The derivation of these results is quite complex and is discussed in detail in Ref. [123].

Figure 5.15 shows the tunneling rate as a function of the internal electrostatic field for a hydrogenic impurity in AlN. The dashed line indicates the internal electrostatic field (1.2 MV/cm) present in the AlN layers in the Bragg reflectors. We see that the dashed line is close to the maximum of the tunneling rate which is as large as 0.2/fs corresponding to a tunneling time of 5 fs. From these results we can conclude that auto-ionization is a very efficient process.

Chapter 6

(Al,In)N/GaN Bragg reflectors

Here, we discuss the synthesis of $Al_{0.82}In_{0.18}N/GaN$ Bragg reflectors grown on 6H-SiC(0001) substrates. The $Al_{0.82}In_{0.18}N$ layers are lattice matched to GaN and, thus, crack-formation should not be observed in these Bragg reflectors. The growth conditions for the structures are based on the results from the last Section of Ch. 3 which treats the growth of (Al,In)N layers.

The initial Section treats the specific growth conditions for the $Al_{0.82}In_{0.18}N/GaN$ Bragg reflectors and the following Sections show the impact of these growth conditions on the surface and interface properties and and the structural and optical properties.

6.1 Growth conditions

The lattice matched $Al_{0.82}In_{0.18}N$ layers of the Bragg reflectors were grown at 400°C with a N-flux of 1 sccm [shaded region in Fig. 3.17 in Ch. 3] yielding N-rich growth conditions with a growth rate of $\Gamma_{(Al,In)N} = 200$ nm/h. The Al and In shutters were closed and the growth temperature was ramped to 650°C prior to the growth of the GaN layers. The N-flux was kept at 1 sccm which in this case gave Ga-stable growth conditions with a growth rate of $\Gamma_{GaN} = 400$ nm/h. At the end of the GaN layers the growth temperature was again ramped down to 400°C before the start of next $Al_{0.82}In_{0.18}N$ layer.

A RHEED pattern indicating shallow ($< 5°$) facets on the growth front, was observed during the growth of the $Al_{0.82}In_{0.18}N$ layers. The facet related RHEED pattern disappeared during the growth of the GaN layers indicating a smoothening of the surface. The surface was exposed to the plasma during the temperature ramping which took 5–6 minutes in each direction (400 → 650°C and 650 → 400°C) but this did not degrade the RHEED pattern.

6.2 Surface and interface properties and structural properties

Figure 6.1 (a) shows a DIC optical microscopy image of the surface of a 11 period $Al_{0.82}In_{0.18}/GaN$ Bragg reflector (sample M8514). No cracks can be observed. In Fig. 6.1 an AFM micrograph over a $1{\times}1$ μm^2 area of the same sample is shown. The

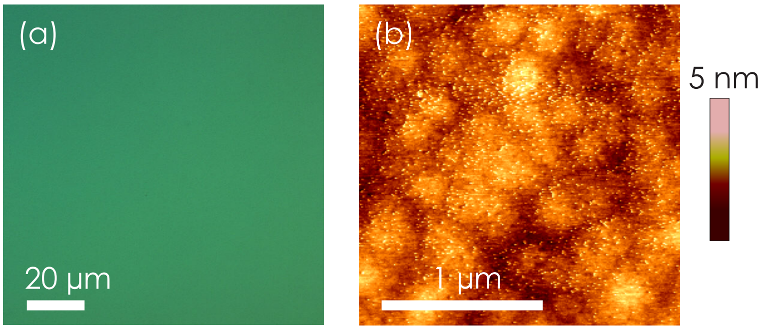

Figure 6.1: DIC optical microscopy images of the surface of sample M8514 consisting of 11 periods of $Al_{0.82}In_{0.18}N/GaN$ (a). No cracks are observed. AFM micrograph of the surface of sample M8514 (b). The small bright dots interspersed over the surface are the individual columns. Peak-to-valley and RMS roughnesses are 5.2 and 0.53 nm, respectively.

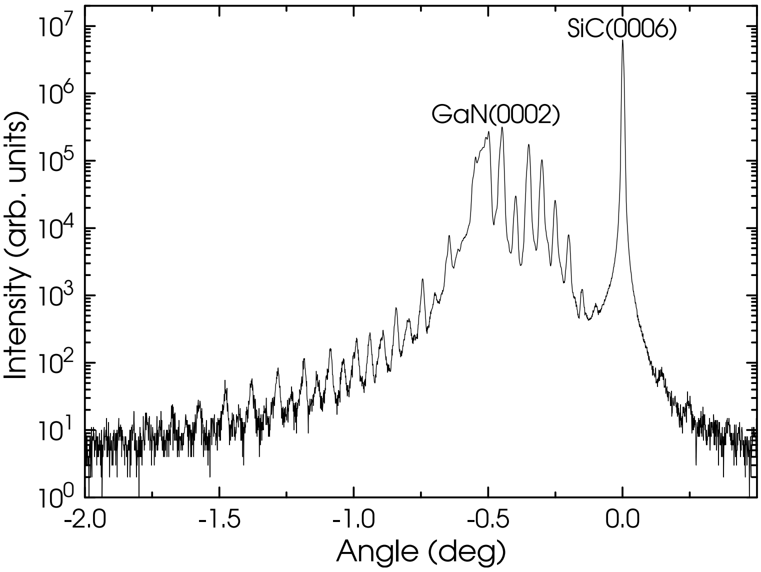

Figure 6.2: XRD ω-2θ XRD scan for the GaN(0002) reflection of sample M8514. A large number of clearly resolved satellites are observed indicating a well defined periodicity and abrupt interfaces.

small bright dots interspersed over the surface are the individual columns. The P-V and the RMS roughness are 5.2 and 0.53 nm, respectively. These values are independent of the scan-size and evidence a statistically smooth surface that is fully acceptable for optical applications.

An ω-2θ XRD scan for the GaN(0002) reflection of sample M8514, is shown in Fig. 6.2. A large number of clearly resolved satellites are observed indicating a well defined periodicity and abrupt interfaces. Using the angular separation of the satellites [Ch. 5] we can determine the period to be 94 nm.

Homogeneous and abrupt interfaces are evidenced in Fig. 6.3 which shows a cross-sectional TEM bright-field micrograph of a 6 period $Al_{0.82}In_{0.18}N/GaN$ Bragg reflector.

From the results in this Section we can conclude that the smooth surfaces and the homogeneous and abrupt interfaces are fully sufficient for the growth of lattice matched and crack-free $Al_{0.82}In_{0.18}N/GaN$ Bragg reflectors.

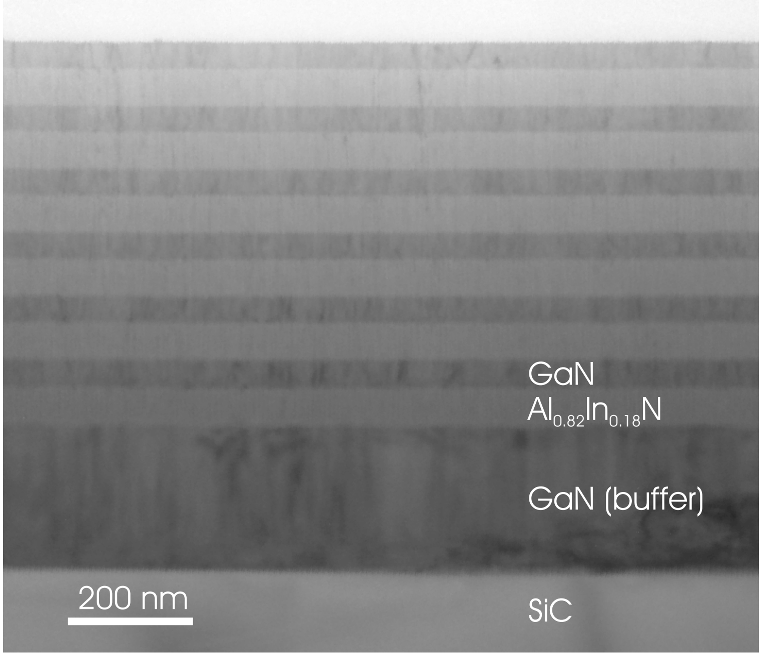

Figure 6.3: Cross-sectional TEM bright-field micrograph of a 6 period $Al_{0.82}In_{0.18}N$/GaN Bragg reflector.

6.3 Optical properties

The reflectance spectrum of a 20 period $Al_{0.82}In_{0.18}N$/GaN Bragg reflector is shown in Fig. 6.4. We see that the peak reflectance occurs at 457 nm, which is very close to the desired 450 nm, but the reflectance is only 0.42. This very low reflectance value is a disappointing surprise. A peak reflectance of at least 0.7 was expected for this structure. All $Al_{0.82}In_{0.18}N$/GaN Bragg reflectors exhibit peak reflectances that are far below the expected reflectances.

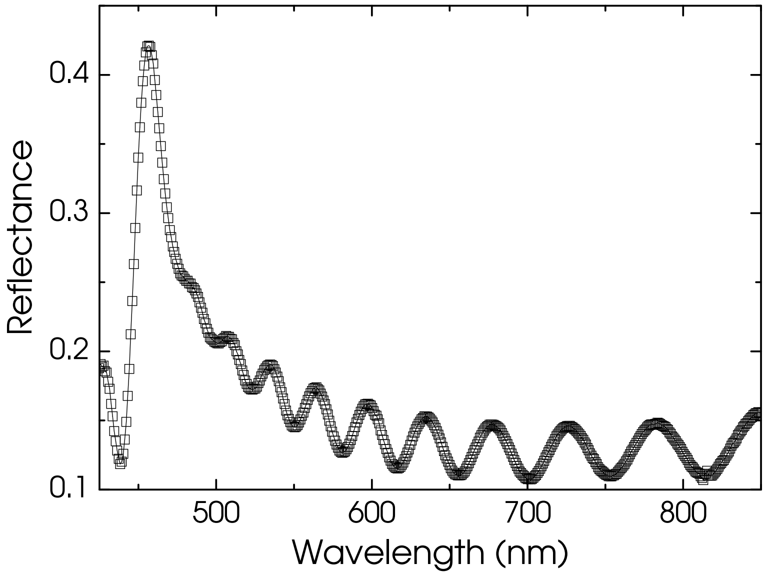

Figure 6.4: Reflectance spectra of a 20 period $Al_{0.82}In_{0.18}N$/GaN Bragg reflector.

From the previous Section we see that rough interfaces or a rough surface cannot be responsible for the low reflectances. Thus, another mechanism must be the cause.

Residual absorption or scattering could produce the observed results. A way to measure the absorption is through transmission measurements. However, this is not trivial in the case of our samples because of two reasons. Firstly, the structures were grown on n-doped SiC which absorbs already in the visible range. The doping is often very inhomogeneous leading to very different transmission results depending on the position on the sample. Secondly, the SiC substrates are polished on the top side only. This means that considerable scattering takes place at the back side of the substrate. Transmission measurements performed on (Al,In)N samples, will therefore be inconclusive.

Chapter 7

Conclusion and outlook

Conclusions This work shows that high-reflectance and crack-free AlN/GaN Bragg reflectors can be grown on 6H-SiC(0001) by plasma-assisted molecular beam epitaxy. In addition, it has been shown that Si-doping of these structures renders them vertically conducting.

This successful finding depended strongly on the growth optimization of AlN which was discussed in Ch. 3. From this Chapter we concluded that the crystal quality and the surface morphology of both un-doped and Si-doped AlN layers are comparable to the GaN layers grown in the same system. Further, we saw that Si-doping of AlN yielded semi-conducting n-type AlN.

The AlN/GaN Bragg reflectors are crack-free due to a relaxation process that results in strain-compensated structures. Key to this relaxation process is that the first layer always was GaN and that it was thin enough (45.5 nm) to relax only partially. The Bragg reflectors exhibit smooth surfaces and interfaces of very high integrity. This is evidenced by the excellent reflectance properties ($\geq$99%). Auto-ionization caused by the electric fields completely ionized the Si-donors in Si-doped AlN/GaN Bragg reflectors resulting in vertically conducting structures ($R_0 A = 2 - 4 \times 10^{-3}\ \Omega\text{cm}^2$).

In this work it was also shown that it is questionable if plasma-assisted molecular beam epitaxy is the optimum growth method for synthesizing (Al,In)N/GaN Bragg reflectors. It was shown in Ch. 3 that for growth at a temperature of 450°C and above, phase separation occurred. Growth at 300°C, on the other hand, produced homogeneous (Al,In)N films. However, these low temperature grown samples exhibited massive cracking due to tensile stresses induced by crystallite coalescence and grain boundary formation. Increasing the growth temperature to 400°C yielded homogeneous and crack-free films with smooth surfaces. Indeed, when employing the growth conditions obtained from the (Al,In)N growth optimization for the growth of (Al,In)N/GaN Bragg reflectors, crack-free structures with a smooth surface morphology and abrupt interfaces were achieved. However, all the (Al,In)N/GaN Bragg reflectors exhibit a much lower reflectance than expected. This is probably due to residual absorption or scattering effects.

Outlook The finding that crack-free Bragg reflectors consisting of AlN and GaN can be fabricated despite the large strain accumulation due to the lattice mismatch, is somewhat surprising. Even more surprising is the fact that vertically conducting structures were obtained despite the common previous opinion that AlN is electrically indifferent to doping. These results strongly inspires to grow a full-blown structure consisting of a bottom AlN/GaN Bragg reflector followed by the active region and the microcavity and finally a top dielectric Bragg reflector which is deposited *ex situ*. A ring contact on the top side of the structure and a metal alloy deposited on the back side of the conducting SiC substrate would allow for electrical injection. This would clear the path for fully epitaxially grown microcavities and electrically driven nitride-based VCSELs. In principle, even the top mirror could be an AlN/GaN Bragg reflector if the microcavity is made of AlN. In fact, such a structure was grown and exhibited a cavity resonance at the desired wavelength of 428 nm with a Q-factor of 222.

Bibliography

[1] C. Adelmann, J. Brault, D. Jalabert, P. Gentile, H. Mariette, Guido Mula, and B. Daudin. *J. Appl. Phys.*, 91(12):9638–9645, 2002.

[2] Christoph Adelmann, Julien Brault, Guido Mula, Bruno Daudin, Liverios Lymperakis, and Jörg Neugebauer. *Phys. Rev. B*, 67(16):165419, 2003.

[3] V. Adivarahan, G. Simin, G. Tamulaitis, R. Srinivasan, J. Yang, M. Asif Khan, M. S. Shur, and R. Gaska. *Appl. Phys. Lett.*, 79:1903, 2001.

[4] I. Akasaki, T. Kozowa, K. Hiramatsu, N. Sawaki, K. Ikeda, and Y. Ishii. *J. Luminescence*, 40/41:121, 1988.

[5] H. Amano, N. Sawaki, I. Akasaki, and Y. Toyoda. *Appl. Phys. Lett.*, 48(5):353–355, 1986.

[6] H. Amano, M. Kito, K. Hiramatsu, and I. Akasaki. *Jpn. J. Appl. Phys.*, 28:L2112, 1989.

[7] Jayanth R. Banavar, Darryl D. Coon, and Jr. Gustav E. Derkits. *Appl. Phys. Lett.*, 34(1):94–96, 1979.

[8] A. Bhattacharyya, Sandeep Iyer, E. Iliopoulos, A. V. Sampath, J. Cabalu, T. D. Moustakas, and I. Friel. *J. Vac. Sci. Tech. B*, 20:1229, 2002.

[9] M. Born and E. Wolf. *Principles of optics*. Pergamon Press, London, 1959.

[10] S. T. Bradley, S. H. Goss, L. J. Brillson, J. Hwang, and W. J. Schaff. *J. Vac. Sci. Tech. B*, 21(6):2558–2563, 2003.

[11] O. Brandt, R. Muralidharan, P. Waltereit, A. Thamm, A. Trampert, H. von Kiedrowski, and K. H. Ploog. *Appl. Phys. Lett.*, 75(25):4019–4021, 1999.

[12] D. Brunner, H. Angerer, E. Bustarret, F. Freudenberg, R. Höpler, R. Dimitrov, O. Ambacher, and M. Stutzmann. *J. Appl. Phys.*, 82:5090, 1997.

[13] J.-F. Carlin and M. Ilegems. *Appl. Phys. Lett.*, 83:668, 2003.

[14] J.-F. Carlin, J. Dorsaz, E. Feltin, R. Butté, N. Grandjean, M. Ilegems, and M. Laügt. *Appl. Phys. Lett.*, 86(3):031107, 2005.

[15] Connie J. Chang-Hasnain, J. P. Harbison, Ghulam Hasnain, Ann C. Von Lehmen, L. T. Florez, and N. G. Stoffel. *IEEE J. Quantum Electron.*, 27:1402, 1991.

[16] D. S. Chemla. *Helv. Phys. Acta*, 56:607, 1983.

[17] R. Chierchia, T. Bottcher, H. Heinke, S. Einfeldt, S. Figge, and D. Hommel. *J. Appl. Phys.*, 93(11):8918–8925, 2003.

[18] I. Daruka and J. Tersoff. *Phys. Rev. Lett.*, 95(7):076102, 2005.

[19] V. Yu. Davydov, V. V. Emtsev, I. N. Goncharuk, A. N. Smirnov, V. D. Petrikov, V. V. Mamutin, V. A. Vekshin, S. V. Ivanov, M. B. Smirnov, and T. Inushima. *Appl. Phys. Lett.*, 75(21):3297–3299, 1999.

[20] V.Yu. Davydov, A.A. Klochikhin, V.V. Emtsev, S.V. Ivanov, V.V. Vekshin, F. Bechstedt, J. Furthmüller, H. Harima, A.V. Mudryi, A. Hashimoto, A. Yamamoto, J. Aderhold, J. Graul, and E.E. Haller. *Phys. Status Solidi B*, 230:R4–R6, 2002.

[21] V.Yu. Davydov, A.A. Klochikhin, R.P. Seisyan, V.V. Emtsev, S.V. Ivanov, F. Bechstedt, J. Furthmüller, H. Harima, A.V. Mudryi, J. Aderhold, O. Semchinova, and J. Graul. *Phys. Status Solidi B*, 229:R1–R3, 2002.

[22] Chris G. Van de Walle and Jörg Neugebauer. *J. Appl. Phys.*, 95(8):3851–3879, 2004.

[23] M. Diagne, Y. He, H. Zhou, E. Makarona, A. V. Nurmikko, J. Han, K. E. Waldrip, J. J. Figiel, T. Takeuchi, and M. Krames. *Appl. Phys. Lett.*, 79:3720, 2001.

[24] J. Dorsaz, J.-F. Carlin, S. Gradecak, and M. Ilegems. *J. Appl. Phys.*, 97(8):084505, 2005.

[25] R. J. Elliott. *Phys. Rev.*, 108:1384, 1957.

[26] Antonella Fara, Fabio Bernardini, and Vincenzo Fiorentini. *J. Appl. Phys.*, 85:2001, 1999.

[27] R. S. Qhalid Fareed, R. Jain, R. Gaska, M. S. Shur, J. Wu, W. Walukiewicz, and M. Asif Khan. *Appl. Phys. Lett.*, 84(11):1892–1894, 2004.

[28] S. Fernández, F. B. Naranjo, F. Calle, M. A. Sánchez-García, E. Calleja, P. Vennegues, A. Trampert, and K. H. Ploog. *Appl. Phys. Lett.*, 79:2136, 2001.

[29] I. J. Fritz and T. J. Drummond. *Electron Lett.*, 68:31, 1995.

[30] J. Gleize, M. A. Renucci, J. Frandona, E. Bellet-Amalric, and B. Daudin. *J. Appl. Phys.*, 93:2065, 2003.

[31] A. R. Goñi, H. Siegle, K. Syassen, C. Thomsen, and J.-M. Wagner. *Phys. Rev. B*, 64:035205, 2001.

[32] R. N. Hall, G. E. Fenner, J. D. Kingsley, T. J. Soltys, and R. O. Carlson. *Phys. Rev. Lett.*, 9(9):366–368, 1962.

[33] O. S. Heavens. *Optical properties of thin solid films*. Dover, New York, 1991.

[34] H. Heinke, V. Kirchner, S. Einfeldt, and D. Hommel. *Appl. Phys. Lett.*, 77(14): 2145–2147, 2000.

[35] M. Hermann, F. Furtmayr, A. Bergmaier, G. Dollinger, M. Stutzmann, and M. Eickhoff. *Appl. Phys. Lett.*, 86(19):192108, 2005.

[36] B. Heying, R. Averbeck, L. F. Chen, E. Haus, H. Riechert, and J. S. Speck. *J. Appl. Phys.*, 88(4):1855–1860, 2000.

[37] Masataka Higashiwaki and Toshiaki Matsui. *Jpn. J. Appl. Phys.*, 41(2(5B)):L540–L542, 2002.

[38] J. W. Hong, Sang-il Park, and Z. G. Khim. *Rev. Sci. Instrum.*, 70(3):1735, 1999.

[39] I hsiu Ho and G. B. Stringfellow. *Appl. Phys. Lett.*, 69(18):2701–2703, 1996.

[40] J. W. P. Hsu, M. J. Manfra, S. N. G. Chu, C. H. Chen, L. N. Pfeiffer, and R. J. Molnar. *Appl. Phys. Lett.*, 78(25):3980–3982, 2001.

[41] J. W. P. Hsu, M. J. Manfra, R. J. Molnar, B. Heying, and J. S. Speck. *Appl. Phys. Lett.*, 81:79, 2002.

[42] T. Inushima, V. V. Mamutin, V. A. Vekshin, S. V. Ivanov, T. Sakon, M. Motokawa, and S. Ohoya. *J. Cryst. Growth*, 227:481–485, 2001.

[43] S.-R. Jeon, Z. Ren, G. Cui, J. Su, M. Gherasimova, J. Hana, H.-K. Cho, and L. Zhou. *Appl. Phys. Lett.*, 86:082107, 2005.

[44] V. M. Kaganer, O. Brandt, A. Trampert, and K. H. Ploog. *Phys. Rev. B*, 72(4): 045423, 2005.

[45] Yasunori Kai, Masashi Yoshimura, Yusuke Mori, and Takatomo Sasaki. *Jpn. J. Appl. Phys.*, 42(2(3A)):L229–L231, 2003.

[46] Makoto Kasu and Naoki Kobayashi. *Appl. Phys. Lett.*, 78(13):1835–1837, 2001.

[47] Makoto Kasu and Naoki Kobayashi. *Appl. Phys. Lett.*, 79:3642, 2001.

[48] Makoto Kasu and Naoki Kobayashi. *J. Cryst. Growth*, 221(1-4):739–742, 2000.

[49] Alexey Kavokin and Bernard Gil. *Appl. Phys. Lett.*, 72(22):2880–2881, 1998.

[50] S. W. King, C. Ronning, R. F. Davis, R. S. Busby, and R. J. Nemanich. *J. Appl. Phys.*, 84(11):6042–6048, 1998.

[51] Sean W. King, Robert J. Nemanich, and Robert F. Davis. *J. of The Electrochemical Soc.*, 146(7):2648–2651, 1999.

[52] G. Koblmueller, R. Averbeck, L. Geelhaar, H. Riechert, W. Hösler, and P. Pongratz. *J. Appl. Phys.*, 93(12):9591–9596, 2003.

[53] G. Koblmüller, J. Brown, R. Averbeck, H. Riechert, P. Pongratz, and J. S. Speck. *Appl. Phys. Lett.*, 86(4):041908, 2005.

[54] Fumio Koyama, Susumu Kinoshita, and Kenichi Iga. *Appl. Phys. Lett.*, 55(3):221–222, 1989.

[55] R. Langer, A. Barski, J. Simon, N. T. Pelekanos, O. Konovalov, R. André, and Le Si Dang. *Appl. Phys. Lett.*, 74:3610, 1999.

[56] C. D. Lee, Y. Dong, R. M. Feenstra, J. E. Northrup, and J. Neugebauer. *Phys. Rev. B*, 68(20):205317, 2003.

[57] J. Li, K. B. Nam, J. Y. Lin, and H. X. Jiang. *Appl. Phys. Lett.*, 79(20):3245–3247, 2001.

[58] B.-T. Liou, S.-H. Yen, and Y.-K. Kuo. *Appl. Phys. A*, 81:651–655, August 2005.

[59] Hai Lu, William J. Schaff, Jeonghyun Hwang, Hong Wu, Wesley Yeo, Amit Pharkya, and Lester F. Eastman. *Appl. Phys. Lett.*, 77(16):2548–2550, 2000.

[60] Hai Lu, William J. Schaff, Jeonghyun Hwang, Hong Wu, Goutam Koley, and Lester F. Eastman. *Appl. Phys. Lett.*, 79(10):1489–1491, 2001.

[61] Hai Lu, William J. Schaff, Lester F. Eastman, and C. E. Stutz. *Appl. Phys. Lett.*, 82 (11):1736–1738, 2003.

[62] S. Makram-Ebeid. *Appl. Phys. Lett.*, 37(5):464–466, 1980.

[63] V.V. Mamutin, V.A. Vekshin, V.Yu. Davydov, V.V. Ratnikov, Yu.A. Kudriavtsev, B.Ya. Ber, V.V. Emtsev, and S.V. Ivanov. *Phys. Status Solidi A*, 176(1):373–378, 1999.

[64] V.V. Mamutin, V.A. Vekshin, V.Yu. Davydov, V.V. Ratnikov, T.V. Shubina, S.V. Ivanov, P.S. Kopev, M. Karlsteen, U. Söderwall, and M. Willander. *Phys. Status Solidi A*, 176(1):247–252, 1999.

[65] Takashi Matsuoka. *Appl. Phys. Lett.*, 71(1):105–106, 1997.

[66] Takashi Matsuoka, Hiroshi Okamoto, Masashi Nakao, Hiroshi Harima, and Eiji Kurimoto. *Appl. Phys. Lett.*, 81(7):1246–1248, 2002.

[67] T. Mattila and R. M. Nieminen. *Phys. Rev. B*, 55:9571–9576, April 1997.

[68] M. D. McCluskey, N. M. Johnson, C. G. van de Walle, D. P. Bour, M. Kneissl, and W. Walukiewicz. *Phys. Rev. Lett.*, 80:4008–4011, May 1998.

[69] T. Metzger, R. Hopler, E. Born, O. Ambacher, M. Stutzmann, R. Stommer, M. Schuster, H. Gobel, S. Christiansen, M. Albrecht, and H.P. Strunk. *Philos. Mag. A*, 77(4):1013, 1998.

[70] E. J. Miller, D. M. Schaadt, E. T. Yu, C. Poblenz, C. Elsass, and J. S. Speck. *J. Appl. Phys.*, 91(12):9821–9826, 2002.

[71] C. R. Miskys, J. A. Garrido, C. E. Nebel, M. Hermann, O. Ambacher, M. Eickhoff, and M. Stutzmann. *Appl. Phys. Lett.*, 82:290, 2003.

[72] H. Morkoç. *Nitride semiconductors and devices*. Springer-Verlag, Berlin-Heidelberg, 1999.

[73] N. Holonyak, Jr. and S. F. Bevacqua. *Appl. Phys. Lett.*, 1(4):82–83, 1962.

[74] N. Nakada, M. Nakaji, H. Ishikawa, T. Egawa, M. Umeno, and T. Jimbo. *Appl. Phys. Lett.*, 76:1804, 2000.

[75] S. Nakamura and G. Fasol. *The blue laser diode*. Springer-Verlag, Berlin Heidelberg New York, 1997.

[76] M. L. Nakarmi, K. H. Kim, K. Zhu, J. Y. Lin, and H. X. Jiang. *Appl. Phys. Lett.*, 85 (17):3769–3771, 2004.

[77] K. B. Nam, J. Li, M. L. Nakarmi, J. Y. Lin, and H. X. Jiang. *Appl. Phys. Lett.*, 81: 1083, 2002.

[78] K. B. Nam, M. L. Nakarmi, J. Li, J. Y. Lin, and H. X. Jiang. *Appl. Phys. Lett.*, 83: 2787, 2003.

[79] F. B. Naranjo, S. Fernández, M. A. Sánchez-García, F. Calle, and E. Calleja. *Appl. Phys. Lett.*, 80:2198, 2002.

[80] F. Natali, D. Byrne, A. Dussaigne, N. Grandjean, J. Massies, and B. Damilano. *Appl. Phys. Lett.*, 82:499, 2003.

[81] H. M. Ng and T. D. Moustakas. *MRS Internet J. Nitride Semicond. Res.*, 5S1:W1.8, 2000.

[82] H. M. Ng, D. Doppalapudi, E. Iliopoulos, and T. D. Moustakas. *Appl. Phys. Lett.*, 74:1036, 1999.

[83] H. M. Ng, T. D. Moustakas, and S. N. G. Chu. *Appl. Phys. Lett.*, 76:2818, 2000.

[84] H. X. Nguyen and W. Egorow. *Nonlinear optical effects in CdS and GaSe crystals*. Habilitation, Zentralinstitut für Elektronenphysik, Berlin, 1988.

[85] W. D. Nix and B. M. Clemens. *J. Mater. Res*, 14(8):3467–3473, 1999.

[86] J. I. Pankove, E. A. Miller, and J. E. Berkeyheiser. *J. Luminescence*, 5:84, 1972.

[87] Si-Hyun Park, Jaehoon Kim, Heonsu Jeona, Tan Sakong, Sung-Nam Lee, Suhee Chae, Y. Park, Chang-Hyun Jeong, Geun-Young Yeom, and Yong-Hoon Cho. *Appl. Phys. Lett.*, 83:2121, 2003.

[88] M. Pophristic, S. P. Guo, and B. Peres. *Appl. Phys. Lett.*, 82:4289, 2003.

[89] Jelena Ristić, Enrique Calleja, Achim Trampert, Sergio Fernandez-Garrido, Carlos Rivera, Uwe Jahn, and Klaus H. Ploog. *Phys. Rev. Lett.*, 94(14):146102, 2005.

[90] H. P. D. Schenk, E. Feltin, P. Vennéguès, O. Tottereau, M. Laügt, M. Vaille, B. Beaumont, P. de Mierry, P. Gibart, S. Fernández, and F. Calle. *Phys. Status Solidi A*, 188:899, 2001.

[91] S. Shokhovets, R. Goldhahn, G. Gobsch, S. Piekh, R. Lantier, A. Rizzi, V. Lebedev, and W. Richter. *J. Appl. Phys.*, 94:307, 2003.

[92] S. Shokhovets, G. Gobsch, and O. Ambacher. *Appl. Phys. Lett.*, 86(16):161908, 2005.

[93] B. S. Simpkins, E. T. Yua, P. Waltereit, and J. S. Speck. *J. Appl. Phys.*, 94:1448, 2003.

[94] G. Snider. 1D Poisson, `http:www.nd.edu\~snider`. Department of Electrical Engineering, University of Notre Dame, Notre Dame, IN 46556, `e-mail: snider.7@nd.edu`.

[95] T. Someya and Y. Arakawa. *Appl. Phys. Lett.*, 73:3653, 1998.

[96] Takao Someya, Yasuhiko Arakawa, Ralph Werner, Alfred Forchel, Massimo Catalano, and Roberto Cingolani. *Science*, 285:1905, 1999.

[97] Y.-K. Song, M. Diagne, H. Zhou, A. V. Nurmikko, R. P. Schneider Jr., and T. Takeuchi. *Appl. Phys. Lett.*, 77:1744, 2000.

[98] Y.-K. Song, H. Zhou, M. Diagne, A. V. Nurmikko, R. P. Schneider, Jr., C. P. Kuo, M. R. Krames, R. S. Kern, C. Carter-Coman, and F. A. Kish. *Appl. Phys. Lett.*, 76: 1662, 2000.

[99] J. Spradlin, S. Doğan, J. Xie, R. Molnar, A. A. Baski, and H. Morkoç. *Appl. Phys. Lett.*, 84:4150, 2004.

[100] C. Stampfl and C. G. Van de Walle. *Phys. Rev. B*, 65(15):155212, 2002.

[101] C. Stampfl and Chris G. Van de Walle. *Appl. Phys. Lett.*, 72:459, 1998.

[102] Yue Jun Sun, Oliver Brandt, Tian Yu Liu, Achim Trampert, Klaus H. Ploog, Jürgen Bläsing, and Alois Krost. *Appl. Phys. Lett.*, 81(26):4928–4930, 2002.

[103] S. Syed, J. B. Heroux, Y. J. Wang, M. J. Manfra, R. J. Molnar, and H. L. Stormer. *Appl. Phys. Lett.*, 83(22):4553–4555, 2003.

[104] Yoshitaka Taniyasu, Makoto Kasu, and Naoki Kobayashi. *Appl. Phys. Lett.*, 81: 1255, 2002.

[105] Yoshitaka Taniyasu, Makoto Kasu, and Toshiki Makimoto. *Appl. Phys. Lett.*, 84: 2115, 2004.

[106] Yoshitaka Taniyasu, Makoto Kasu, and Toshiki Makimoto. *Appl. Phys. Lett.*, 85: 4672, 2004.

[107] T. L. Tansley and C. P. Foley. *J. Appl. Phys.*, 59(9):3241–3244, 1986.

[108] T. Tawara, H. Gotoh, T. Akasaka, N. Kobayashi, and T. Saitoh. *Phys. Rev. Lett.*, 92 (25):256402, 2004.

[109] Takehiko Tawara, Hideki Gotoh, Tetsuya Akasaka, Naoki Kobayashi, and Tadashi Saitoh. *Appl. Phys. Lett.*, 83:830, 2003.

[110] A. Thamm, O. Brandt, K. H. Ploog, J. Hilsenbeck, and R. Lossy. In *27th International Symposium on Compound Semiconductors edited by M. Melloch and M. A. Reed*, page 455. IEEE Piscataway, 2000.

[111] I. Vurgaftman and J. R. Meyer. *J. Appl. Phys.*, 94(6):3675–3696, 2003.

[112] M. C. Wagener, G. R. James, and F. Omnès. *Appl. Phys. Lett.*, 83:4193, 2003.

[113] K. E. Waldrip, J. Han, J. J. Figiel, H. Zhou, E. Makarona, and A. V. Nurmikko. *Appl. Phys. Lett.*, 78:3205, 2001.

[114] P. Waltereit. *(Al,Ga,In)N heterostructures grown along polar and non-polar directions by plasma-assisted molecular beam epitaxy*. Ph.D. thesis, Humboldt University Berlin, Berlin, 2001.

[115] P. Waltereit, O. Brandt, A. Trampert, M. Ramsteiner, M. Reiche, M. Qi, and K. H. Ploog. *Appl. Phys. Lett.*, 74(24):3660–3662, 1999.

[116] T. Wang, R. J. Lynch, P. J. Parbrook, R. Butté, A. Alyamani, D. Sanvitto, D. M. Whittaker, and M. S. Skolnick. *Appl. Phys. Lett.*, 85:43, 2004.

[117] M. J. Weber. *Handbook of optical materials*. CRC Press, Boca Raton, 2003.

[118] C. Weisbuch, M. Nishioka, A. Ishikawa, and Y. Arakawa. *Phys. Rev. Lett.*, 69(23): 3314–3317, 1992.

[119] J. Wu, W. Walukiewicz, W. Shan, K. M. Yu, J. W. Ager, E. E. Haller, H. Lu, and W. J. Schaff. *Phys. Rev. B*, 66(20):201403, November 2002.

[120] J. Wu, W. Walukiewicz, K. M. Yu, J. W. Ager III, E. E. Haller, Hai Lu, and William J. Schaff. *Appl. Phys. Lett.*, 80(25):4741–4743, 2002.

[121] J. Wu, W. Walukiewicz, K. M. Yu, J. W. Ager III, E. E. Haller, Hai Lu, William J. Schaff, Yoshiki Saito, and Yasushi Nanishi. *Appl. Phys. Lett.*, 80(21):3967–3969, 2002.

[122] K. Xu and A. Yoshikawa. *Appl. Phys. Lett.*, 83(2):251–253, 2003.

[123] Tokio Yamabe, Akitomo Tachibana, and Harris J. Silverstone. *Phys. Rev. A*, 16(3): 877–890, 1977.

[124] A. Yariv and P. Yeh. *Optical waves in crystals*. Wiley, Hoboken, 2003.

[125] P. Yeh. *Optical waves in layered media*. Wiley, New York, 1988.

[126] P. Y. Yu and M. Cardona. *Fundamentals of semiconductors*. Springer-Verlag, Berlin-Heidelberg, 2001.

[127] R. Zeisel, M. W. Bayerl, S. T. B. Goennenwein, R. Dimitrov, O. Ambacher, M. S. Brandt, and M. Stutzmann. *Phys. Rev. B*, 61(24):R16283–R16286, 2000.

[128] S. B. Zhang, S.-H. Wei, and Alex Zunger. *Phys. Rev. Lett.*, 84:1232, 2000.

[129] K. Zhu, M. L. Nakarmi, K. H. Kim, J. Y. Lin, and H. X. Jiang. *Appl. Phys. Lett.*, 85: 4669, 2004.

Acknowledgements

It is with great pleasure that I dedicate these final pages to express my deepest gratitude to all who have given me support, encouragement and inspiration during the course of my PhD work at PDI. I would especially like to thank the following persons. . .

. . . Prof. Dr. Klaus H. Ploog for giving me the opportunity to do my PhD thesis on MBE growth at PDI. MBE growth has fascinated me ever since my university years. I appreciate his great interest in my work, for his insightful advice and for providing the financial means to attend two important international conferences.

. . . Prof. Dr. W. Ted Masselink and Prof. Dr. Enrique Calleja for taking their time to review this work.

. . . Dr. Lutz Däweritz for his support and encouragement and for his good company in Seoul at the ISCS 2004.

. . . Dr. Oliver Brandt! If there was a Prize for PhD supervisors then Dr. Brandt certainly would have received several long ago. Words are not enough to describe his infinite patience, his engagement and encouragement and his profound knowledge in physics. From Dr. Brandt I have learned enormously much about material science, semiconductor physics, computers and the art of writing good scientific papers. Working with Dr. Brandt has been a true pleasure which I will miss.

. . . Hans-Peter Schönherr for his truly invaluable technical help with the MBE system. His expertise in the technical aspects of MBE kept M8 up and running almost continuously. This allowed me to perform the necessary growth experiments on which this thesis is based.

. . . Dr. Manfred Ramsteiner for his assistance on the μ-PL system and Raman measurements.

. . . Dr. Uwe Jahn for his help with SEM and CL measurements.

. . . Dr. Helmar Kostial for his great help with device processing.

… Dr. Achim Trampert for the TEM analysis of the AlN/GaN Bragg reflectors.

… Dr. Xiang Kong for his help with TEM on the (Al,In)N samples.

… Dr. Daniel Schaadt for teaching me the secrets of AFM.

… Dr. Torsten Hesjedal for helping out with the AFM and for his good suggestions.

… Dr. Lutz Schrottke for his great help with the PL setup and for his patience.

… Dr. Manfred Giehler for the help with the InN absorption measurements.

… Dr. Gregor Mussler for helping out with the IR-PL setup.

… Dr. Goldhahn at Technische Universität Ilmenau for his ellipsometry measurements.

… Ilka Schuster for her help with all kinds of image processing.

… Dr. Subhabrata Dhar for the discussions on physics and Indian culture.

… Dr. Atsushi Kawaharazuka and Dr. Jean-Michel Chauveau for the very good time shared. And of course I am thankful for their good cooking abilities.

… Dr. Dennis Kolovos-Vellianitis and Dr. Fumitaro Ishikawa for their excellent company and for the endless discussions about everything between heaven and earth.

… Pranob Misra for the good time shared and for the very fruitful discussions on nitrides and Indian mythology.

… Dr. Yue-Jun Sun for his help with the XRD equipment and for his interesting attitude.

… Claudia Hermann, Michael Höricke and Doris Spaniol for their technical assistance.

… Rebecca for her good and kind spirit.

… my father Tomo and my mother Irma for their never ending support and my brother Anders for his different perspective.

… and last but absolutely not the least, my wife Julia. Nothing would have been possible without her support and personal sacrifices and foremost her patience with all my crazy ideas.

Curriculum Vitae

Name:	Tommy Ive
Geburtstag:	11. März 1968
Geburtsort:	Växjö (Schweden)

06.2002 – 09.2005	Anfertigung der vorliegenden Dissertation am Paul-Drude-Institut für Festkörperelektronik in der Arbeitsgruppe von Herrn Dr. O. Brandt unter Betreuung von Herrn Prof. Dr. K. H. Ploog
11.1996 – 05.2002	Satellite Engineer Socité Européenne des Satellites (SES) - ASTRA (Luxembourg)
09.1996 – 11.1996	Software Engineer 3C Communications S.A. (Luxembourg)
1996	Master of Science in Engineering Physics Thema: *Diffusion and LPE Experiments Concerning Erbium Incorporation in Silicon* Betreuung: Herrn Prof. Dr. H. Grimmeiss
1989 – 1996	Studium der Technischen Physik Lund Institute of Technology Lund University (Schweden)
1988 – 1989	Wehrdienst Königlich Schwedische Flotte
1984 – 1987	Gymnasium in Växjö (Schweden)
1979 – 1984	Grundschule in Växjö (Schweden)

Selbständigkeitserklärung

Hiermit erkläre ich, die vorliegende Arbeit *Growth and investigation of AlN/GaN and (Al,In)N based Bragg reflectors* selbständig und nur unter Verwendung der gemäß §6 Absatz (3) angegebenen Hilfen und Hilfsmittel angefertigt zu haben.

Ich habe mich an keiner anderen Universität um einen Doktorgrad beworben und besitze auch keinen entsprechenden Doktorgrad.

Ich erkläre die Kenntnis der dem Verfahren zugrunde liegenden Promotionsordnung der Mathematisch-Naturwissenschaftlischen Fakultät I der Humboldt-Universität zu Berlin.